INCIPIENT TRANSPORT OF SILT-SIZED SEDIMENTS

by

Bruce James Nairn

Project Supervisors:

Norman H. Brooks
James J. Morgan
Fredric Raichlen

Supported by:

Andrew W. Mellon Foundation

Walter L. and Reta Mae Moore Fellowship

W. M. Keck Laboratory of Hydraulics and Water Resources
Division of Engineering and Applied Science
California Institute of Technology
Pasadena, California 91125

Report No. KH-R-59

May 1998

This report is same as the thesis of the same title submitted by the writer on May 19, 1998, to the California Institute of Technology, in partial fulfillment of the requirements for the degree of Doctor of Philosophy in Environmental Engineering Science.

Acknowledgements

Firstly, I'd like thank my advisor, Norman Brooks, for initially suggesting this project and providing great enthusiasm, guidance and support throughout my stay. You've taught me so much, allowed me the freedom to pursue my own ideas, and pointed out when I was off track. Thanks to Jim Morgan for teaching me about aquatic chemistry and providing insightful discussions and advice. I'd also like to thank the rest of my committee, Fred Raichlen, Chris Brennen, and Brad Werner for all the useful comments they provided. I am very grateful for the support the Andrew W. Mellon Foundation gave for this research and for the receipt of the Walter L. and Reta Mae Moore Fellowship during my final year.

Thanks also to Marcelo Garcia for his helpful comments and thought-provoking discussions during his stay here as a visiting professor.

This research would have been impossible without the able technical assistance of the sub-basement staff. Thanks to Hai Vu for help with the electronics, Rich Eastvedt for fixing all the little things, and to Russ Green and Joe Fontana for machining my test sections. Upstairs, Fran Matzen and Linda Scott provided much appreciated assistance with the administrative details. Thanks also to the librarians Rayma Harrison and Susan Leising.

Thanks to all my fellow graduate students for helping make my stay at Caltech so enjoyable. Particular thanks to Aaron, Phil, and Selena for their insightful advice and willingness to listen to my problems. Thanks to Selena and Rich for proof-reading and providing some of the photos. Thanks to Chuk, Claudine, Jenny, Rob, and all the others who let me ramble at CETF meetings. Jennifer, Oliver, Veronica, Tom, Linda, Paul, Pin, Susan and Fabrizio are a few of many who made my life so much more fun. Special thanks to Natalie for being so loving and understanding, and for providing some much needed distractions.

Finally, I would like to thank my parents, who have always been encouraging and supportive of my aspirations. In so many ways you managed to make everything so much easier for me. I dedicate this thesis to you.

Abstract

Laboratory experiments were conducted to determine the influence of stream bed shear stress and water chemistry on the sediment transport rate for silt-sized particles near the critical threshold for motion. Experiments were conducted in two large recirculating laboratory flumes, 40 m and 12 m long, with a small sediment bed 40 cm long. The sediment transport rate was determined from the volume of sediment eroded from this sediment bed per unit time. The smaller flume was filled with deionized water, to which specific electrolytes were added to vary the water chemistry.

Dimensional analysis predicted the sediment transport rate of non-cohesive material can be described by two dimensionless groups, one for transport and one for bed shear stress. A new transport model was developed on physical considerations for particles smaller than the thickness of the viscous sublayer, and supported this conclusion.

Sediment transport rates were measured in experiments using carefully cleaned glass beads (15 μm to 69 μm) in low ionic strength (10^{-4}M) solution by measuring the elevation of the sediment bed along transects with a laser displacement meter every 10 to 30 minutes. The results supported the prediction that the dimensionless transport rate is solely a function of the dimensionless shear stress (Shields parameter) and the water composition, and not of the bed Reynolds number, when the latter is less than one.

Experiments were conducted with NaCl and $CaCl_2$ electrolytes at differing concentrations up to 10^{-2} M, which reduced the transport rate by up to 2 to 3 orders of

magnitude for the finest particles. Calcium was more effective at reducing the sediment transport rate than sodium. These trends were captured by the transport model, but additional work is required in estimating the inter-particle forces.

A new criterion for initiation of motion is proposed based on a small dimensionless transport rate $q_s^* = 0.01$, corresponding to about 2% of the surface grains in motion. For bed Reynolds numbers $u^*d/\nu < 1$, the equivalent Shields parameter for critical shear becomes $\tau^* = 0.075$ for non-cohesive sediment. With cohesion, a new model is used to predict the change in the Shields curve for various dimensionless interparticle forces.

Table of Contents

List of Figures

List of Tables

Notation

a	-	particle radius
a, b	-	coefficients in general sediment transport equation
A_{eff}	-	Hamaker's constant, adjusted for retardation
B	-	flume width
b	-	width of sediment bed
d	-	particle diameter
D	-	water depth in flume
d_g	-	geometric mean particle diameter
$\dot{E}$	-	mean sediment bed elevation
Fc	-	cohesive force
Fc*	-	cohesive force normalized by particle's weight
F_D	-	drag force
F_L	-	lift force
g	-	gravitational acceleration
g_s	-	sediment transport rate, as mass per unit time per unit width
H	-	average bedform height
h	-	particle-particle separation distance
h	-	distance between point of action of fluid drag force and particle's center
h*	-	normalized displacement of the fluid drag from the particle centroid = h/a
I	-	ionic strength
L	-	length of sediment bed
n	-	fractional area of the sediment bed in motion

p - pressure

Q - total flow rate

q_B - bedload transport rate, volume per unit width

q^* - normalized sediment transport rate, $q_s/(gRd^3)^{1/2}$

q_B^* - normalized sediment transport rate, qs/u*d

q_s - bulk volumetric sediment transport, per unit width

Q_s - bulk volumetric sediment transport

q_s^* - dimensionless sediment transport parameter, $\frac{q_s \mu}{\tau d^2}$

R - density ratio minus one, $\frac{\rho_s - \rho}{\rho}$

Re - Flow Reynolds number $\frac{UD}{\nu}$

Re* - Bed Reynolds number $\frac{u^* d}{\nu}$

t - time

U - average flow velocity in flume channel

u - streamwise velocity

u* - friction velocity

v - vertical velocity

V - volume of water in the flume

w_s - settling velocity

x - streamwise coordinate

y - vertical coordinate

z - ionic charge

z - horizontal, cross stream coordinate

Φ - surface interaction potential $\Phi = \int_{\infty}^{0} F dx$

Ψ_d - diffuse layer potential

Ψ_o - surface potential

δ - normalized particle protrusion from the mean bed elevation

δ_{max} - protrusion of the least stable particle on a sediment bed

ϕ - contact angle of downstream grain

η - sediment bed elevation

$\overline{\eta}$ - mean sediment bed elevation

κ - Von Karman constant, 0.4

κ - double layer thickness

λ - average bedform wavelength

μ - viscosity

ν - kinematic viscosity

θ - porosity of the sediment bed

ρ - density, water

ρ_b - bulk density of the sediment bed

ρ_s - particle density

ρ_s - sediment density

σ_g - geometric standard deviation of the sand grain diameters

τ - fluid shear stress on sediment bed

τ^* - dimensionless shear stress, Shields parameter, $\frac{\tau}{(\rho_s - \rho)gd}$

τ_c^* - critical dimesionless shear stress

1 Introduction

1.1 Overview

Sediments composed of silt-sized particles are found throughout the world, in both fresh and saline environments. The erosion of sediment can have a significant impact on the benthic community, the marine geological record, and on pollutant transport. With a high specific surface area, fine sediments create an effective sink for many pollutants and hydrophobic compounds. Erosion of contaminated sediment reintroduces these pollutants into the water column, where they may be transported over large distances. Thus, the conditions required to mobilize the bottom sediments are very important in predicting the fate of such pollutants. In this work, the factors that affect the mobility of such silt-sized particles are addressed and the sediment transport rate of 15-70 μm-sized particles are reported.

A typical natural setting has uni-directional flow of water over a sediment bed; friction along the boundary results in a shear stress acting on the sediment. As a result, each sediment particle experiences a drag force, which if sufficiently large, will dislodge the particle from the bed. If the particles continue to roll downstream along the sediment bed, the transport is referred to as bedload. Suspended load refers to the particles that are carried primarily in suspension along with the stream flow.

The flow conditions at which sediment particles begin to move is the critical, or threshold, condition. The corresponding fluid shear stress is the critical shear stress (τ_c). For non-cohesive sediments, the fluid force on a particle must overcome the submerged weight acting to keep it stationary. The required shear stress has been determined

experimentally as a relation between shear stress, grain size, viscosity and the submerged weight. Cohesive sediments possess additional attractive chemical forces between the individual sediment particles, which act to increase the stability of the bed and the critical shear stress.

Previous experimental research to determine the threshold of motion has concentrated on non-cohesive sand and gravel sized particles ($d > \sim 0.1$ mm). These experiments are conceptually simple. The sediment bed is watched as the fluid shear is gradually increased. When the sediment grains begin to move, the threshold condition has been passed. These experiments are typically conducted in a laboratory flume, in which the channel bottom is fully covered with sediment of a known size. Only a few experiments of this nature have been reported for silt-sized particles, due in part to the difficulty in observing them. The difficulty in observing particle motion has led previous researchers to use smaller flumes and more viscous fluids with larger particles to obtain similarity conditions to silt-sized sediments. The resulting low Reynolds numbers precluded turbulent effects that might play a role in mobilizing sediments in environmental flows.

The majority of fine sediments found in the natural environment contain a broad mixture of particle sizes and mineral compositions. As sediments transition from sand-size to clay-size, they typically become more cohesive. In the majority of previous flume studies, the fine sediment particles were considered analogous to sand sized particles; cohesion has been ignored as an explanation of the increased threshold condition observed for smaller sized particles.

The state of knowledge for cohesive sediments is much less developed than that for non-cohesive materials. The cohesive forces acting to stabilize the sediment bed are difficult to predict, and most previous work has employed bulk material parameters to correlate with the results. Cohesive sediments encompass a large range of material properties, from consolidated soils to very loose, flocculated mud suspensions. Good correlations have been obtained between rheological parameters (i.e., yield stress, viscosity) of loosely consolidated muds and their erosion threshold. Within a fine sediment system, the presence of multivalent ions, fine particle sizes, or organic binding agents is known to increase the cohesive behavior. This cohesion creates a larger resistance to erosion than expected on the basis of particle weight alone.

1.2 The Present Study

The goal of this study was to measure the transport rate of fine sediments near the critical threshold of motion and to examine how this rate was influenced by turbulence and chemical parameters. Experiments were designed to measure the rate of particle erosion to avoid bias from subjective interpretations of the amount of motion corresponding to the threshold condition. By eliminating the need to be close to the sediment for visual observations, a large (60 cm deep) laboratory flume could be used to allow fully turbulent flow at high Reynolds numbers. This allowed investigation into the possibility of large turbulent eddies causing sediment resuspension.

The experiments were designed to use a small volume of sediment contained in a test tray mounted flush with the flume bottom. The reduced amount of material made it practical to wash the particles to remove organics and metals that might promote cohesion. Glass beads were chosen as model sediment because they are similar to natural

silica particles, and are predominately spherical, ensuring that the particle geometries would be identical for all particle sizes. The beads were sorted by sedimentation into four sizes, 15 μm, 26.5 μm, 41 μm and 69 μm, all with a narrow log-normal distribution ($\sigma_g \sim 1.3$).

A highly accurate (+/- 10 μm), non-intrusive, laser displacement meter was used to measure the elevation of the sediment bed. The sediment transport rate was quantified by computing the rate at which material was removed from the test bed from repeated measurements of the bed elevation. A quantitative measure of the sediment transport also allowed the influence of chemical variables on the transport rate to be studied. Field evidence and previous studies have shown that the critical shear stress increases for decreasing particle size, but without consideration of chemical parameters that might reduce the mobility of fine sediment.

Chapter 2 contains a brief review of previous work that addressed the mobility of silt-sized particles or sediments. A review of available information on chemical treatments designed to clean particle surfaces is also included.

Chapter 3 develops a series of simple models aimed at predicting the mechanisms of sediment motion and the influence of chemical parameters.

The apparatus designed to measure the sediment transport rate, and the 12-meter and 40-meter recirculating flumes are described in Chapter 4. The experimental procedure is also discussed.

The experimental results are presented and briefly discussed in Chapter 5. Chapter 6 contains detailed discussion of the results and compares the results to the models presented in Chapter 3.

A summary of the work and the conclusions are given in Chapter 7.

Appendix A discusses the chemical processes considered in modeling the cohesive nature of the glass beads.

1.3 Definition of Terms

For clarity, definitions are given for some of the terms used in this work. These terms may have different implications in other scientific fields.

Barchan: a crescent shaped ripple or dune.

Bed profile: the sequence of measurements of the sediment bed's elevation traversing the length of the sediment bed.

Bed Reynolds number: the Reynolds number based on the friction velocity and sediment grain size, $Re^* = u^*d/\nu$.

Bed sediment, bed material: the particles that make up the bed. Soda-lime glass beads were used in all experiments except Series E (two experiments).

Bedform: Periodic variation in the elevation of the sediment bed caused by the interaction between fluid flow and sediment transport. Different shapes of bedforms occur under different flow conditions. See also ripple, barchan.

Bedload, bed-load transport rate: sediment particles that are carried along with the fluid flow within a layer one to two particle diameters in extent above the sediment bed.

Cohesion, inter-particle forces: non-gravitational forces that act to keep particles agglomerated.

Critical condition, threshold condition: the flow parameters that cause surfical sediments to be moved, such as velocity or shear stress.

Critical shear stress: the fluid shear stress acting on the sediment bed which causes a predefined fraction of particles to move.

Critical velocity: the mean flow velocity that corresponds to sediment particles just beginning to move.

Erosion, erosion rate: the process (or rate thereof) of removing material from the sediment bed. It implies a flux of particles normal to the sediment bed.

Ionic strength: the charge weighted concentration of all ions in solution.

Mean bed elevation: the spatial average of the surface of the sediment bed.

Mean velocity: fluid velocity averaged over the flow cross section (A), = Q/A.

Resuspension: the process of entraining sediment particles into the mean fluid flow from the sediment bed.

Ripple: a small bedform, primarily two-dimensional in nature, with a triangular shape, consisting of a gradual rise in elevation along the upstream surface, followed by a sharp crest and steep slope. A wavelength to amplitude ratio of about 10 is typical with sand beds. The ripples observed in this work were much flatter, the wavelength being about 50 times the amplitude.

Shear stress, bed shear stress: the fluid force acting on the sediment bed, $\tau = \rho u^{*2}$.

Shear velocity: u* - defined by $u^* = \sqrt{\frac{\tau}{\rho}}$.

Silt: sediment particles with a diameter between 4 and 64 μm.

Stream Reynolds Number: the Reynolds number based on the mean velocity and the hydraulic diameter of the flow.

Test tray: the stainless steel cavity that held the sediment.

Total sediment transport rate: the volume (or mass) flux of sediment, irrespective of its mode of transport (bedload or suspended load).

Transport rate: the rate at which material is carried through a given cross-section of the stream. It implies that the particles are moving parallel to the sediment bed, and is expressed as a bulk volume per unit width per unit time.

2 Background

2.1 Overview

The behaviour of silt-sized sediments has generally been estimated from the extrapolation of results for larger sized materials. Several studies have used silt-sized material to measure the critical shear stress that initiates motion of the sediment. The individual forces acting on a single particle have been modeled to give a theoretical prediction of the critical condition. For smaller particles, the forces arising from chemical interactions between individual particles can become comparable with the particle's weight, and must be accounted for in any modeling efforts.

2.2 Initiation of Motion

Shields (1936) modeled the forces on a single particle situated at a flat sediment/fluid interface, and found that the condition for particle motion could be expressed by two dimensionless variables. Since several of the coefficients could not be predicted, he conducted experiments to determine the relation $\tau_c^* = f(\mathrm{Re}^*)$ for initiation of motion, where

$$\tau_c^* = \frac{\tau_c}{(\rho_s - \rho)gd}$$ ratio of: shear force to particle weight

$$\mathrm{Re}^* = \frac{u^* d}{\upsilon}$$ ratio of: particle diameter to viscous sub-layer thickness, multiplied by 11.6, if the viscous sub-layer thickness is taken as 11.6 ν/u*.

τ_c – critical bed shear stress

ρ_s - sediment particle density

ρ - fluid density

g - gravity

d - median grain size

ν - kinematic viscosity

u* - friction velocity = $\sqrt{\frac{\tau}{\rho}}$

The experimental results of Shields' investigation is reproduced in Figure 2.1 (Shields, 1936). Rouse (1939) transformed Shields' fuzzy zone indicated here to a solid line. Shields' measurements extended down to Re* ~ 1, and from these measurements he extrapolated to smaller particle sizes. His proposed extrapolation was $\tau_c^* \sim 0.1(Re^*)^{-1}$.

It has been suggested that Shields' employed the transport relationship given in his thesis to extrapolate several experiments back to a condition of zero transport. However, Kennedy (1995) found no evidence of this when he reviewed the original work of Shields.

Critical shear stress has been a fundamental component in sediment transport literature. Reviews of the work have been published by: Vanoni, et al. (1966); Miller, et al. (1977); and Buffington and Montgomery (1997). The following focuses on work directly related to silt-sized material.

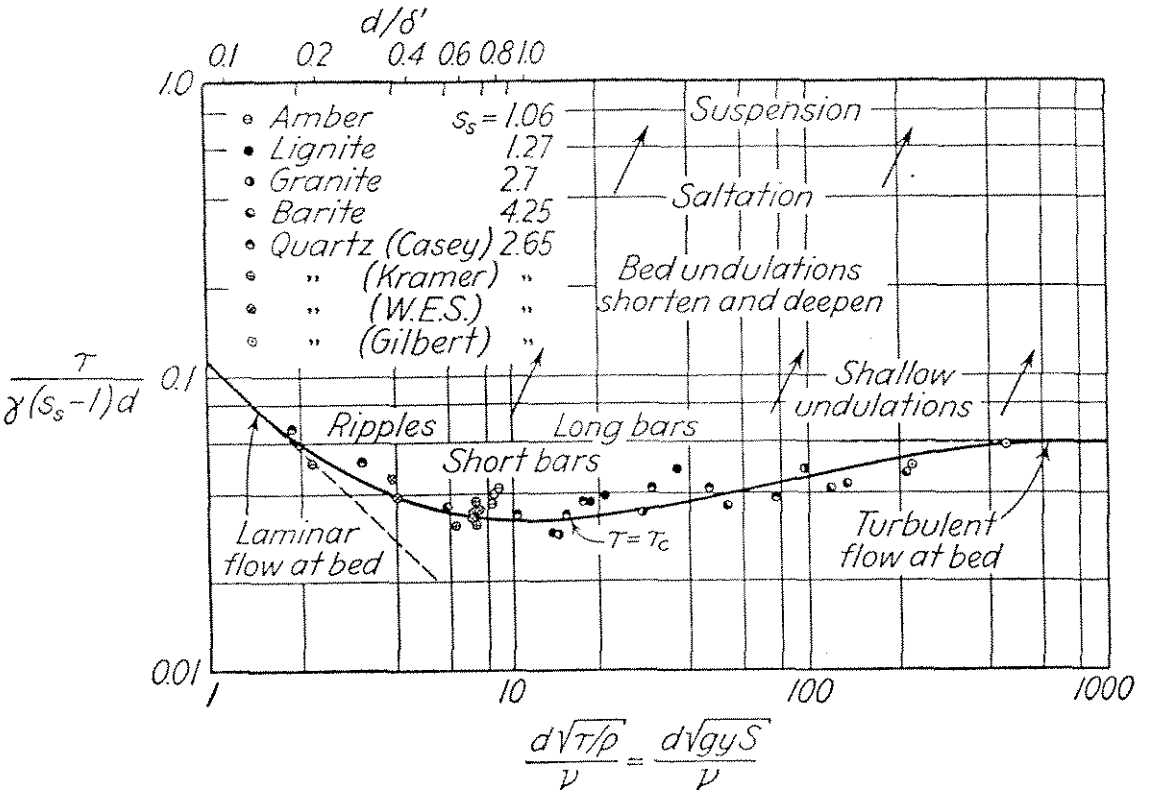

Figure 2.1: Shields curve as redrawn by Rouse (1950).

Theoretical evaluations of the critical shear stress have been derived by balancing forces on a hypothetical 'critical' particle (Figure 2.2). White (1940) and all following workers have found that this approach predicts that τ_c^* becomes independent of the bed Reynolds number (Re*) below unity. The inclusion of lift forces (Wiberg & Smith (1989), Ling (1995)) does not alter this conclusion. This is contrary to Shields' hypothesis and the experimental results that follow.

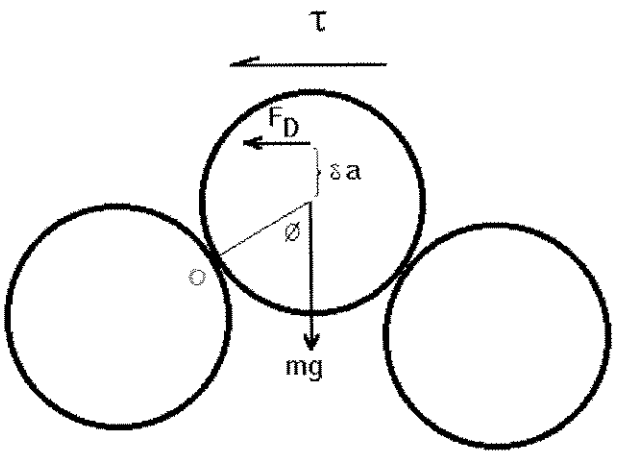

Figure 2.2: Hypothetical critical particle, and forces considered to act upon it.

The first experimental test of Shields' extrapolation to lower particle size (or bed Reynolds number, Re*) was performed by Vanoni (1964) using two particle sizes (d = 37, 102 μm) in the developing boundary layer of a recirculating flume. Experimentally, a small amount of sediment movement was observed visually, and the intensity of motion was determined from the frequency of observed bursts of sediment motion. These observations were classified as negligible, small, critical, or general bed motion, and are presented in Figure 2.3. These results illustrate that the value reported as the 'critical' shear stress will depend on what condition is considered "initiation of motion".

Vanoni also observed that the intensity of motion increased as the boundary layer developed, suggesting that turbulence plays an important role in erosion.

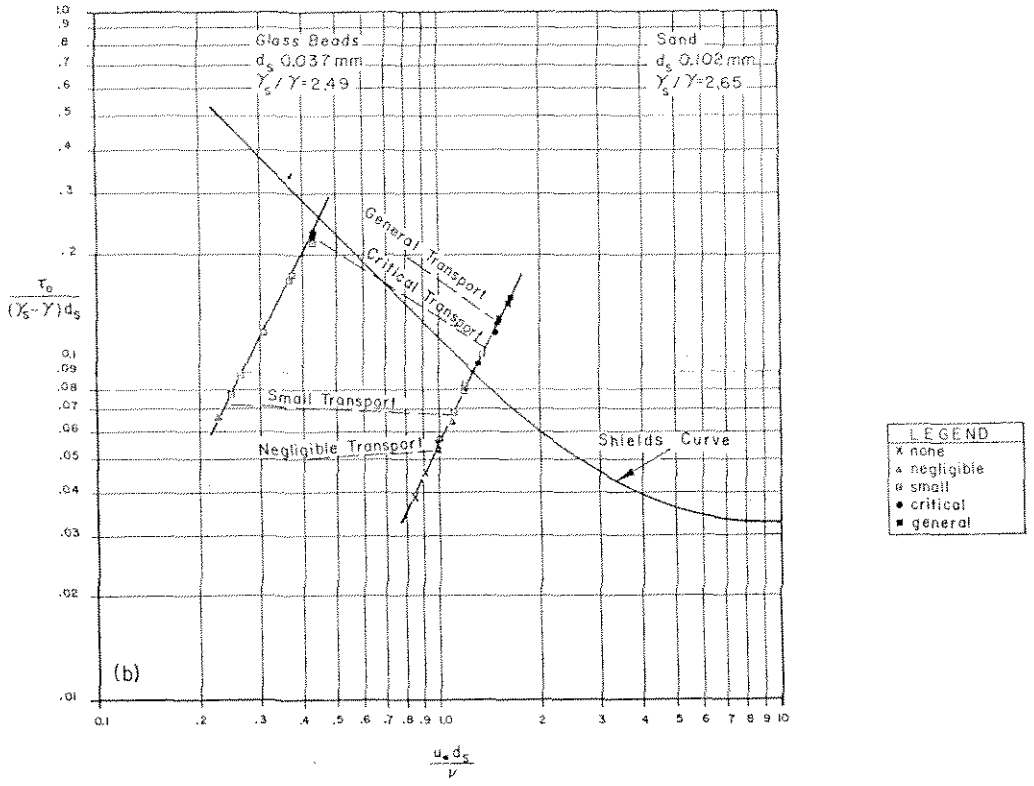

Figure 2.3: Results from Vanoni (1964) illustrating the dependence of the 'critical' shear stress on the definition of initiation of motion.

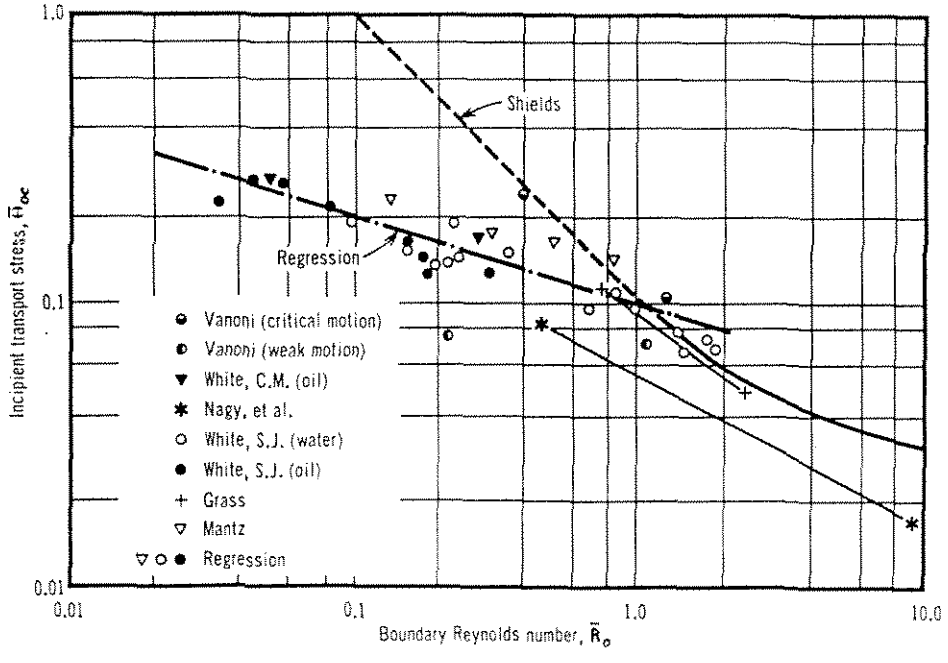

Figure 2.4: Experimental results to extend Shields' curve to smaller particle sizes. (Mantz, 1977)

Grass (1970) performed a set of experiments to examine the relationship between turbulence and erosion for fine sand (0.09 – 0.195 mm). A wire generated a line of hydrogen (H_2) bubbles in the flow, whose subsequent deformation was recorded with a high speed camera to determine the instantaneous shear. Individual grain motions were captured along with the H_2 bubble profile, allowing measurement of the shear stress corresponding to particle motion. The probability of the turbulent shear stress exceeding the stability of a grain was used to show that Shields' curve corresponded to a finite transport rate. The results of this investigation showed that τ_c^* scaled as $Re^{*-0.55}$, less than the 1/Re* dependence predicted by Shields (Figure 2.4).

White (1970) and Mantz (1977) conducted experiments with a variety of particles ($15 < d < 170$ μm) in oil and water flows. All of the oil-flow experiments were laminar, but those in water were turbulent ($1500 < Re < 20{,}000$). Mantz proposed that the correlation $\tau_c^* = 0.1(Re^*)^{-0.30}$ would fit both the laminar and turbulent results (Figure 2.4). Yalin and Karahan (1979) reported similar results from experiments under laminar flow conditions.

Unsold (1984) performed a comprehensive set of measurements of quartz grains (3 – 260 μm) in water. In these experiments the transport rate was measured by collecting the eroded material downstream of a 29.4 cm wide x 50 cm long test section. While the dimensionless transport rates from his experiments did not collapse into a single curve (Figure 2.5), he suggested a value of dimensionless transport rate ($q_s^+ \sim 10^{-4}$) to represent the critical condition, where $q_s^+ = g_s/\rho_s u^* d$. He established that this dimensionless transport rate was compatible with the generally accepted Shields' curve at

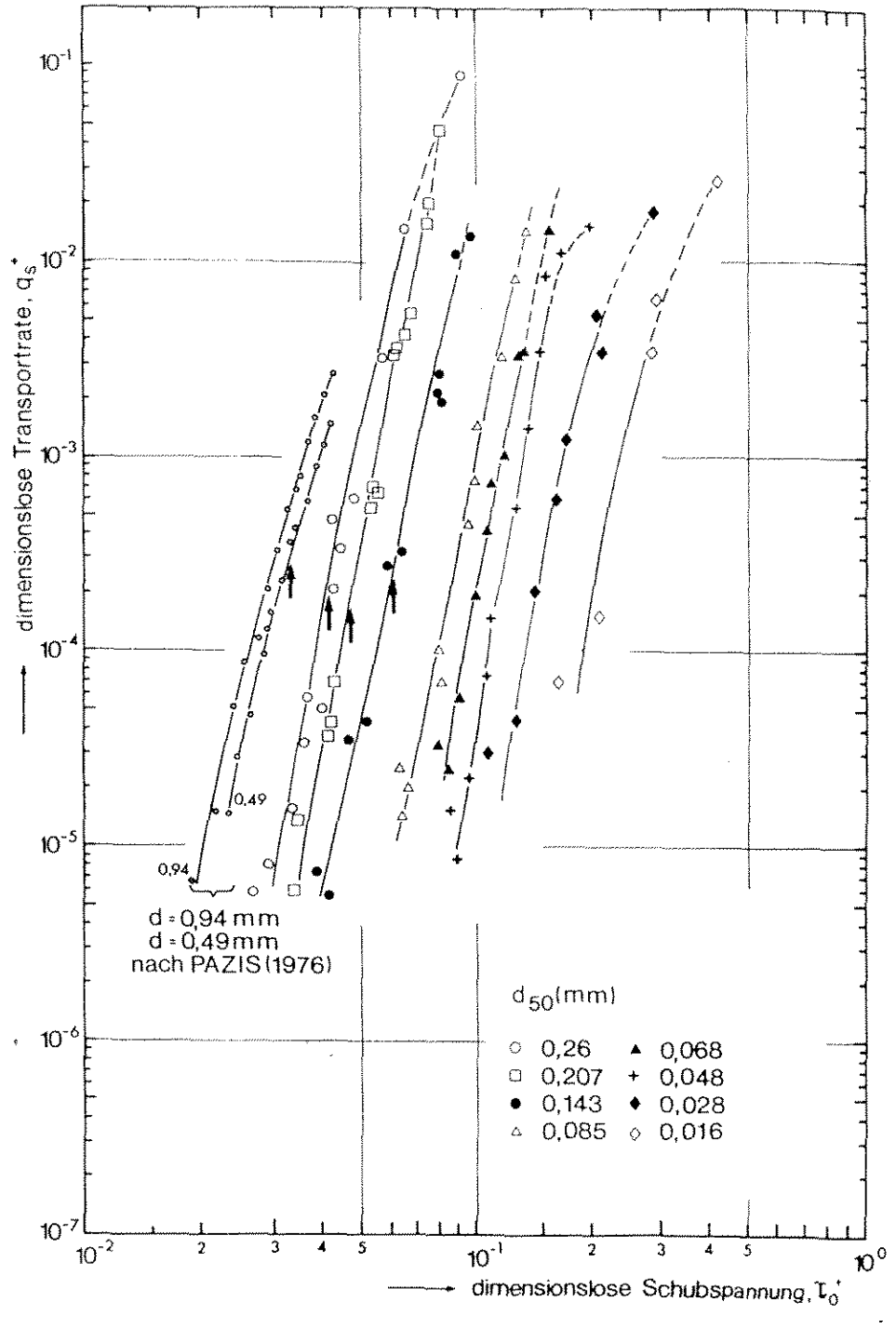

Figure 2.5: Dimensionless transport rates measured by Unsold (1984). The dimensionless parameter $q_s^+ = \frac{g_s}{\rho_s d u*}$ where g_s is the sediment mass transport rate (g cm^{-1} s^{-1}).

higher bed Reynolds numbers. This curve also fell somewhere in between Shields' 45° extrapolation and a constant value.

One additional investigation of interest is that of Rees (1966), who conducted flume experiments with a natural silt (10μm) containing a very small amount of clay. He observed the initiation of bed motion at $\tau^* = 0.10$ for $Re^* = 0.04$, significantly below that found by others.

2.3 Sediment Transport

The critical shear stress is an important conceptual parameter in most bedload sediment transport models, including those of Bagnold (1957), Wiberg and Smith (1989) and others. These models incorporate the critical shear stress in a manner similar to that of the more empirical equation of Meyer-Peter and Muller (1948):

$$q^* = 8(\tau^* - \tau_c^*)^{3/2}, \qquad \tau_c^* = 0.047 \tag{2.1}$$

or in general, $q^* = a(\tau^* - \tau_c^*)^b$

in which $q^* = q_B/((\rho_s/\rho - 1)gd^3)^{1/2}$; q_B is the bedload transport rate, as solid volume per time per unit width. Descriptions of these transport models can be found in Vanoni (1975), Raudkivi (1990) and others. Almost exclusively, these sediment transport models have been designed with larger sized particles in mind. Nonetheless, they provide a conceptual framework for evaluating the transport rate results obtained in these experiments.

Einstien (1942, 1950) introduced the notion that particle movement could be modeled as a stochastic process. He pointed out that in turbulent flow the fluid forces acting on the sediment bed vary with respect to both time and space. Therefore, the movement of any particle depends on the probability, p, that the applied force exceed the

resisting forces at that particular time and place. For low rates of transport, Einstein's formulation agrees well with equation (2.1). Other transport formula based on a similar probablistic approach have been proposed, and reviewed in texts of Raudkivi (1990), Vanoni (1975).

Lavelle and Mofjeld (1987) presented an argument against the use of a critical shear stress in predicting non-cohesive sediment transport. Instead, a stochastic view of sediment transport is advanced. They point out that the majority of sediment transport results (even at low dimensionless shear stresses) are still well fit by a simple power law equation of the form:

$$q \sim a(\tau^*)^b$$

implying that no critical stress exists and some transport occurs under all conditions.

Unsold (1984) found a power law relation of this type satisfactorily fit the sediment transport rates he observed (shown in Figure 2.5). Unfortunately, the constants a and b varied with particle size. Unsold reported that for sediment sizes below 10μm the measured transport rates varied erratically, and coincided with a large increase in the critical Shields parameter (τ_c^*). This was attributed to 'cohesion' in the water-quartz system. Measurements of the angle of repose supported the assumption that these sediments were cohesive, but no attempt was made to investigate the chemical nature of this cohesion. It is unclear if the erratic transport rates may also have been due to the fine particles avoiding the sediment trap used. Unsold's results are discussed in greater detail within the context of this work in Section 6.5.

2.4 Resuspension

Resuspension refers to the process of sediment particles becoming entrained into suspension in the mean fluid flow from the sediment bed. The ratio of the particle settling velocity, w_s, to friction velocity, u*, has been the traditional criterion for the occurrence of suspended load. For conditions in which $w_s/u^* < 1$, the turbulent velocity fluctuations are expected to be able to keep the sediment in suspension, producing suspended load in addition to bedload. However, recent work by Nino and Garcia (1995) has shown that silt-sized particles are not initially resuspended from a flat bed until significantly higher shear stresses are reached than implied by this criterion.

Leighton and Acrivos (1986) have observed that particles can become resuspended in laminar flow, a process they term viscous resuspension. Particles moving along the wall (bed) interact with themselves, creating a diffusion-like process moving the particles away from the wall. Their experimental results indicated that a dimensionless shear stress (τ^*) of 0.5 was required to begin resuspension.

2.5 Cohesive Materials

Cohesive sediments are rather arbitrarily classified as either soils or muds, depending upon their degree of consolidation. The term soil is used to identify firm consolidated deposits of cohesive material. Studies on the erosion characteristics of soils have presented the results in terms of bulk parameters used in soil mechanics. These have not yielded results that can be readily used for predictive purposes (Raudkivi, 1990) and empirical data are usually relied upon.

Muds refer to soft, loosely or unconsolidated deposits of cohesive material, and are commonly found in estuarine environments. They are commonly modeled as a dense suspension, and have properties very similar to a non-Newtonian fluid.

Otsubo & Muraoka (1988) attempted to relate the critical shear stress to the rheological properties of a variety of muds and clays. They found two critical conditions: that for floc erosion (similar to non-cohesive erosion) and that for massive bed failure. Both of these conditions correlated closely with the yield stress, for materials that possessed a finite yield stress. Their results were similar to that obtained by Migniot (1968), except Migniot's data changed its dependence on yield stress for larger yield stresses.

Dade (1992) modified a force balance model to incorporate cohesion on the basis of the yield stress (τ_y - i.e., considering the sediment to be a non-Newtonian fluid). An adhesive force proportional to the contact area of a particle and the yield stress was incorporated in a force balance model. This resulted in good agreement with both Migniot's and Otsubo & Muraoka's data. A similar model was also proposed by Junda and Zhiliang (1989), who incorporated a concentration dependence. Other investigators (Metha, 1994; Junda and Zhiliang, 1989) have found a large dependence on the degree of material consolidation or water content.

Studies on cohesive materials have focused on highly cohesive systems, and little work has been done on slightly cohesive sediments, or transitional conditions between "non-cohesive" and "cohesive" (Metha, 1994, Partheniades, 1992).

2.6 Particle – Particle Forces

A quantitative measure describing the cohesive properties of a sediment is desired to assist in understanding the factors affecting both the critical shear stress and the transport rate of a given sediment. The preceding models utilized the yield stress as a measure of the interparticle chemical forces in weakly consolidated muds. But rheological measurements are sensible only for fluid-like materials. Alternatively, it has been shown that interparticle forces can be accurately computed from particle surface chemistry and composition of the electrolyte solution.

A theory describing the interaction energies between colloidal particles was developed independently by Derjaguin and Landau (1941) and Verwey and Overbeek (1948). Now known as the DLVO theory, it uses the superposition of van der Waals and electrostatic forces to predict colloidal stability. Details on using this approach to compute interparticle forces can be found in texts such as Stumm and Morgan (1996), and Israelachvili (1991).

In general terms, the DLVO theory is used to compute the net force between two surfaces as the linear superposition of two forces: Van der Waals and electrostatic. Van der Waals (or London) forces arise between two objects as local fluctuations in polarization within one particle induce, via the propagation of electromagnetic waves, a correlated response in the other particle. As the distance between particles increases, the finite speed of propagation induces a phase shift, reducing the degree of correlation and the attractive force. While this force decays rapidly, the cumulative effect of summation over all molecules is a force that scales with the particle size (diameter). The Van der Waals force between two identical spheres (radius a) is given by:

$$F_a(h) = \frac{A_{eff}(h)a}{6h^2} \qquad (2.2)$$

where the Hamaker constant (A_{eff}) is a function of the distance separating the spheres (h). The text of Russel, et al. (1989) contains a good discussion on computing the Van der Waals forces between objects in an aqueous media.

The electrostatic force arises from electric charges acquired on the surface of a particle when in contact with water. The aqueous medium surrounding the particles develops an equivalent charge of opposite sign to maintain electrical neutrality. Electrostatic repulsion occurs when the double layers associated with two surfaces of similar charge overlap. For particles with identical chemistry, this force will always be repulsive, as both particles will acquire a surface charge of the same type (positive or negative). For sphere whose radii are large compared to the double layer, the repulsive force is:

$$F_r = -\frac{64\pi\, 10^3 I}{\kappa} RTa\gamma^2 e^{-\kappa h} \qquad \gamma = \tanh\left(\frac{ze\psi_d}{4kT}\right) \qquad (2.3)$$

where: I is the ionic strength, κ the double layer thickness ($\frac{2.8 \cdot 10^{-10}}{\sqrt{I}}$ m), h the interparticle separation, a the radius, R the gas constant, k Boltzmann's constant, T temperature, ψ_d the diffuse layer potential, z the ionic charge, and e the charge on an electron.

DLVO theory models the net force on two colloidal particles as the arithmetic sum of the attractive van der Waals and repulsive electrostatic forces. If the electrostatic repulsion is sufficiently small, the particles are predicted to stick together (coagulate).

2.7 Sediment Cleaning

Litton and Olsen (1993) compared the effectiveness of different washing procedures for glass-bead media used as collectors in column adsorption experiments. They found that cleaning with a strong acid (HCl) alone did not remove all surface contamination. A combination of washing in strong acid and an aggressive oxidizing procedure (chromic acid or combustion) produced better agreement with theoretical predictions.

Litton and Olsen also found that these washing procedures did not eliminate difficulties in characterizing the glass surface. Zeta potential measurements appeared to vary depending on the wetting and drying histories of the glass beads. A time dependence of the zeta potential was observed, the potential decreasing with time. This was attributed to the growth of a hydration layer at the particles surface from the substitution and inter-diffusion of hydronium ion (H_3O^+) with Na^+ in the glass. They concluded that zeta potential measurements did not necessarily provide an accurate characterization for soda-lime glass beads.

To date, little attention has been paid to the preparation of particle surfaces prior to conducting sediment transport experiments. Exceptions to this are the work of Elyers (1994) and Packman (1997), who investigated the adsorption of metal ions, and capture of clay particles, respectively, in a dune-covered sand bed. A dilute acid wash (10^{-3} M HCl) was used to remove adsorbed ions in multiple washings and rinsings with deionized water.

2.8 Summary

Experiments to determine the critical shear stress of silt-sized sediments indicate a dependence on the bed Reynolds' number (Re*, Figure 2.4) that is not predicted from the simple force balance models. The sediment transport behaviour of silt-sized materials is assumed to be analogous to larger particle sizes; but experimental data are very limited. The criterion for "initiation of motion" has been shown to be an imprecise concept, and requires an associated small but finite transport rate to be definitive. The effect of cohesion in fluid-like muds has been modeled using the yield stress of the sediment, but has generally been ignored in laboratory flume studies. DLVO theory provides a model to predict the characteristics of inter-particle forces; unfortunately, glass beads (used in this work) have been shown to be very difficult to characterize.

3 Modeling

The models presented in this chapter were developed to provide insight into the basic physical and chemical processes affecting the mobility of silt-sized sediment. Section 3.1 presents a dimensional analysis of the initiation of motion problem, which develops a sediment transport rate parameter applicable to silt-sized particles in water. The nature of the fluid forces exerted on a sediment grain is found from scaling the Navier-Stokes equations in Section 3.2. The effect of turbulent bursting processes on particle mobility is examined in Section 3.3. In Section 3.4, the effect of the viscous sublayer is included in a traditional force balance model, which is then used to gain an estimate of the critical condition. Section 3.5 presents a model of the inter-particle forces.

3.1 Dimensional Analysis for Critical Shear

The critical shear stress (τ_c) is the shear required to produce movement of the surface grains on a bed of similar particles. In general,

$$\tau_c = \varphi(d, \mu, g, \rho_s, \rho), \tag{3.1}$$

where φ indicates a functional relation of the included variables, and

τ_c	$[M/LT^2]$	critical bed shear stress
d	[L]	particle diameter, nominal if non-spherical
μ	[M/LT]	fluid viscosity

g	$[L/T^2]$	gravitational acceleration
ρ_s	$[M/L^3]$	sediment density
ρ	$[M/L^3]$	fluid density

where M represents mass; L, length; and T, time. The size distribution and particle shape (geometry) are not considered for this analysis. Using the Buckingham-PI theorem, the critical shear relationship can be expressed in terms of three dimensionless groups:

$$\tau^*_c = \varphi(Re^*, \rho_s/\rho) \qquad (3.2)$$

where the three dimensionless parameters are:

Shields' Parameter, $\tau^* = \dfrac{\tau_c}{(\rho_s - \rho)gd}$

Bed Reynolds' Number, $Re^* = \dfrac{u^* d}{\nu} = \dfrac{\sqrt{\tau\rho}\, d}{\mu}$

Density Ratio (solid:fluid), ρ_s/ρ

and $\tau = \rho u^{*2}$. The bed Reynolds number (Re*) is 11.6 times the ratio of the particle diameter to the thickness of the viscous sublayer ($11.6\nu/u^*$).

The density ratio represents the importance of moving particles that transfer momentum to other particles on the sediment bed; this ratio is important at large values (e.g., air/sand system). However, for solids in water flows, the density ratio is closer to 1 and not large enough for the particle momentum to be important. It is typically neglected for all bed Reynolds number flows in water.

For small bed Reynolds numbers a limiting case for the dependence of the critical shear stress can be obtained. In analogy to Stokes flow around a single sphere, small

Reynolds numbers imply viscous forces dominate over inertial forces. In the dimensional analysis, fluid density represents inertial fluid forces and is thus neglected in the analysis.

The weight of the particle is the force opposing motion and is included as a unit weight $(\rho_s-\rho)g$. These simplifications result in

$$\tau_c = \varphi(d, \mu, (\rho_s-\rho)g) \tag{3.3}$$

By applying the Buckingham-PI theory, the Shields' Parameter becomes constant.

$$\tau^*_c = \frac{\tau}{(\rho_s - \rho)gd} = \text{constant (independent of } \mu), \tag{3.4}$$

and is independent of other parameters. Since it is not possible to create a dimensionless group from these four parameters involving the viscosity (μ), the only possible dimensionless group is τ^*_c which is independent of the viscosity. Since the bed Reynolds' number ($u^*d/\nu = \rho u^*d/\mu$) contains the viscosity, it follows that the dimensionless critical shear stress (τ_c^*) can not be a function of the bed Reynolds number (as implied by many others).

An alternative view of this limiting case is that the viscous sub-layer is much thicker than the particle diameter, so variations in the sublayer thickness have no effect on the particles. Since the bed Reynolds number (Re^*) is a ratio of particle diameter to the viscous wall unit ν/u^* (the viscous sub-layer is ~$11.6\ \nu/u^*$), the critical condition is independent of Re^*, when $Re^* < 1$.

3.2 Sediment Transport Rate Parameter

Experimentally, the critical condition can not be measured directly; it may only be bounded. If no particles are observed to be in motion, the shear stress is below critical; if

particles are observed to move, the shear stress exceeds the critical level. As a result, reported critical shear stresses correspond to a finite amount of sediment transport, often described qualitatively. Since different investigators have used differing definitions of the threshold condition, different studies are difficult to compare. Vanoni (1964) demonstrated that differing assumptions on the amount of transport would change the critical shear stress by a factor of two to three.

Quantifying the erosion and transport rate of particles overcomes this difficulty. The sediment transport rate (q_s) used here is taken on a bulk volume basis, and corresponds to the bulk volume of sediment moved per unit width. The equivalent mass transport rate is $q_s \cdot \rho_s \cdot (1-\theta)$, where θ is the porosity of the sediment bed ($\theta \sim 0.4 - 0.5$).

Including the sediment transport variable q_s, (units: $[L^2/T]$) in the dimensional analysis for fine grained sediments ($Re^* < 1$) yields the functional relationship:

$$q_s = \varphi(\tau, d, \mu, (\rho_s-\rho)g)$$

or

$$q_s^* = \varphi(\tau^*) \tag{3.5}$$

where

$$q_s^* = \frac{q_s \mu}{\tau d^2} \tag{3.6}$$

This dimensionless group for sediment transport is different from the usual, and is suitable only for low bedload transport rates of non-cohesive silt-sized material ($Re^* < 1$). In Chapter 5 it will be shown that this parameter and Equation (3.5) work well for the observed data.

3.3 Physical Interpretation of q_s^*

The dimensionless sediment transport parameter, q_s^*, will now be shown to be proportional to the fraction of the bed in motion under the following assumptions:

- The flow is steady, incompressible, and is a fully developed turbulent channel flow.
- Particles are of uniform size and shape, smaller than the viscous sublayer thickness.

Consider an area of the bed L x W, in which a fraction, n, of the surface particles are in motion at any given time. In this area there are ~ $\frac{LW}{d^2}$ particles, so $n\frac{LW}{d^2}$ particles are moving. Each particle has a volume, $\frac{\pi}{6}d^3$, and moves with a velocity U_{bed}. U_{bed} is the characteristic (mean) velocity of the particles rolling along the bed, assumed to be the unperturbed fluid velocity at the particle's centroid. The time required for all of the moving particles to move off the selected area is then L/U_{bed}.

Thus the transport rate is:

$$\frac{volume}{unit\ time} = n\frac{LW}{d^2}\frac{\pi}{6}d^3\frac{U_{bed}}{L} = n\frac{\pi}{6}WdU_{bed} \tag{3.7}$$

Expressed as a bulk volume per unit width,

$$q_s = \frac{bulk\ volume}{unit\ width \bullet unit\ time} = \frac{Q_s}{W} = n\frac{\pi}{6}dU_{bed}\frac{1}{(1-\theta)} \tag{3.8}$$

where θ is the porosity of the sediment, and $(1-\theta)$ the solid fraction.
Under the assumption that the particles move with the fluid velocity, $U_{bed} = u(y = d/2)$, and the velocity profile for the viscous sublayer,

$$u(y) = u^{*2}y/\nu$$

then $U_{bed} = u^{*2}d/2\nu$, so

$$q_s = n\frac{\pi}{6}d\frac{du^{*2}}{2\nu(1-\theta)} = n\frac{\pi}{12(1-\theta)}\frac{d^2u^{*2}}{\nu} \tag{3.9}$$

For $\theta = 0.48$,

$$q_s \approx \frac{n}{2}\frac{d^2u^{*2}}{\nu}$$

The dimensionless transport rate parameter q_s^* becomes

$$q_s^* = \frac{q_s\mu}{\tau d^2} = n\frac{\pi}{12}\frac{d^2u^{*2}}{(1-\theta)\nu}\frac{\mu}{\tau d^2} = n\frac{\pi}{12(1-\theta)} \tag{3.10}$$

$$\approx \frac{n}{2}$$

Thus q_s^* is directly proportional to the fraction of bed surface (n) that is in motion. For example, if $q_s^* = 0.01$, then $n \sim 0.02$, or 2% of the bed is in motion.

3.4 Scaling of Navier-Stokes Equations

Turbulent bursts and sweeps of fluid have been shown to be responsible for initiation of motion (Vanoni, 1964). The scaling analysis of the Navier-Stokes equations presented here provides some insight into how the forces associated with these bursts affect silt-sized sediments.

The Navier-Stokes equation is:

$$\rho\frac{\partial \mathrm{v}}{\partial t} + \rho\mathrm{v}\cdot\nabla\mathrm{v} = \mu\nabla^2\mathrm{v} - \nabla p + F_{ext} \tag{3.11}$$

where v = v(x, y, z, t) is the local velocity vector field. We retain the acceleration term due to the unsteady nature of the turbulent fluctuations. Choosing the characteristic scaling quantities as:

V - characteristic velocity

T - characteristic time scale

d - characteristic length scale (particle diameter)

and the pressure fluctuations are made dimensionless by: $(p-p_o)\, d/(\mu V)$

$$\rho\frac{V}{T}\frac{\partial \mathrm{v}^*}{\partial t^*}+\rho\frac{V^2}{d}\mathrm{v}^*\cdot\nabla^*\mathrm{v}^*=\mu\frac{V}{d^2}\nabla^{*2}\mathrm{v}^*-\mu\frac{V}{d^2}\nabla^* p^*+F_{ext}^* \tag{3.12}$$

$$\frac{\rho d^2}{\mu T}\frac{\partial \mathrm{v}^*}{\partial t^*}+\frac{\rho V d}{\mu}\mathrm{v}^*\cdot\nabla^*\mathrm{v}^*=\nabla^{*2}\mathrm{v}^*-\nabla^* p^*+F_{ext}^*$$

where v* is the dimensionless velocity field. When the two Reynolds numbers associated with the terms on the left-hand side are small compared to one, the terms drop out and the equation reduces to that for (quasi-steady) Stokes flow. These Reynolds numbers will now be examined in detail.

First consider the advective inertial term: $\frac{\rho V d}{\mu}\cdot O(1)$, and take the characteristic velocity $V = u_{fluid}$ at $y = d$. Since the particles were assumed to be within the viscous sublayer, we obtain:

$$u_{fluid}=\frac{du^{*2}}{\nu}$$

Therefore,

$$\frac{\rho V d}{\mu}=\frac{V d}{\nu}=\frac{u^{*2}d^2}{\nu^2}=\left(\mathrm{Re}^*\right)^2,$$ where Re* is the bed Reynolds number.

Thus if $(Re^*)^2 << 1$, this term is negligible.

Next, consider the unsteady term of Equation (3.12). If the time scale is taken to be the ratio of length and velocity scales, T = Length/Velocity = d/V, then:

$$\frac{\rho d^2}{\mu\tau} = \frac{\rho d^2}{\mu d/V} = \frac{\rho V d}{\mu}$$

which is the same condition as the advective inertial term; $(Re^*)^2 << 1$ to be negligible. Alternatively, if the time scale is taken to be the time between turbulent bursts, the period between bursting events is approximately (50-100) ν/u^{*2} (Kim, 1971). This gives:

$$\frac{\rho d^2}{\mu\left(50\frac{\nu}{u^{*2}}\right)} = \frac{u^{*2}d^2}{50\nu^2} = \frac{1}{50}\left(\mathrm{Re}^*\right)^2$$

which is no more restrictive than the inertial condition, provided $du^*/dt^* < O(50)$, which is certainly true in our case.

This scaling analysis suggests that the unsteady inertial contribution (or the added mass) due to boundary layer bursting events can be neglected for small bed Reynolds number flows. Thus the quasi-steady Stokes Equation,

$$0 = \nabla^{*2}\mathrm{v}^* - \nabla^* p^* + F^*_{ext} \qquad (3.13)$$

applies even if there are turbulent sweeps or bursts, because only the viscous force on particles (and pressure distribution due to viscous shear) is significant, and not the inertial terms. This allows a simplified stochastic model of turbulence to be applied to this problem, as detailed in the next section.

3.5 Turbulence Modeling

3.5.1 Turbulent Shear Distribution

The proceeding scaling analysis does not imply that boundary layer bursting processes are unimportant, but rather that a stochastic view of them is sufficient (i.e., quasi-steady). The probability distribution of the wall shear stress, τ, was measured by Alfredsson, *et al.* (1988), who recommended the following parameters:

Standard deviation, σ =0.4

Skewness, $\beta_1 = 1.0$

Kurtosis, $\beta_2 = 4.0$

Figure 3.1 illustrates the nature of the shear distribution with a Pearson type IV probability distribution fit to the parameters listed above. Notice that the distribution is skewed towards the occurrence of higher shear stresses. This distribution implies that the instantaneous bed shear stress exceeds twice the mean shear more than 2% of the time.

3.5.2 Resuspension

Given that that the flow field surrounding the particle is Stokesian, then a criterion for resuspension may be defined as the local fluid velocity normal to the bed must be greater than the particle's settling velocity ($V_f > Ws$). An estimate of the normal fluid velocity, obtained from flat plate/pipe boundary layer measurements (Cleaver and Yates, 1972), is:

$$\frac{\sqrt{v'^2}}{u^*} \approx 0.01 y_+^2, \; y_+ < \sim 6$$

where $y_+ = \frac{yu^*}{\nu}$.

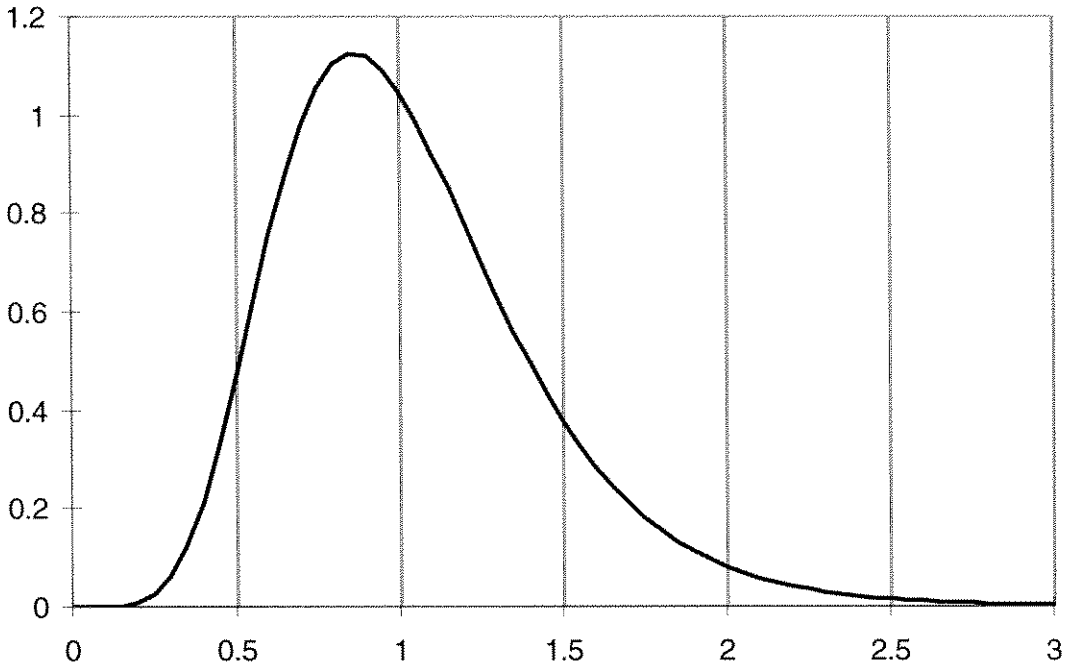

Figure 3.1: Wall shear stress distribution (s = 0.4, β_1 = 1.0, β_2 = 4.0) fit by a Pearson type IV probability distribution. The mean is 1, as is the area under the curve.

If V_{max} is assumed to be $3\sqrt{\overline{v'^2}}$ (representing ~0.1% probability of occurrence), then $V_{max} = 0.03\ y_+^2\ u^*$. With the approximation, y = d, the critical condition for entrainment into the mean flow becomes:

$$W_S = V_{\max} \Rightarrow \frac{(\rho_s - \rho)gd^2}{18\,\mu} = 0.03\left(\frac{du^*}{\nu}\right)^2 u^*$$

$$\frac{1}{18 \cdot 0.03}\frac{\nu}{du^*} = \frac{\rho u^{*2}}{(\rho_s - \rho)gd}$$

$$\tau^* = \frac{1}{0.54\,\mathrm{Re}^*} = \frac{1.85}{\mathrm{Re}^*} \qquad (3.14)$$

For $Re^* < 1$, this condition requires τ^* be greater than 2.

3.5.3 Turbulent Pressure Fluctuations

Because the sediment bed is porous, the turbulent pressure fluctuations in the fluid flow create local pressure gradients, which induce flow in the bed. The lift force on a particle at the bed's surface, due to a turbulent pressure fluctuation, will be shown to be less than 1% of the particle's weight, and is thus neglected from further consideration. From turbulence literature (Willmarth, 1975):

$\Delta p_{rms} \sim 3\ \tau_w$

and the horizontal separation between high and low pressure flucuations on a wall boundary is: $\lambda+ = \lambda u^*/\nu \sim 150$. Taking $\Delta p_{max} \sim 3\ \Delta p_{rms}$, then $\Delta p_{max} \sim 9\tau_w \sim 10\tau_w$.

The criterion to lift a particle from the bed is that the upward force on a single particle at the surface of the sediment bed must exceed the particle's weight. The pressure gradient, Δp, across a single particle is $\Delta p_{max} D/L$; L = distance between p_{max} and p_{min}, about $150(\nu/u^*)$.

$$F_p \approx \Delta p \frac{\pi}{4} D^2 \approx \Delta p_{\max} \frac{Du^*}{150\upsilon} \frac{\pi}{4} D^2$$

$$\frac{F_p}{F_g} = \frac{\Delta p_{\max} \dfrac{Du^*}{150\upsilon} \dfrac{\pi}{4} D^2}{\dfrac{\pi}{6}\left(\rho_s - \rho\right) g D^3} = \frac{1}{100} \frac{10\tau_w}{\left(\rho_s - \rho\right) g D} \frac{Du^*}{\upsilon}$$

$$\frac{F_p}{F_g} = \frac{1}{10} \tau^* \mathrm{Re}^* \qquad (3.15)$$

For fine sediments, $Re^* < 1$, the force resulting from turbulent pressure fluctuations does not exert any significant lift on the particle, because $\tau^* \sim 0.05 - 0.1$ for critical shear

stress. However, for materials with a much higher critical shear stress, such as consolidated clays, this term has been found to be important (Raudkivi, 1991).

3.6 Force-Balance Model for Initiation of Motion

The critical condition is obtained from a force balance by determining the fluid forces required to move the least stable particle on a sediment bed. The computation of forces on an individual particle is highly dependent on the localized geometry surrounding the particle. The random nature of a packed bed creates difficulties in specifying the geometry associated with a critical particle. Nonetheless, consideration of an idealized particle geometry provides an estimate of the critical shear stress, and its functional relationship to particle and fluid characteristics.

Cases (a) and (b) in Figure 3.2 depict the results of exact analytical solutions to Stokes flow around a sphere (or hemi-sphere) in a linear shear flow. The purely viscous flow results in zero lift force, but a significant torque acts on the particle, in addition to the drag force. This torque is represented by a displacement h*a of the drag force from the center of mass. Case (c) represents the viscous drag on an area πa^2, as an approximation for a sphere that does not protrude into the flow. Cases (a) and (c) are the limiting conditions, and the actual value is anticipated to be between cases (b) and (c).

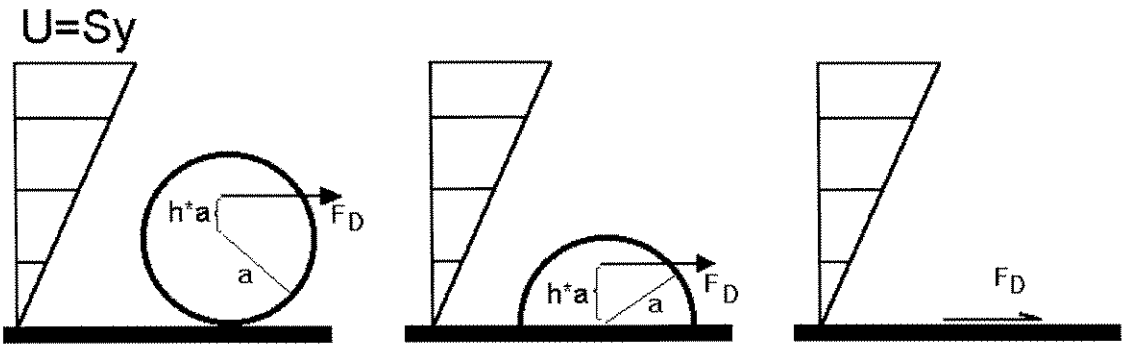

(a) Sphere on wall	(b) Hemisphere on wall	(c) wall only
$F_D = 10.203\pi\mu a^2 \cdot S$	$F_D = 4.30\pi\mu a^2 \cdot S$	$F_D = \pi\mu a^2 \cdot S$
$F_L = 0$	$F_L = 0$	$F_L = 0$
$h^* = 0.37$	$h^* = 0.5674$	$h^* < 1.0$
(O'Neill, 1968)	(Price, 1985)	

S = shear rate [1/T]

Figure 3.2: Particle geometry considered for drag force estimation.

The viscous drag force on a bed particle acts predominately on the area of the particle that protrudes into the flow. The fluid velocity within the interstitial matrix of the bed is much smaller and contributes a negligible amount to the total drag force. The idealized geometries of Figure 3.2 capture this important characteristic, account for the particle's protrusion into the shear layer, and provide a reasonable estimation of the drag force.

Now we consider the balance of viscous and gravity forces for a sphere resting on other spheres as pictured in two-dimensions in Figure 3.3. Experiments utilizing a tilting plate covered with a fixed layer of grains estimated the contact angle (ϕ) as: 50° for spheres, 60° for natural material, and 70° for angular grains (Miller & Byrne, 1966),

where ϕ is defined from the vertical. This angle is different from the angle of repose, and meant to estimate the angle at which a particle in the upper layer of a stream bed makes contact with the particle downstream of it.

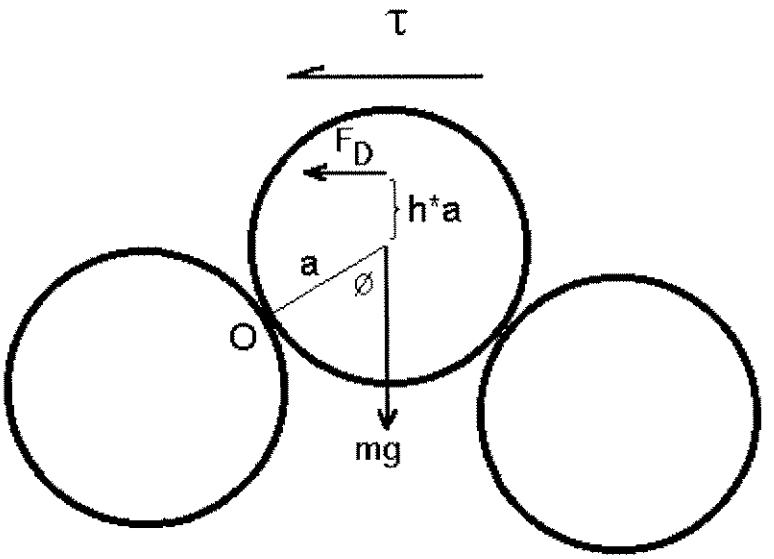

Figure 3.3: Geometry for force balance analysis

The critical condition occurs as the drag force begins to make the particle roll about point O, shown in Figure 3.3. Thus the normal force from upstream grain is zero (lift off). The sum of the moments about point O:

$$\Sigma M_O = 0 = F_g\, a \sin\phi - F_D(a\cos\phi + a\, h^*)$$

With β defined by $F_D = \beta\cdot\pi\mu a^2\cdot S = \beta\cdot\pi a^2\cdot\tau$, this equation can be used to derive the dimensionless shear stress (Shields' parameter) as follows:

$$\tfrac{\pi}{6}(\rho_s - \rho)gd^3 \sin\phi = \beta\, \pi\, a^2 \tau\, (\cos\phi + h^*)$$

$$\tau_c^* = \frac{\tau}{(\rho_s - \rho)gd} = \frac{2}{3}\frac{\sin\phi}{\beta(\cos\phi + h^*)} \qquad (3.16)$$

This model also predicts τ_c^* ~ constant, in the range of bed Reynolds numbers $Re^* < 1$, which agrees with the dimensional analysis. For the case of drag calculated assuming the grain is a hemisphere (Figure 3.2b), $\beta = 4.3$, $h^* = h/a = 0.57$, and assuming $\phi = 60°$, Equation (3.16) gives $\tau_c^* = 0.13$. In this example, a typical value of the contact angle ($\phi = 60°$) was taken from the values reported by Miller and Byrne (1966).

Here τ is the instantaneous shear force acting on the bed. Treating turbulent bursts in a quasi-static manner, and using the probability distribution given in Section 3.3.1, the instantaneous shear has a probability of exceeding 2.87τ of about 0.001. Substituting this into equation (3.16) gives:

$$\bar{\tau}_c^* = \frac{\tau}{2.87(\rho_s - \rho)gd} = \frac{\sin\phi}{4.3\beta(\cos\phi + h^*)}$$

which for $\beta = 4.3$, $h^* = 0.57$, and $\phi = 60°$ gives a critical condition of $\tau_c^* = 0.044$.

This result required the estimation of many geometric variables, which, due to wide variations in the local packing geometry, cannot be determined with sufficient accuracy to give a definitive prediction of τ^*. For the simple geometry considered here, the contact angle $\phi = 60°$ implies that half the particle protrudes into the flow, which corresponds to the hemispherical geometry used to estimate the β and h^* parameters.

Table 3.1 illustrates the sensitivity of the critical shear stress to these geometric variables and the amount of transport deemed critical. Within the range of expected contact angles (ϕ), τ^* increases by 40%. Rows one through three illustrate the sensitivity of the critical mean shear to the amount of motion, as indicated by the probability of the instantaneous shear stress exceeding the critical value. The ratio of the critical shear stress to the mean shear varies from 1.5 to nearly 3, increasing as the probability of

motion decreases. An increase in the magnitude of the drag force (row four) decreases the critical shear stress by the same proportional amount, while assuming the drag force acts through the particle's center of mass (h* = 0) more than doubles the calculated critical shear stress. The variation in the estimated critical shear stress from these parameters indicates that the point of action of the drag force, plus reasonable estimates for the particle geometry are required in a model of the sediment mobility. This is discussed in the next section to create a sediment transport rate model.

Probability of motion	τ/τ	β	h*	τ_c* Critical Shear Parameter		
				Contact angle ϕ		
				50°	60°	70°
0.001	2.87	4.3	0.57	0.034	0.044	0.055
0.01	2.2	4.3	0.57	0.044	0.057	0.072
0.1	1.5	4.3	0.57	0.065	0.083	0.106
0.01	2.2	5.2	0.57	0.037	0.047	0.060
0.01	2.2	4.3	0	0.084	0.122	0.194

Table 3.1: Sensitivity of the predicted dimensionless critical mean shear stress τ_c* to geometric assumptions. ϕ = contact angle; β, h* = relative magnitude and location of drag force; p = probability of instantaneous shear exceeding critical shear.

3.7 Sediment Transport Rate Model

A simple model was developed to predict the sediment transport rate based on simplistic arguments about the physical nature of the sediment bed and transport

processes. The important physical processes identified in this chapter are incorporated into the model, which displays the correct scaling relationships. As a result, it provides a basis for comparison with experiments for non-cohesive sediment beds, and a prediction of the influence of cohesion on the sediment transport rate.

This model has three main components. First, the variation in turbulent shear stress is modeled as a completely stochastic process; so the model computes the transport rate at all shear stresses and weights each transport rate by the probability of occurrence of each shear stress. Second, the bed stability is modeled by a distribution of particle positions about the mean bed level. The torque required to roll a particle is estimated from the fluid drag force acting on particles, accounting for their protrusion and the corresponding geometric position. Third, cohesion is included as a single additional force acting normal to the bed and stabilizing the particles.

The model assumes that the particles are submerged in the viscous sublayer ($Re^* < 1$). The flow is turbulent, and the shear stress distribution shown in Figure 3.1 is applicable. Sediment transport rates for different shear stresses are computed, weighted by the probability of that shear stress occurring for the given mean shear stress, and integrated over all shear stresses.

To determine the fraction of the sediment bed that is mobile (n) under a given shear stress, information on the particle geometry is required. Lacking better knowledge, the following simple model was used.

In a unit area of this hypothetical sediment bed, there are $1/d^2$ 'cells', each of which contains one particle. The sediment bed is assumed to be flat within +/-d (one particle diameter). Each particle (or cell) is assigned a height (elevation) relative to this

level bed. The particle's height normalized by the diameter is denoted δ, and indicates the non-dimensional distance from the particle's center to the center of another particle at the mean bed elevation. In essence, it is assumed that the particles immediately upstream and downstream are at the mean bed elevation. The probability distribution of heights is assumed to be a uniform distribution (equal probability of particle heights from –d to +d).

Particles with negative heights will never erode, since they are overtopped by their neighboring, less stable particles. Another particle is allowed to occupy the space above each particle, if this space provides a stable position. If the original particle has a relative elevation of δ, the new particle is assigned a height of 1 + δ. The first process that was assumed was the most unstable particles would relocate to occupy more stable 'sites' present on the bed. The modification in the distribution of particle heights is illustrated in Figure 3.4

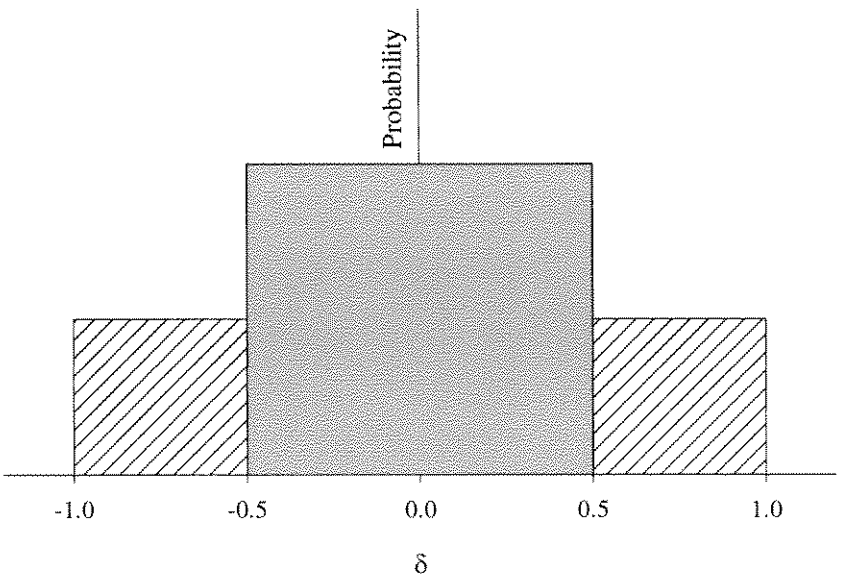

Figure 3.4: Modification of particle height distribution, as particles move to more stable sites. δ is the particle height normalized by the diameter. The hatched area is the assumed initial distribution, the grey area the distribution of particle heights after the particles relocate.

This idea could be applied to other distributions in addition to the uniform distribution assumed here. This was not done because (a) of the lack of specific knowledge of the bed state, nor the appropriateness of this cell-type model was known, and (b) the process of redistributing the particles to fill empty 'sites' will move an assumed distribution towards a more uniform one.

Stationary particles on the bed are assumed to experience a force/torque that corresponds to their protrusion from the bed. The results compiled in Figure 3.2 were used to develop a correlation between particle protrusion and shear stress. For a sphere level with the bed, similar to case (c), h* or h/a was assumed to be 0.75 to give a linear relation between h* and δ. This resulted in the relation:

$$h^* = h/a = 0.75 - 0.38\,(\delta)$$

The drag force was fit with a quadratic polynomial of the particle elevation:

$$F_D = \beta\,\pi\,a^2\,\tau \qquad \beta = 1 + 4\,\delta + 5.2\,\delta^2$$

These parametrizations are compared in Figure 3.5 to the exact results from Figure 3.2.

A particle was considered stable if the torque due to fluid shear was less than that due to gravity:

$$Fx = mg\frac{\sin\phi}{h^* + \cos\phi} = mg\frac{\frac{2}{\sqrt{3}}\left(\frac{3}{4} - \delta^2\right)^{1/2}}{0.75 - 0.38\delta + \frac{2}{\sqrt{3}}\delta} \tag{3.17}$$

$$= \frac{\pi}{6}\left(\rho_s - \rho\right)D^3\frac{\left(\frac{3}{4} - \delta^2\right)^{1/2}}{0.65 + 0.67\delta}$$

$$Fx = \tau_{bed}\frac{\pi}{4}D^2\left(1 + 4\delta + 5.2\delta^2\right) \tag{3.18}$$

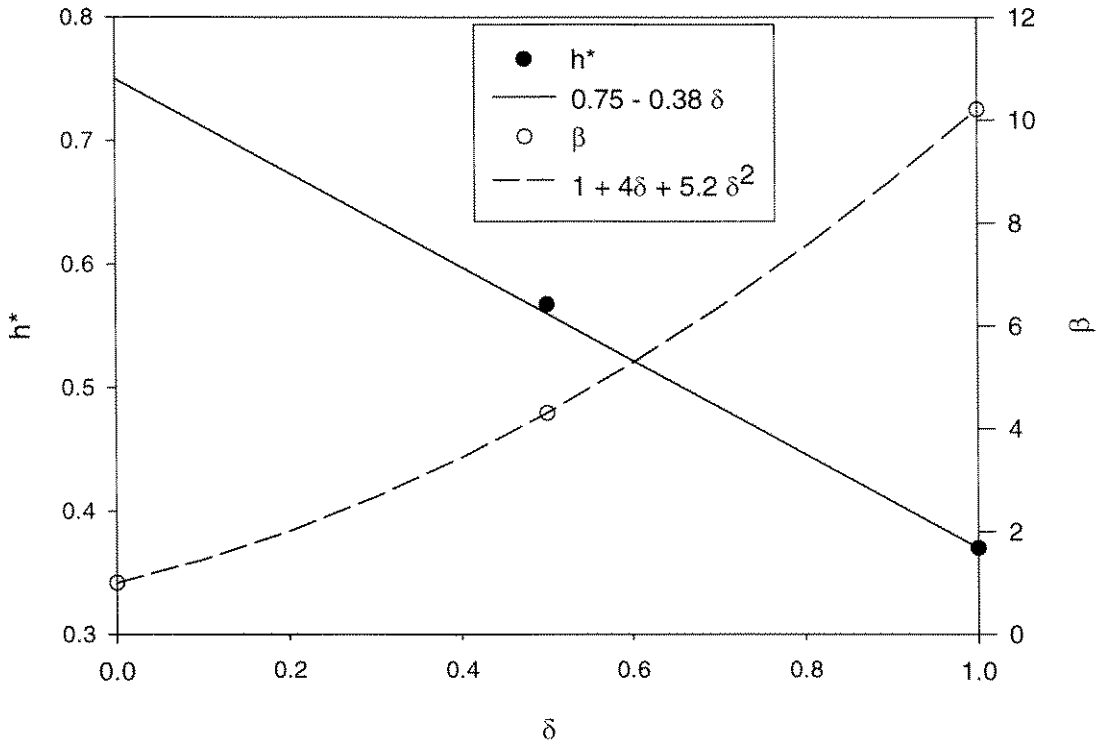

Figure 3.5: Parametrizations used for drag force (β) and moment arm (h*). The symbols correspond to the exact solutions given in Figure 3.2.

The contact angle ϕ is given by assuming the downstream 'particle' actually represented the gap between two touching, adjacent particles. This computation allows the height of the least stable particle to be determined. All particles with a lower height are stable, while all 'cells' that contained particles with a higher elevation will be in motion.

Since the velocity profile is assumed to be independent of the presence of particles, particles are transported with the fluid velocity one radius above the bed. Since the particles are within the viscous sublayer, $\tau = \mu\, du/dy$ and the velocity at d/2 is:

$$V_p = \frac{\tau d}{2\mu}$$

The transport rate is the fraction of bed in motion multiplied by the particle's velocity. To convert this back to a bulk volume of particles (to correspond with q_s^*), the number of particles per unit area was $1/d^2$, and the volume per particle is $1/d^3$, so

$$q_s = V_p \frac{n}{d^2} d^3 = \frac{\tau d}{2\mu} nd$$

$$q_s^* = \frac{q_s \mu}{\tau_o D^2} = \frac{n}{2}$$

For example, the value of $q_s^* = 10^{-2}$ corresponds to n = 0.02, or 2% of the surface grains in motion.

To summarize, the model used an assumed uniform distribution of particle elevations about a mean to compute the fraction (n) of the bed in motion under a given shear stress. This was converted into the dimensionless transport rate, and weighted by

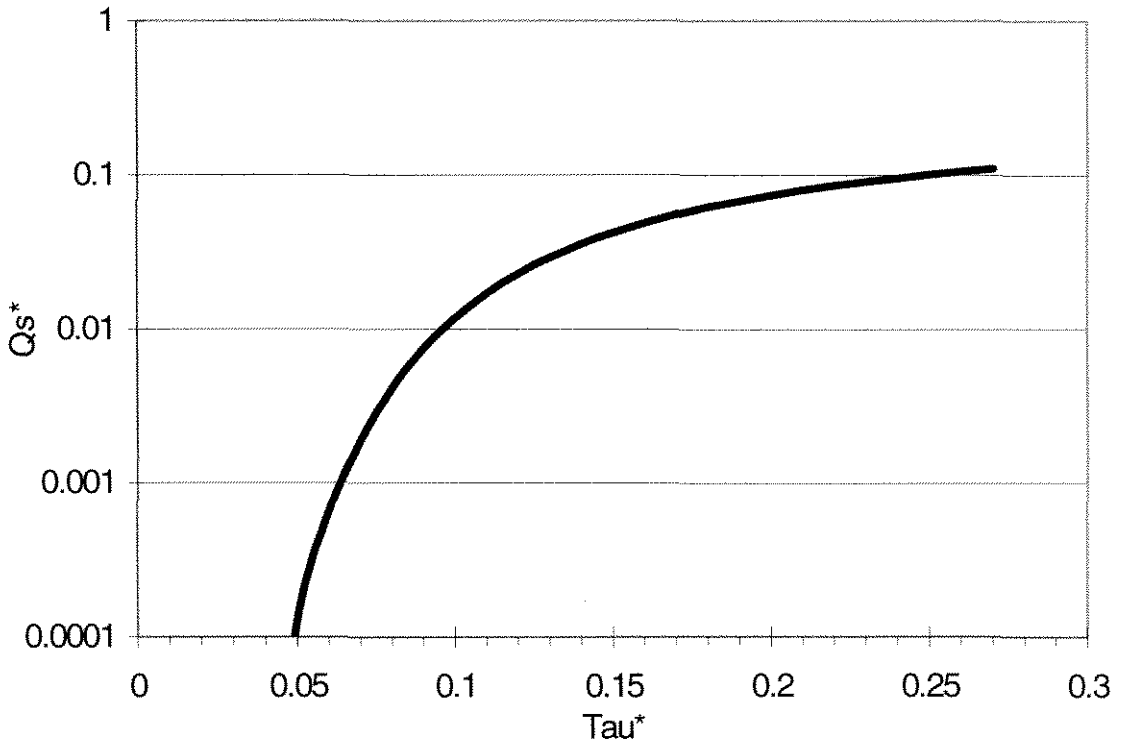

Figure 3.6: Dimensionless transport rate as predicted by the model for a non-cohesive material (Re* < 1).

the probability (Figure 3.1) of occurrence of that shear stress. The final transport rate is the sum over all shear stresses and is shown in Figure 3.6 for non-cohesive particles.

The model incorporates cohesion as a single force acting normal to the bed. This parameter should correspond to the cohesive force between two particles and the number and geometric arrangement of neighbouring particles. To determine if a particle will roll from its position, the moment of the cohesive force about the point of contact is required. For modeling purposes, the net cohesive force was assumed to act through the particle's centroid, in the same direction as gravity, so that equation (3.17) becomes:

$$Fx = (mg + Fc)\frac{\sin\phi}{h + \cos\phi} = (mg + Fc)\frac{\frac{2}{\sqrt{3}}\left(\frac{3}{4} - \delta^2\right)^{1/2}}{0.75 - 0.38\delta + \frac{2}{\sqrt{3}}\delta} \qquad (3.19)$$

$$= \left(\frac{\pi}{6}(\rho_s - \rho)D^3 + Fc\right)\frac{\left(\frac{3}{4} - \delta^2\right)^{1/2}}{0.65 + 0.67\delta}$$

The cohesive force, Fc, may be normalized by the particle's weight to produce the dimensionless term:

$$Fc^* = \frac{Fc}{\frac{\pi}{6}(\rho_s - \rho)gD} \qquad (3.20)$$

The model predictions of the dimensionless transport rate for four values of this cohesive force parameter are shown in Figure 3.7. Increasing values of Fc* result in a decrease of the transport rate, which is relatively less at higher shear stresses.

A modeling approach to predict the cohesive force between particles in discussed in the next section.

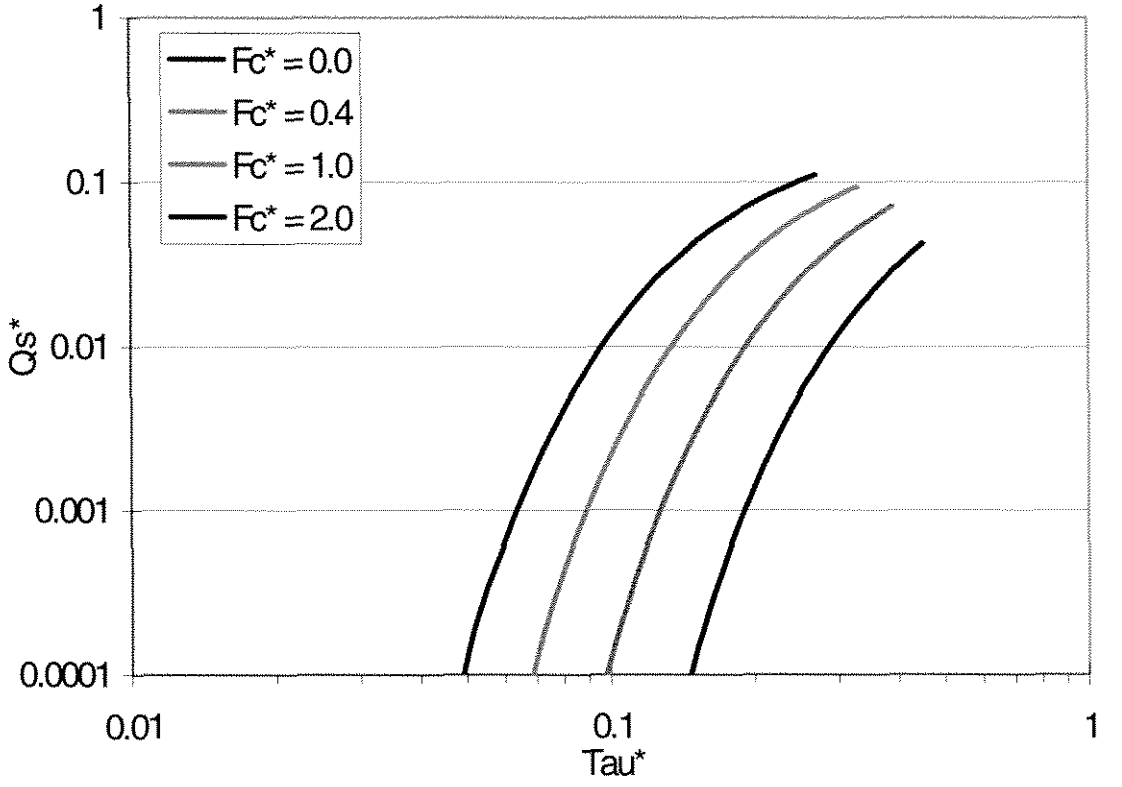

Figure 3.7: Dimensionless transport rate (qs*) vs. dimensionless shear stress (τ*) as predicted by model for materials of varying cohesion (Fc*).

3.8 Modeling of Inter-particle Forces

To estimate the cohesive forces, the interaction between two ideal, spherical particles was modeled using DLVO theory. DLVO theory originally was constructed to explain and predict colloidal stability and flocculation, as the combination of electrostatic repulsion and van der Waals attractive forces. Colloidal stability is interpreted in terms of the predicted potential energy: a primary minimum, a repulsive barrier, and, under some conditions, a secondary minimum. Originally, it was thought that the secondary minima predicted to occur in DLVO theory could account for the cohesive behaviour of

silt-sized particles. However, for the particle sizes considered here (d > 10 μm), the net attractive force is not significant relative to the particle's weight. The alternative explanation, that the particles overcome the repulsive barrier and are attracted to each other in the primary minimum, is explored.

Quartz or silica surfaces possess a pH_{pzc} ~ 2.0 (Stumm & Morgan, 1981), resulting in an electrostatic repulsion at the pH's of interest. DLVO theory predicts that electrostatically repulsive particles may be attracted to each other in a weak secondary energy minimum. To compute the maximum attractive force associated with the secondary minimum, consider the two isolated spherical particles in Figure 3.8.

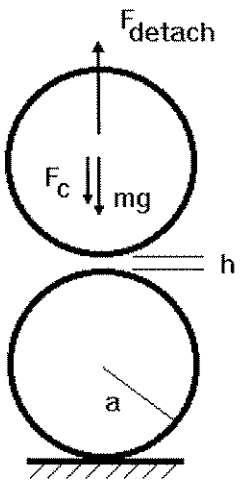

Figure 3.8: Modeled geometry for van der Waals forces.

The electrostatic repulsion between the two particles is:

$$F_r = -\frac{64\pi 10^3 I}{\kappa} RTa\gamma^2 e^{-\kappa h} \qquad \gamma = \tanh\left(\frac{ze\psi_d}{4kT}\right) \tag{3.21}$$

and the van der Waals attraction is given by:

$$F_a = \frac{A_{11(2)}a}{12h^2} \tag{3.22}$$

where: I is the ionic strength, h the interparticle separation, a the radius, A, Hamaker's constant, R the gas constant, ψ_d the diffuse layer potential, z the ionic charge, and e the charge on an electron.

At separations larger than about 5 nm, the van der Waals force is retarded due to two factors: screening from aqueous ions and the finite propagation time of electromagnetic waves. The expected separation distances between these particles means that equation (3.22) can not be used without some modification, and therefore Hamaker's constant (A) is redefined as an effective value $A_{eff}(h)$. Details of this modeling are given in Appendix A, and the results are summarized in Figure 3.9 as a function of the diffuse potential. The attractive force predicted from the secondary minimum is a few percent of the particle's self-weight, while the repulsive barrier is several times the particle's weight for potentials above 20 mV. This is expected to be the case for the experimental conditions in this work.

The forces predicted above scale with the particle diameter. The more general result, that the cohesive force scales with the particle diameter, is given below. This requires that the interaction distance of the surface force, typically several nanometers, is much smaller than the particle radius, 10's of micrometers for silt-sized material. Under these conditions, the interaction between two object becomes essentially one-dimensional, so the interaction potential can be found by integrating the potential for flat plates, evaluated at the local surface-to-surface separation, over the entire gap (the Derjaguin approximation, see Russel *et al.*, 1989). The interaction energy for two

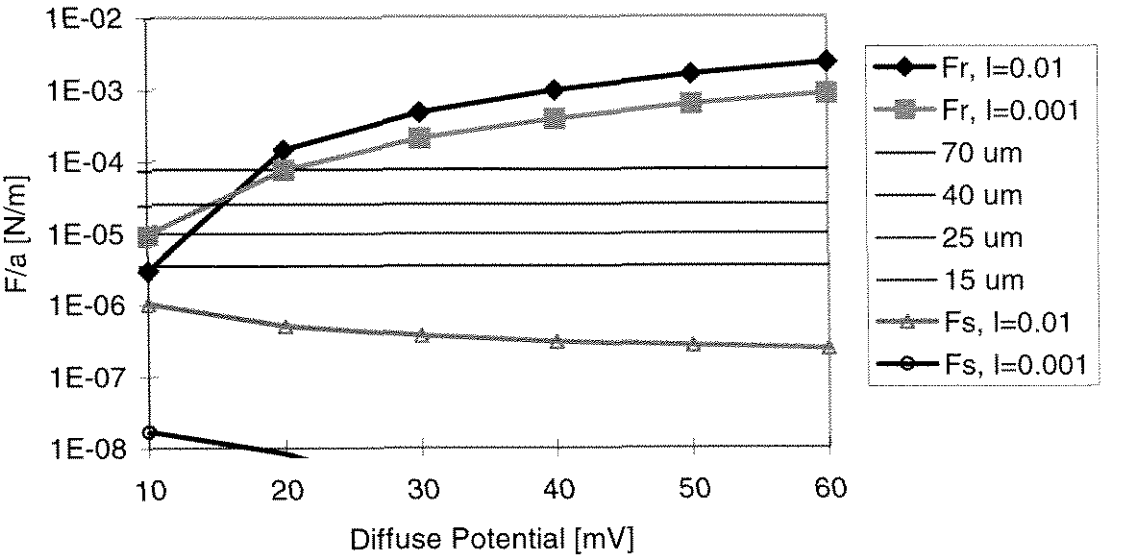

Figure 3.9: Attractive and repulsive forces between two spheres from DLVO theory. Fr -maximum repulsive force, Fs- maximum attractive force (secondary minimum) I - ionic strength [M]. The particle weights, normalized by their radius, are shown as horizontal lines.

spheres of radius a_1 and a_2 can be expressed in terms of the energy per unit area of a flat plate, Φ_{fp}, as:

$$\Phi \approx 2\pi \int_0^\infty \Phi_{fp}(z) r dr \approx 2\pi \frac{a_1 a_2}{a_1 + a_2} \int_h^\infty \Phi_{fp}(z) dz \tag{3.23}$$

where z is the separation and r the radial distance in cylindrical co-ordinates. Thus the force is

$$F = -\frac{\partial \Phi}{\partial h} \approx 2\pi \frac{a_1 a_2}{a_1 + a_2} \Phi_{fp}(h) \tag{3.24}$$

Thus, if the force resulting from the chemical interactions can be expressed as a force per unit area between parallel plates, the net cohesive force will scale as

$Fc \sim \pi \Phi_{fp} d$. The dimensionless cohesive force, Fc^* (Equation (3. 19)), should be expressed as $Fc^* = \Phi d/(\rho_s-\rho)g$, where Φ is a function only of the chemical conditions.

3.9 Summary

This chapter considered the problem of how a bed of silt-sized particles, immersed in a flow of water, begins to move due to the fluid shear. For bed Reynolds numbers less than one, dimensional analysis reduces the non-cohesive problem to a relationship between two dimensionless parameters, q_s^*, a transport rate, and a shear stress τ^*. A small but finite value of q_s^* can be chosen to represent critical conditions, and to fix τ_c^*. The critical condition for initiation of motion is shown to correspond to a constant Shields Parameter (τ^* = constant) for $Re^* < 1$. In this case, the particle diameter is much smaller than the thickness of the viscous sublayer.

For fluid forces acting on a single particle, a scaling analysis shows that only the viscous forces are important, and fluid and grain inertia can be neglected. This allows analytical solutions for a sphere, which protruded into a linear shear flow, to be used to estimate the fluid drag force and torque acting on an individual sediment particle. Additionally, the instantaneous bed shear is parameterized as a stochastic process, while the contribution from acceleration terms is insignificant. This information was then combined with an idealized particle geometry to show that the dimensionless critical shear stress was constant for varying particle sizes and flow conditions. An estimate of the critical condition for non-cohesive materials is also provided.

This model is further extended to predict the sediment transport rate under a given mean shear by including a statistical distribution of particle elevation (and consequently

erodibility) on the bed. It is shown how a cohesive, inter-particle force will decrease the sediment transport rate, when the cohesion is quantified. The final section discusses the cohesive forces predicted by DLVO theory.

4 Experimental Apparatus and Methods

4.1 Recirculating Flumes

Experiments to measure the sediment transport rate utilized two tilting, recirculating flumes, 40 m and 12 m long respectively. The use of two flumes was required to allow for large Reynolds number flows (in the larger flume), as well as practical control over the water chemistry (in the smaller flume). In both cases, the sediment was contained in a test section inserted into a false bottom in the flume.

4.1.1 40-meter Flume

The first six series of experiments was carried out in the 40-meter precision tilting flume located in the W.M. Keck Hydraulics Laboratory. This flume has an open rectangular channel 40 m long, 110 cm wide, and 60 cm deep, constructed with a stainless-steel bottom and glass walls over the entire length. Details of the flume design are given by Vanoni et al. (1967). The downstream half of the flume is shown in Figure 4.1.

This flume is equipped with two variable-speed propeller pumps at the downstream end each discharging into a separate return pipe (20 cm/8 in. or 40 cm/16 in.), to provide an increased range of flow conditions. In all experiments, only one return pump was used, and the other was blocked with a plastic plug at the upstream hopper to prevent return flow through the unused pipe. To measure the total flow rate, each return pipe is equipped with a calibrated venturi meter (Keck Lab nos. Q-6 and Q-39) connected to an air-water manometer.

The return pipes connect to the bottom of an upward diverging hopper at the upstream end of the flume, which provides the transition to a rectangular, free surface flow that feeds the channel. At the channel entrance, two stainless steel mesh screens (120 mesh) and one half-inch thick poly-fiber air filter were mounted vertically across the entire flow. The resulting pressure drop across the screens was sufficient to damp out eddies from the inlet hopper and provided a smooth entry condition for the flow into the channel. The filter also collected fine particles formed from corrosion within the flume or deposited from the air and required replacement on a weekly basis.

Figure 4.1: Photograph of instrument carriage and 40-meter flume, looking downstream.

The instrument carriage (Figure 4.2) rolls the entire length of the flume along two adjustable, stainless steel rails mounted on top of the flume walls. For the purposes of

these experiments, the instrument position was driven in the X-Z plane (streamwise, cross-stream) by two stepper motors. In the streamwise direction, a rod with four threads per inch was installed on the carriage, and connected to a stepper motor with 200 steps per revolution. This arrangement allowed for the instrument to be positioned within a 60 cm range with a step size of 0.032 mm. In the cross-stream direction, an identical stepper motor was connected to the existing chain drive, providing a step resolution of 0.4 mm.

Within the flume, the test section of sediment was located 27.5 m downstream from the inlet hopper, and 12.5 m upstream from the outlet.

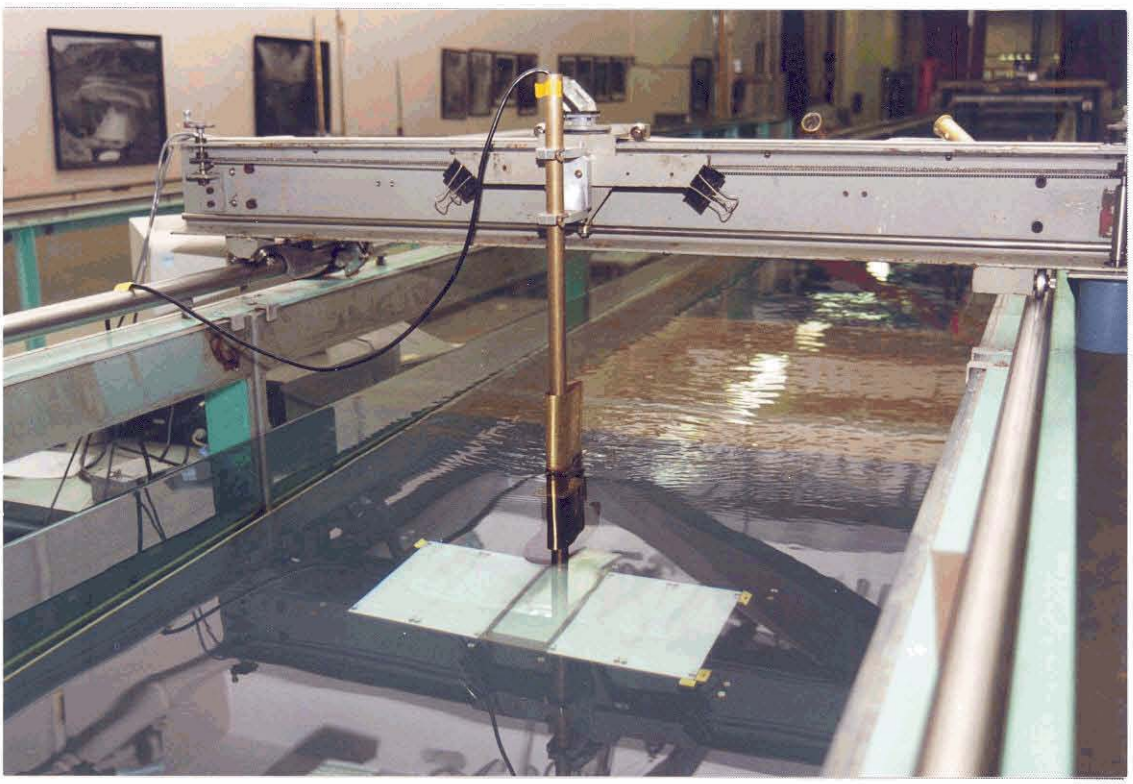

Figure 4.2: Photograph of instrument carriage on 40-meter flume.

A computer program controlled the position of the instrument carriage by indexing the stepping motors the appropriate number of steps. The program, operating on a personal computer with a digital I/O card, sent the indexing signal to the power supply for the appropriate stepper motor.

4.1.2 12-meter Flume

The second series of experiments was performed in the 12-meter recirculating flume facility, also located in the W.M. Keck Hydraulics Lab. This flume has a channel 12 m long, 26.5 cm wide, and 25.4 cm deep constructed of structural steel. The channel is painted with a chemically resistant, high solids epoxy paint, while the inlet and outlet hoppers and return pipe are galvanized. The side walls contain a 1.5 m section of Lucite located 8.5 m downstream of the inlet. The test section was located within this region, at a position 9 m downstream from the inlet (3 m from the outlet).

This flume is equipped with a variable-speed propeller pump at the downstream end of discharging into a return pipe (10.2 cm/4 in.), equipped with a calibrated venturi meter (Keck Lab no. Q-22). The venturi meter was connected to an air-water manometer, and used to measure the total flow rate.

The condition at the channel entrance was similar to the 40-meter flume, with two stainless steel mesh screens (120 mesh) and one half-inch thick poly-fiber air filter mounted vertically across the entire flow. The filter was replaced each time the water chemistry was adjusted (typically 4 to 6 experiments).

Variation in the water composition was only made practical by the reduced volume (600L) of this flume compared to the 40-meter flume (30,000 – 40,000 L). This volume

was sufficiently small that the flume could be filled with deionized water from Caltech's central supply and the composition adjusted by the addition of specific chemicals.

The instrument carriage on the 12-meter flume was similar to the 40-meter flume, except the instrument was fixed along the centerline of the flume. The carriage rolled along stainless steel rails, driven by a stepper motor (200 steps per revolution) connected to a 16-tooth spur gear. A mating 32-pitch rack was mounted on the inside edge of the rail. The computer interface used for experiments in the 40-meter flume was used to position the instrument carriage in the 12-meter flume, with the cross-stream interface unused. The instrument carriage can be seen in Figure 4.3.

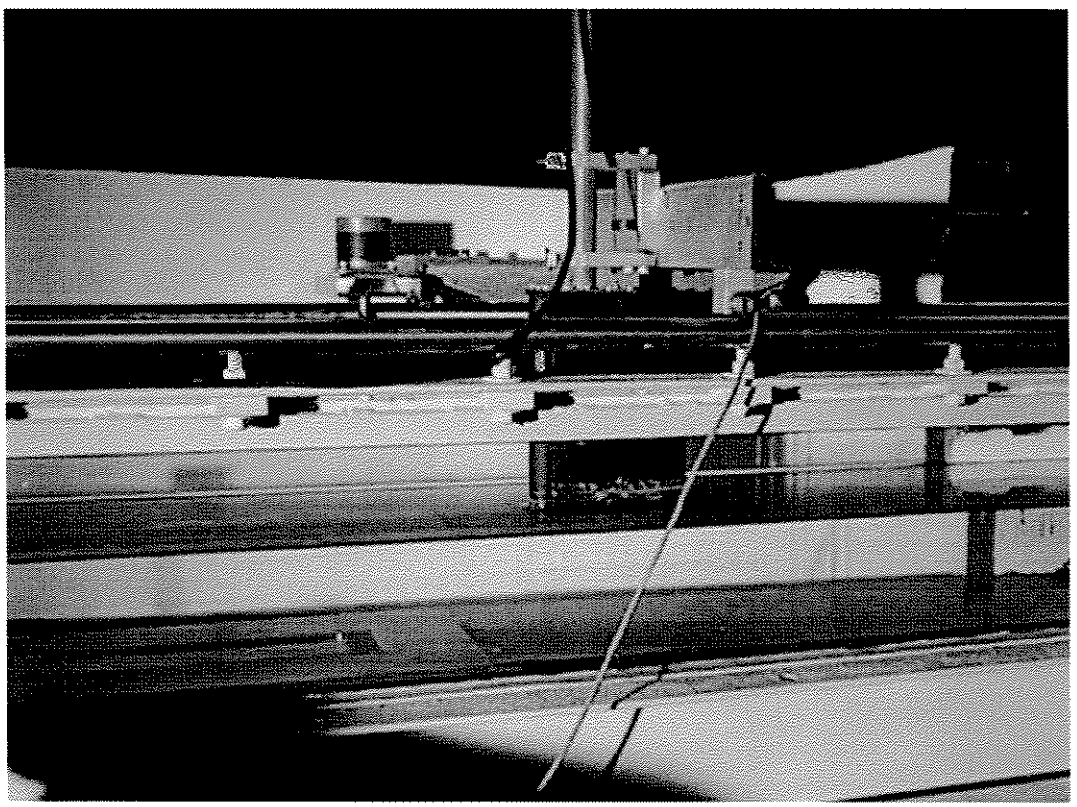

Figure 4.3: Photograph of instrument carriage on 12-meter flume. The laser displacement meter is mounted in the black foiled housing.

4.1.3 Test Section

The sediment was contained in a small tray, located on the flume centerline, within a false bottom as shown in Figure 4.4. The false bottom installed in each flume was identical, except for the width. The sediment was contained in a 316-stainless-steel tray, 450 mm long by 100 mm wide. The sediment occupied a recessed area measuring 400 mm long by 80 mm wide by 3 mm deep. The leading edge was sandblasted to provide a light grey reference surface for the laser displacement meter. This tray was bolted to two recessed surfaces in a ¼-inch stainless steel plate. This supporting plate contained adjustable set screws to account for irregularities in the flume bottom. The test section was leveled to within 0.1 mm. Upstream, a piece of ¼-inch PVC (poly-vinyl chloride) sheet extended 2m upstream, were it ended in a 1:10 ramp. Downstream, a ¼-inch PVC sheet extended for 50 cm, also ending in a 1:10 ramp. All of these components (except the test tray itself) were fastened to the flume bottom with a urethane adhesive/sealant (Bostik 920).

The first three series of experiments conducted in the 40-meter flume utilized a test tray with a recessed cavity measuring 200 mm long, 80 mm wide and 3 mm deep. For subsequent experiments, the sediment bed was lengthened to ensure that the sediment transport rate had reached an equilibrium value. The longer (400 mm) tray was used in all subsequent measurements.

4.2 Sediment Properties

All of the experiments (except Series E) utilized soda-lime glass beads obtained from Potters Industries Inc. (Valleyforge, PA) as a model sediment. The majority of these

particles were almost perfectly spherical (see Figure 4.6), with the occasional oblong or jagged shaped particle. The manufacturer's composition of the glass is reproduced in Table 4.1.

A. TOP VIEW

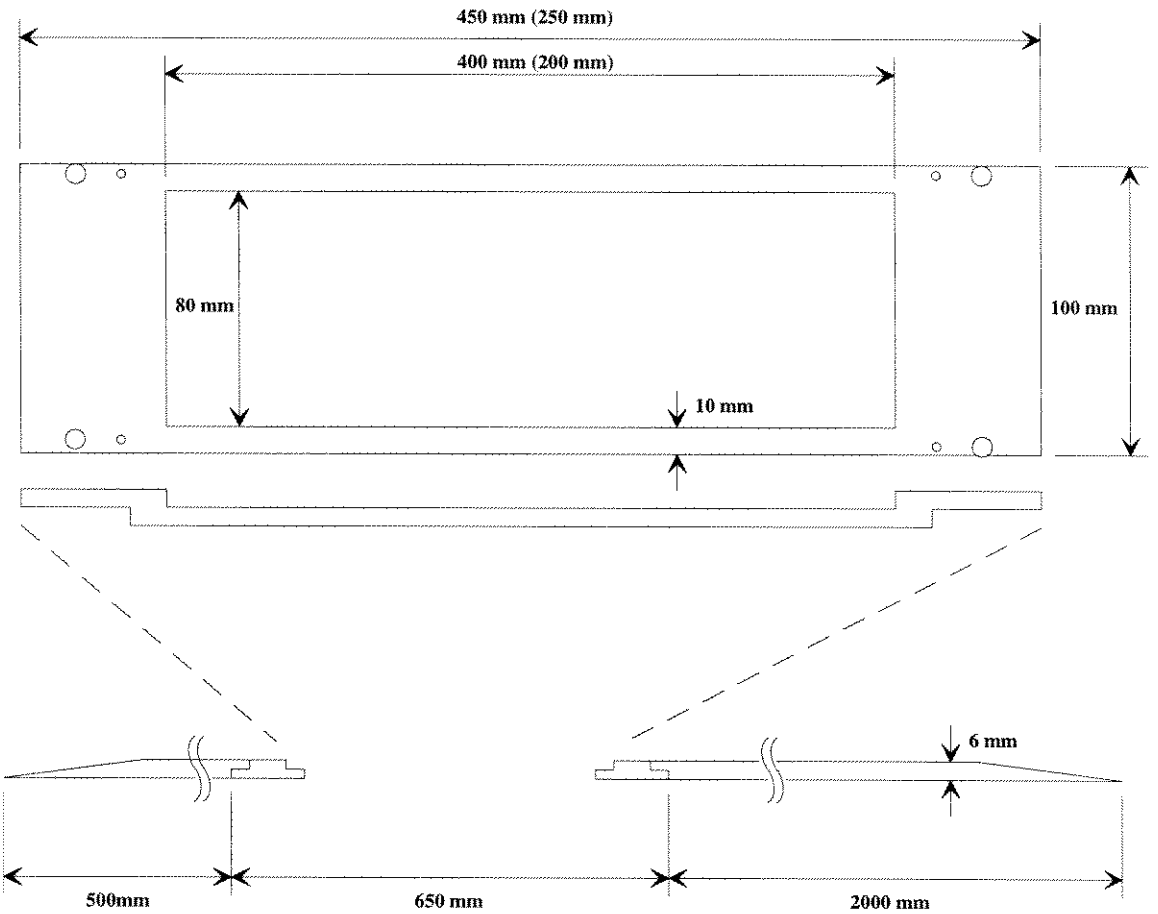

B. SIDE VIEW

Figure 4.4: Construction details of the false bottom and sediment test tray. Early experiments used a test tray with a 200 mm bed length.

Scanning electron micrographs of three of the sediments (d_g = 15 μm, 41 μm, 69 μm) used are shown in Figure 4.6 through Figure 4.8.

The glass beads supplied with smaller mean diameters had an unacceptably broad size distribution ($\sigma_g \sim 2$), and were separated into more uniform size classes before use. Two methods were employed to achieve this separation, sedimentation and fluidization.

For the sedimentation procedure, the glass beads were initially uniformly suspended in a glass jar, 40 cm tall by 20 cm in diameter. Typically the upper 80% was siphoned off after a prescribed period of quiescent settling. The jar was refilled with water, the remaining particles were resuspended, and the procedure was repeated until a sufficiently narrow size distribution was obtained.

The fluidization method used a column constructed of 4" Lucite pipe, with conical end caps (Figure 4.5). Flow entered the column from the bottom, fluidized the particles, and carried particles with settling velocities below the column velocity out the top. The bottom cone was filled with fine gravel (2-4 mm) overlain with sand (0.5 mm). This ensured that the flow emerged uniformly distributed across the column. The outflow was collected in a Lucite cylinder (30 cm in diameter), where the particles were allowed to settle; the overflow was collected, and pumped back (with a peristaltic pump) into the column. The peristaltic pump provided the constant, but low flow rate, and the recycling of the water allowed deionized water to be used with this method.

No modification of the size distribution was required for the particles of 69 μm or 41 μm mean diameter (Spheriglass 2530, Spheriglass 2900, and Spheriglass 3000) were used without any further size separations. Measurements of the size distributions (see Section 4.2.1) indicated that the Spheriglass 2900 and Spheriglass 3000 grade particles were identical, and had a mean diameter of 41 μm.

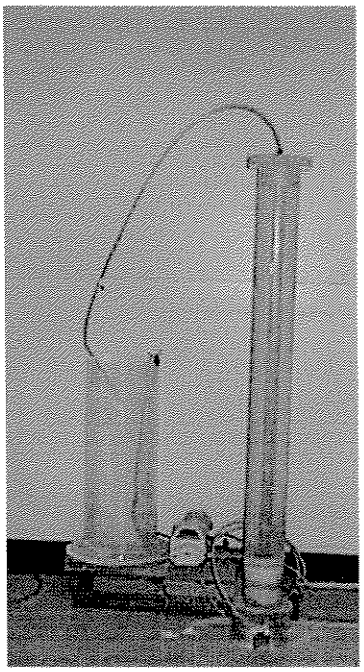

Figure 4.5: Picture of up-flow particle separation apparatus. Upwards flow in the column on the right would carry particles with smaller settling velocities out the top to be collected in the column on the left.

	% by mass	mole fraction (%)
SiO_2	72.5	73.1
Na_2O	13.7	14.2
CaO	9.8	9.2
MgO	3.3	2.2
Al_2O_3	0.4	0.7
FeO/Fe_2O_3	0.2	0.4
K_2O	0.1	0.2

Table 4.1: Composition of soda-lime glass beads (as reported by Potters Industries Inc.).

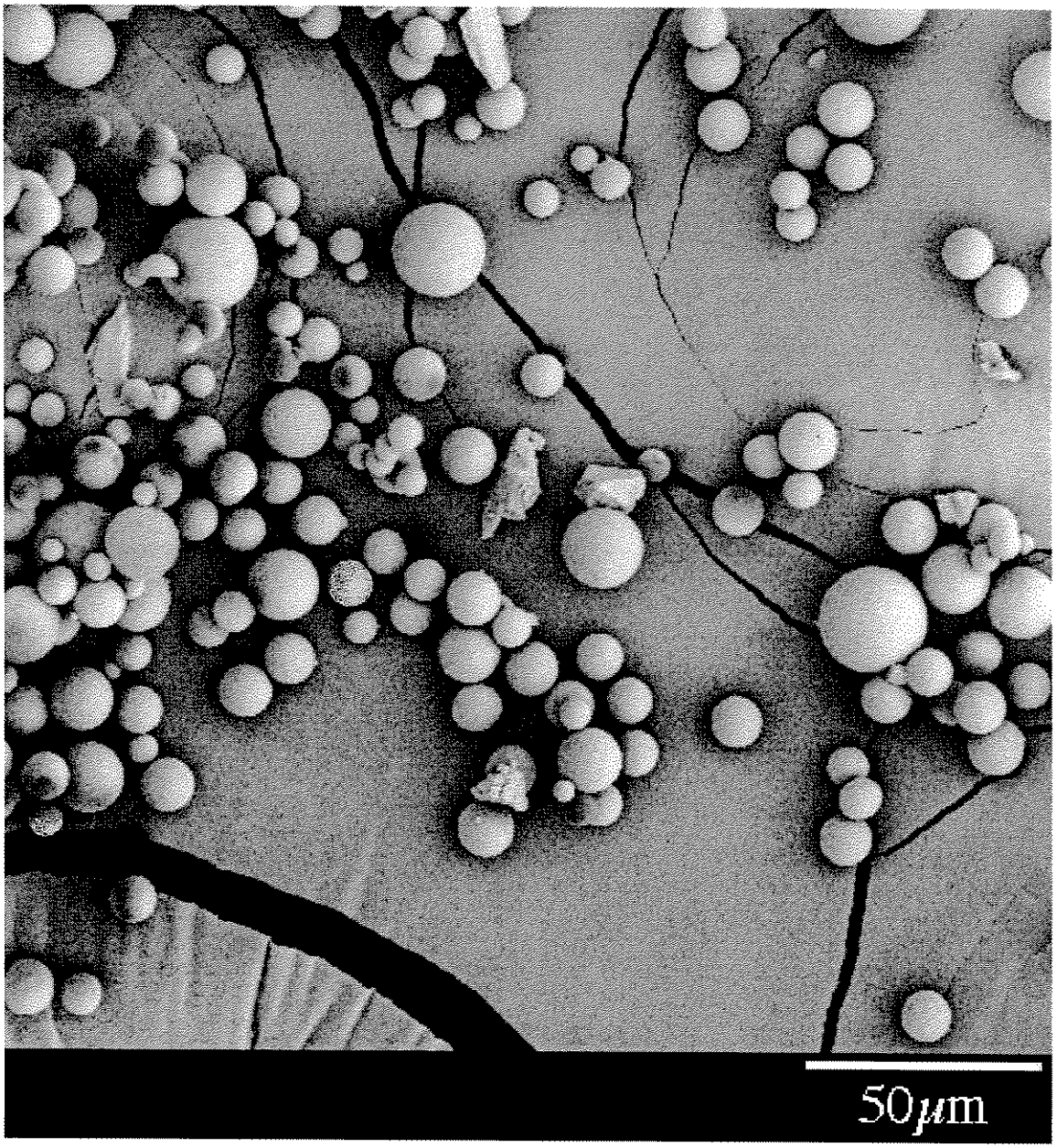

Figure 4.6: Photomicrograph of 15 μm glass beads. The particles were dried and mounted on a SEM sample stage, then coated with a gold film by sputtering.

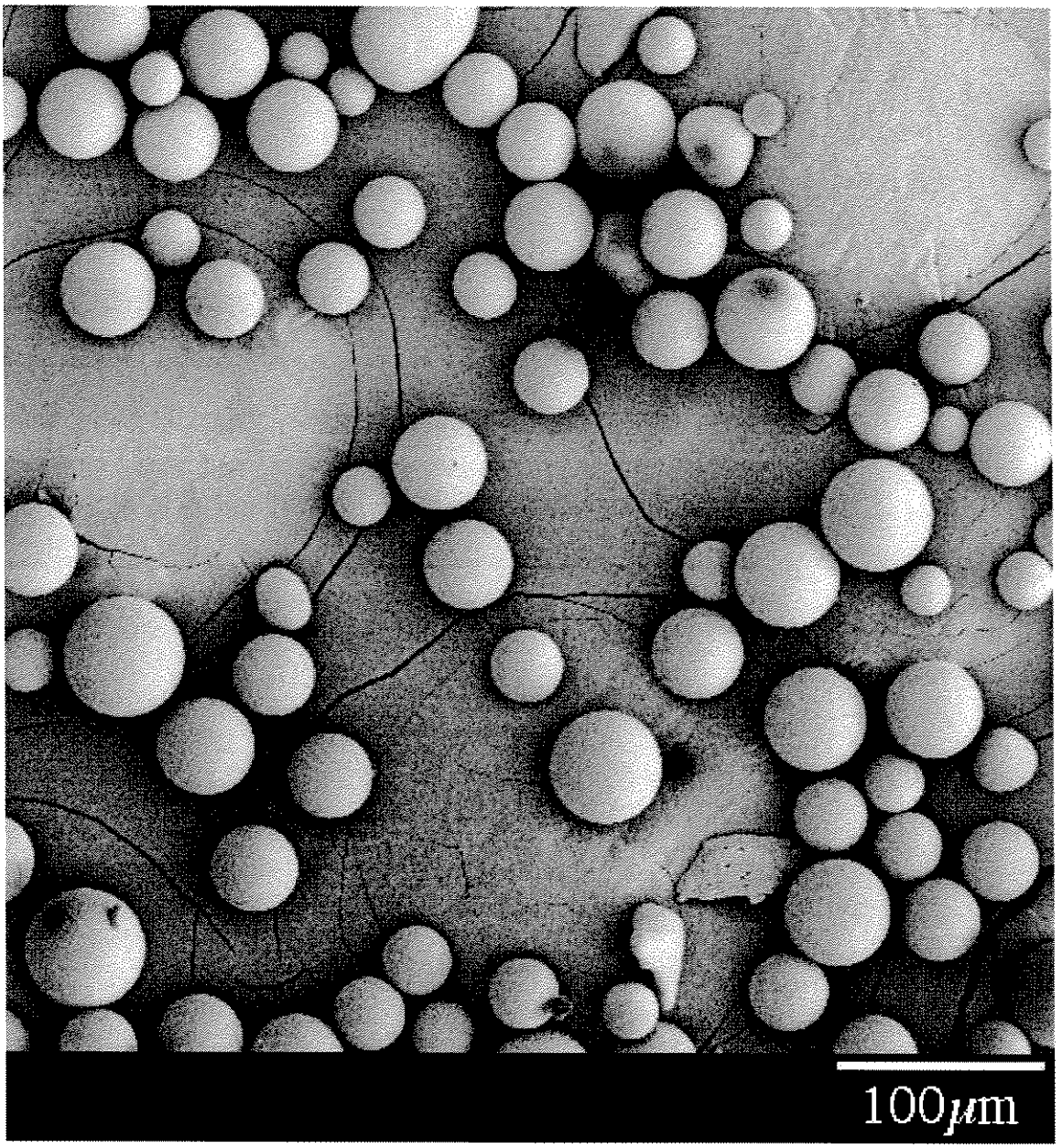

Figure 4.7: Photomicrograph of 41 μm glass beads. The particles were dried and mounted on a SEM sample stage, then coated with a gold film by sputtering.

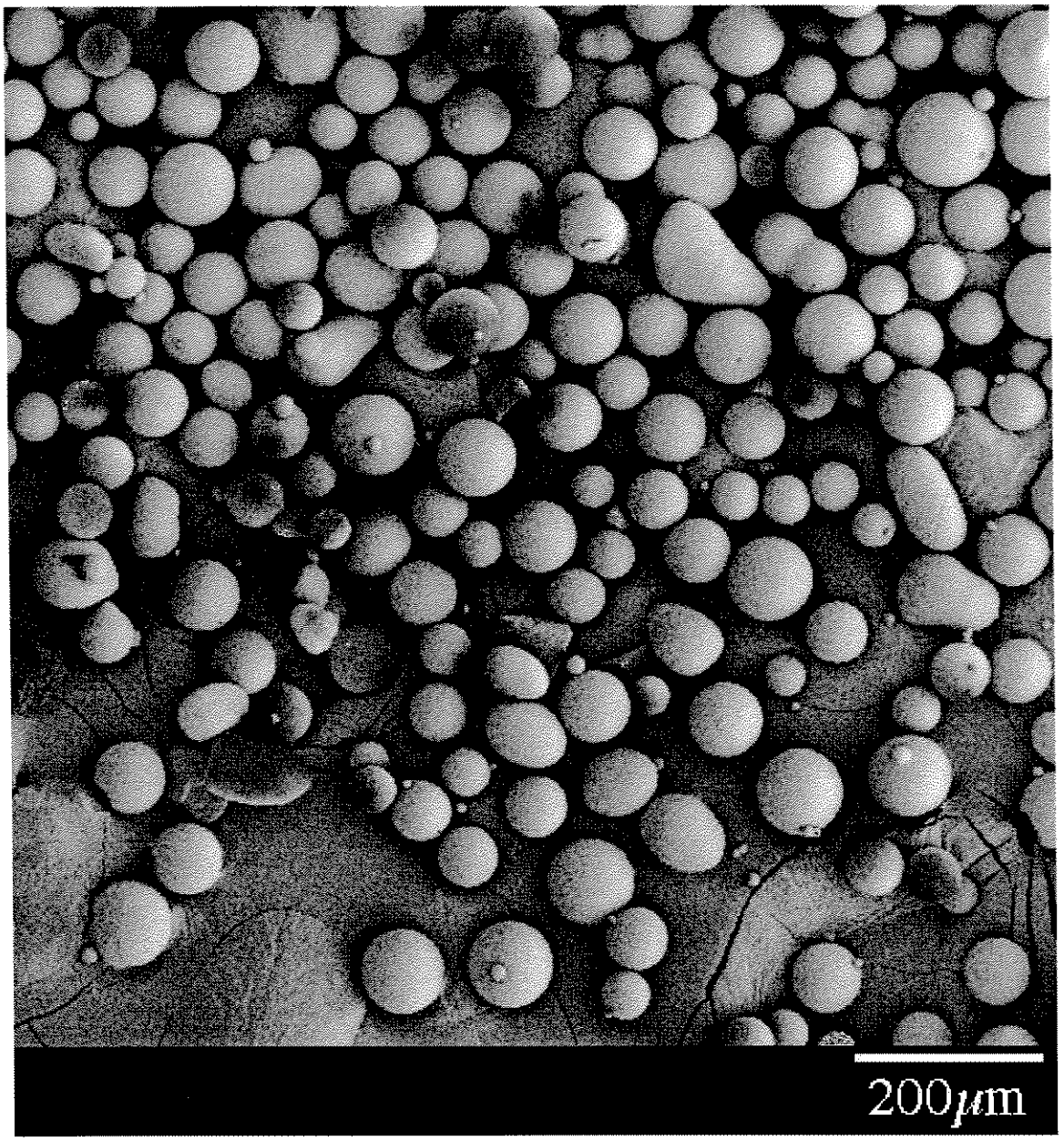

Figure 4.8: Photomicrograph of 69 μm glass beads. The particles were dried and mounted on a SEM sample stage, then coated with a gold film by sputtering.

4.2.1 Size Distributions

A model TA-II Coulter Counter (Coulter Electronics, Inc., Hialeah, FL) was used to measure the size distribution of the glass beads. The 140 μm and 50 μm apertures were used, as appropriate. The geometric mean diameters of the particles were: 15 μm,

26.5 μm, 41 μm, and 69 μm, with an approximate log-normal distribution and a geometric standard deviation of 1.28-1.3. The cumulative size distributions and best fits are shown in Figure 4.9.

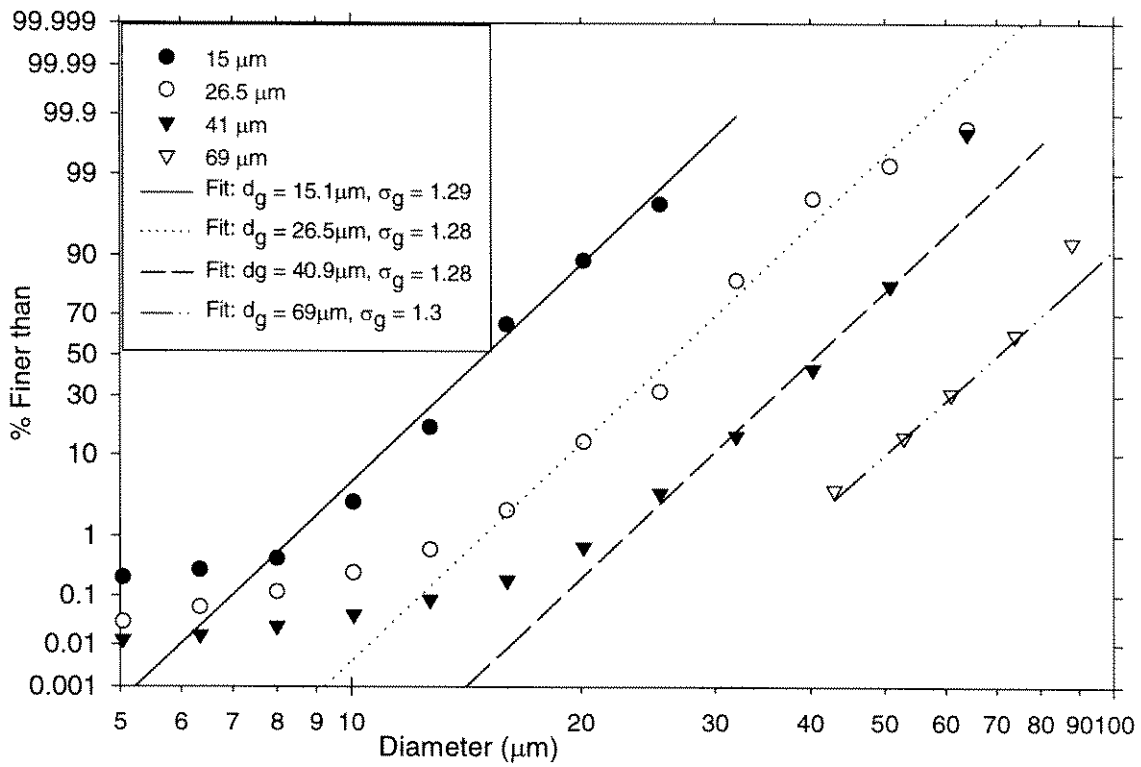

Figure 4.9: Size distribution of glass beads. The fitted log-normal distributions correspond to: d_g = 15.1 μm, σ_g = 1.29; d_g = 26.5 μm, σ_g = 1.28; d_g = 40.9 μm, σ_g = 1.28; d_g = 69 μm, σ_g = 1.3.

4.2.2 Surface Properties

Electrophoresis is the steady translation of charged colloidal particles under the influence of an external electric field; the electrokinetic potential (zeta potential, ζ) is the potential associated with this motion. It is assumed that a shear layer separates two portions of the double layer: one adhered to the particle, the other free to move. The

potential at this shearing layer is the electrokinetic potential; it is often assumed to be identical to the potential across the diffuse portion of the double layer (Ψ_d).

The pH at which the number of positive and negative surface sites are equal and the surface is uncharged is referred to as the pH of the point of zero charge (pH_{pzc}). The surface potential is zero at the pH_{pzc}, thus the particles do not move under an applied electric field.

The electrophoretic mobility (velocity per unit of electric field) was measured for the glass microspheres with a Rank Brothers Mark II Microelectrophoresis instrument utilizing a rectangular cell (1 mm thick by 10 mm high). Colloidal particles were obtained from the original microspheres by grinding them with mortar and pedestal, followed by 30 minutes of sonication. Twenty measurements of the particle velocity were made for each sample, ten in each direction. The zeta potential was computed from the measured particle mobility (m_e) by the Smoluchowski formula (Stumm & Morgan, 1996):

$$m_e = \frac{\varepsilon \varepsilon_o \zeta}{\mu} \qquad (4.1)$$

where ε is the relative dielectric permittivity, ε_o the permittivity in vacuum, and μ the viscosity of the solution.

The particles were found to have zero mobility (no net surface charge) at a pH of ~2.0 (pH_{pzc}), similar to reported values of SiO_2. Figure 4.10 shows the calculated zeta potential as a function of salt concentration (NaCl) and pH. Pasadena tap water has an ionic strength of about 15 mM, and a conductance of 850-900 μmho/cm. The larger zeta potential at lower ionic strengths is due to a greater portion of the diffuse double layer residing outside the shear plane.

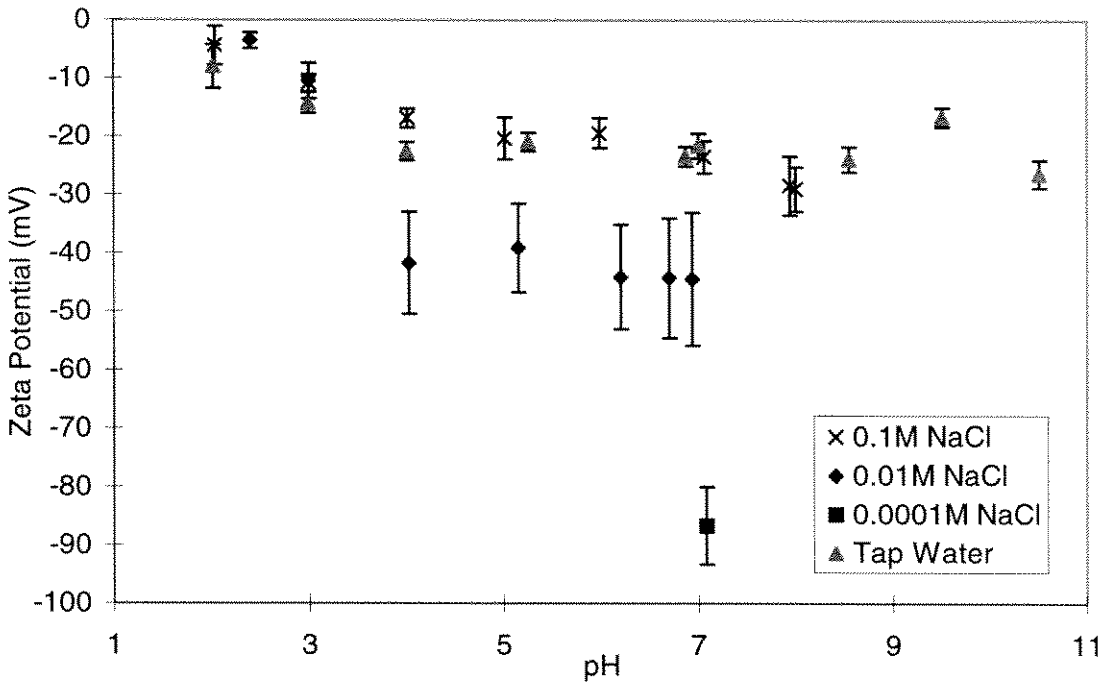

Figure 4.10: Zeta potential of glass beads as determined by electrophoresis for tap water (I ~ 15 mM) and three concentrations of NaCl solution.

4.3 Sediment Preparation

As obtained, the glass beads were mixed with iron particles, likely a by-product of their manufacturing process. The iron particles were assumed to be magnetite, being both magnetic and black in appearance. In order to remove this unwanted iron, the following washing process was developed.

First, a strong magnet was used to remove the magnetite particles, by allowing a suspended solution of particles to settle across the magnetic field. This was repeated until only a few particles were attracted to the magnet.

Second, the particles were suspended in 1.0N HCl and stirred overnight with a propeller-type stirrer. After settling the particles, the supernatant was removed, and collected. The amount of iron removed was estimated from comparison of the

supernatant's UV absorbance with a calibration curve (Figure 4.11). The absorbance at 335 nm corresponds to the $FeCl_2^+$ complex (Thompson and Tahir, 1991). The particles were then rinsed with deionized water until the pH no longer changed (usually 5 to 7 rinses).

Third, the particles were washed with hydrogen peroxide to remove any organic contaminants. The procedure, adapted from Black (1966), involved heating a suspension of particles in 10% H_2O_2 to 70°C for 15 minutes. Once cooled, the liquid was drained and the particles rinsed (usually twice) with deionized water.

The final step was to remove iron by reducing it, following the procedure in Black (1966). A solution comprised of 400 mL 0.3M sodium citrate and 50 mL 1.0M sodium bicarbonate were added to the particles and heated to 70°C. To this solution, 10 g sodium dithionate ($Na_2S_2O_4$) was added, stirred for 15minutes, and allowed to cool.

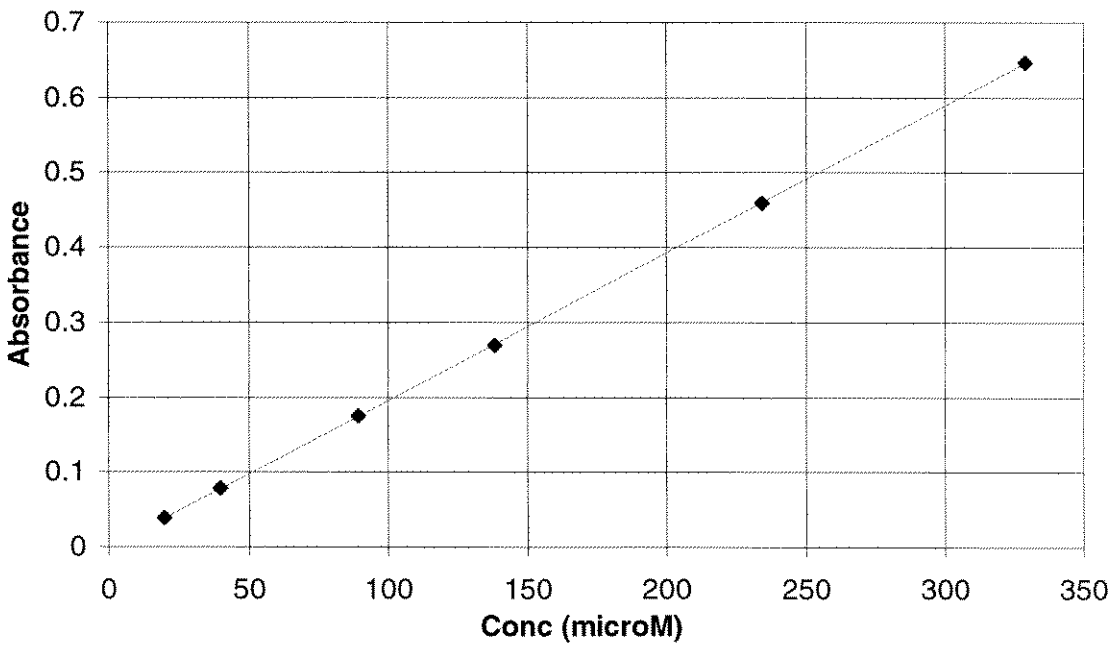

Figure 4.11: Calibration curve for UV adsorption at 335 nm of Fe in 1N HCl solution. Adsorption corresponds to $FeCl_2^+$.

Upon cooling, the supernatant was discarded, and the particles rinsed with deionized water until the pH no longer changed (5 to 7 rinses).

Step two was then repeated. If the amount of iron dissolved in the HCl was less than ~15 μM, the particles were considered clean. Otherwise, steps two through four were repeated until this condition was met.

It was found that aging (on a time scale of several weeks to months) would change the surface chemistry of the glass beads and reduce the observed transport rates. It was found that the transport rate matched that of the freshly prepared particles if the particles were rinsed in 1.0N NaOH (overnight), followed by 1.0N HCl (overnight), and then rinsed with deionized water until the pH stabilized. This procedure was used on all particles that had been prepared more than two months before their use.

4.4 Laser Displacement Meter

The sediment transport rate was computed from the change in the sediment bed's surface elevation in time. This was accomplished by mounting a LB-081 Laser Displacement Meter (Keyence Corp.) to the flume's instrument carriage. This displacement meter measures distance by triangulating the maximum intensity of the diffuse reflection from a laser beam incident on the surface. Although the instrument has a stated accuracy of < 2μm on a white surface, an accuracy of < 10 μm was observed on the sediment bed. The instrument was mounted in a foiled, waterproof housing, with a glass bottom (see Figure 4.3), allowing submersion in the ambient flow. A position approximately 10 cm above the test bed was required for optimal performance and range of the displacement meter.

The LB-081 meter was connected to a LB-1101 processor, which produced an analog output signal with a full-scale range of -5 to 5 volts. This voltage was measured, accurate to 0.01mV, with a H-P 3478A Multimeter and recorded on a personal computer via a GPIB bus interface.

The response of the laser displacement instrument proved to be linear throughout its operating range. A typical calibration curve using a white target attached to a point gauge vernier (+/- 0.1 mm) is shown in Figure 4.12. This was required to calibrate the instrument's sensitivity (V/mm).

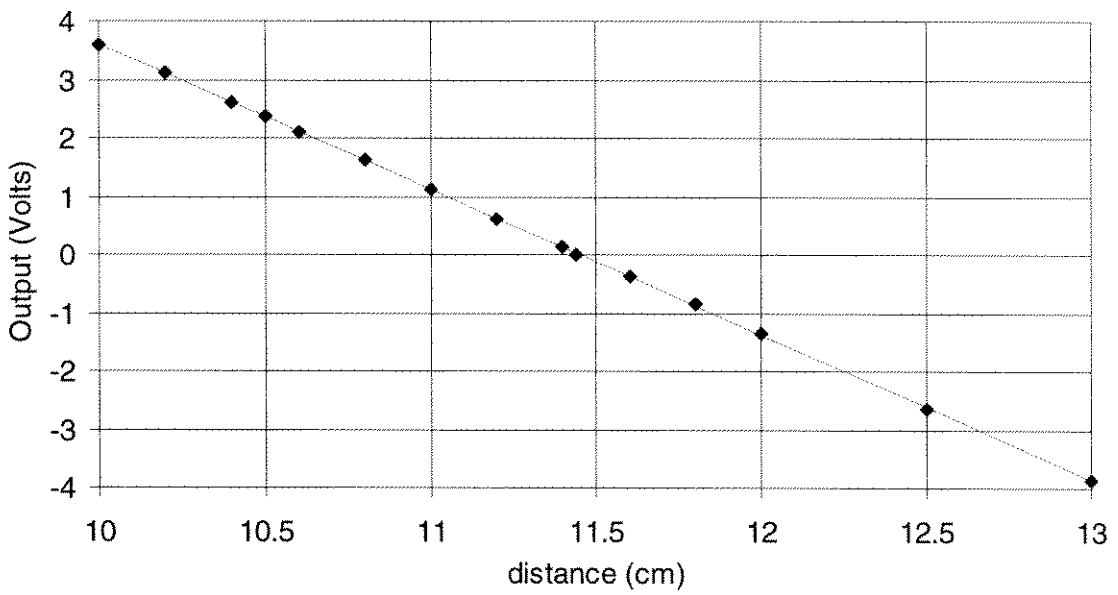

Figure 4.12: Calibration curve of laser displacement meter (LB-081/1101, Keyence Corp.).

4.5 Shear Stress Measurements

The shear stress over the sediment test section was calculated from the mean flow depth (D) and the total discharge (Q) as measured by the venturi meter. The mean velocity (U) is related to the shear stress (τ) by the friction factor (f) as:

$$\tau = \rho u^{*2} \tag{4.2}$$

$$\frac{u^*}{U} = \sqrt{\frac{f}{8}} \tag{4.3}$$

A smooth boundary layer was assumed, and the friction factor was determined from the Blasius equation with the Reynolds number based on the hydraulic diameter:

$$f = 0.316\,\mathrm{Re}_{Dh}^{-1/4} \tag{4.4}$$

$$\mathrm{Re}_{Dh} = \frac{U \cdot 4R}{\nu}$$

$$R = \frac{BD}{B + 2D}$$

where f is the Darcy-Weisbach friction factor, B is the channel width, D the flow depth, R the hydraulic radius, and Re_{Dh} the Reynolds number based on the hydraulic diameter (four times the hydraulic radius) and the mean flow velocity, U. The use of the hydraulic radius, instead of the flow depth, accounts for friction along the side-walls. No additional correction was made for the side walls.

A channel (or pipe) is considered 'smooth' if (White, 1986):

$$\frac{k_s u^*}{\nu} < \approx 5 \tag{4.5}$$

$$\mathrm{Re}^* = \frac{u^* d}{\nu} < 2$$

with the roughness elements height (k_s) usually taken as 2.5d. Substitution yields the criteria for a hydraulically smooth bed as $Re^* < 2$. This was the case in all experiments conducted in this study.

The shear stresses required to mobilize the fine sediments used in this investigation correspond to a uniform flow with a free surface slope of 10^{-5} to 10^{-4}, which was too small to measure accurately. To verify that the shear stresses calculated from the smooth boundary friction factor were accurate, a two-component Laser Doppler Velocimeter (Model 5980, TSI Inc. St. Paul, MN) was used to measure the velocity profile and Reynolds stress profile in the 12-meter flume. Agreement between the two values was good, as shown in Table 4.2. The total shear stress was obtained from the LDV measurements by extrapolating the linear portion of the Reynolds stress to the channel bottom (y = 0). The Reynolds shear stress profile for uniform flow in an infinitely wide channel is linear from the free surface to just above the bottom (y/D < 0.05), where viscous shear becomes important.

Mean Velocity [cm/s]	Depth [cm]	Computed u* from Equation (4.3) [mm/s]	u* from Reynolds Stress [mm/s]	% Difference
14.9	9.9	7.97	7.95	0.25
21.2	10.0	10.9	10.3	5.50

Table 4.2: Comparison of predicted friction velocity with that calculated from Reynolds stress measurements.

The measured Reynolds stresses (Figure 4.13) are linear only in the lower half ($y/D < 0.5$) of the flow depth. This discrepancy is taken to be the result of boundary friction from the sidewalls, since the width to depth ratio of the flow was about 2.65:1. Measurements at a width-to-depth ratio of 6:1 provided results that were closer in line with theory, and previous work in this flume at similar width:depth ratios (Lyn, 1986). The corresponding velocity profiles are shown in Figure 4.14. The velocity profiles were fit with a logarithmic velocity profile with a wake function:

$$\frac{u_{max} - u}{u^*} = -\frac{1}{\kappa}\ln\left(\frac{y}{y_{max}}\right) + \frac{2W_o}{\kappa}\cos^2\left(\frac{\pi}{2}\frac{y}{y_{max}}\right) \qquad (4.6)$$

u* was obtained from the Reynolds stress measurements, κ was taken as 0.4, y_{max}

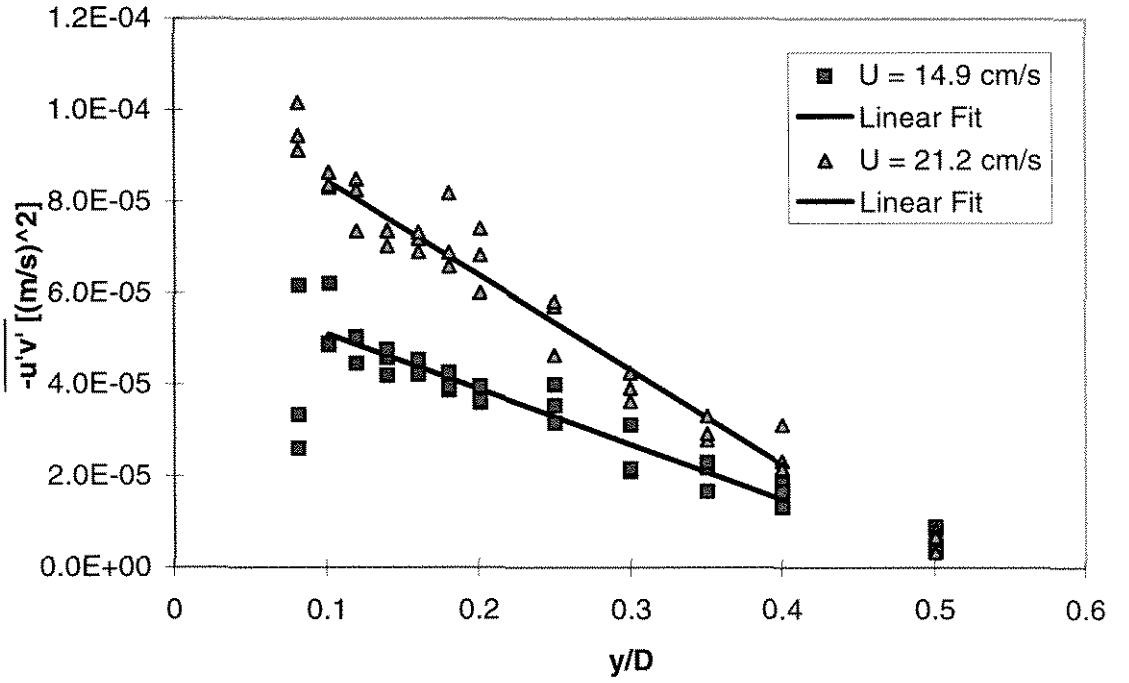

Figure 4.13: Measured Reynolds stresses for two flow rates in the 12-meter flume. Each point is a five minute average.

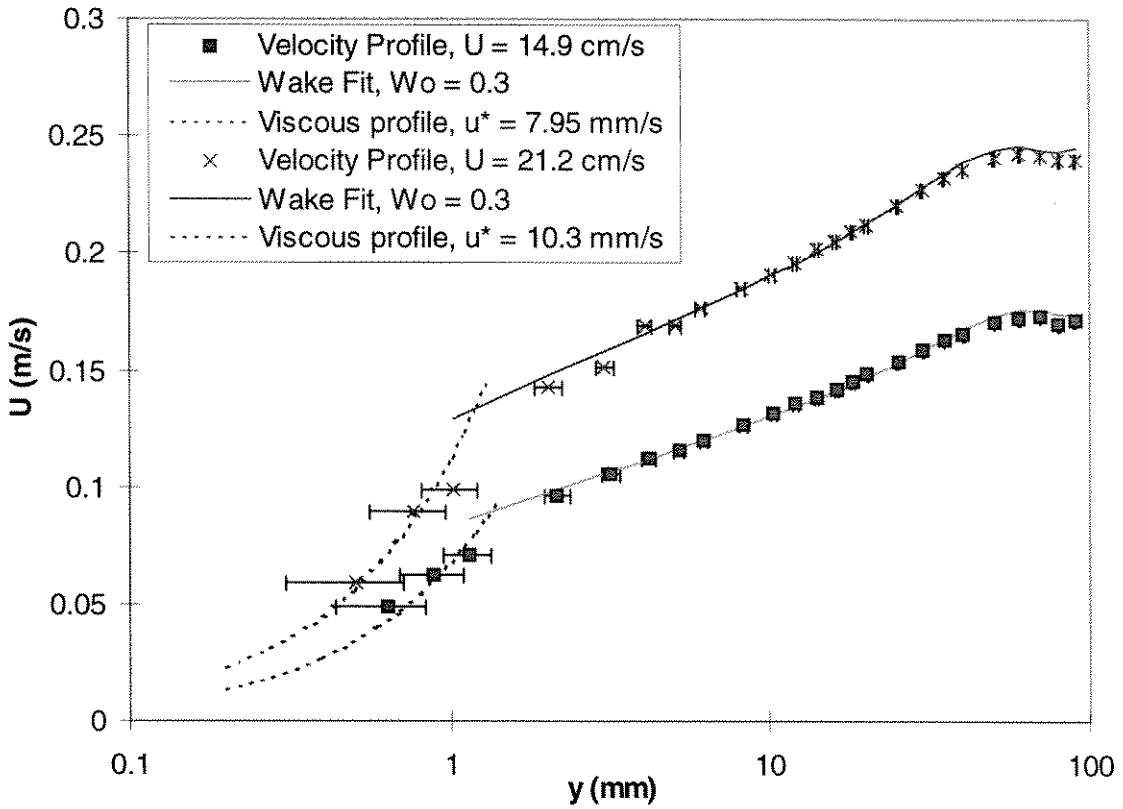

Figure 4.14: Measured velocity profiles. Curve fits are from equation (4.6) for U= 21.2 cm/s ($u^* = 10.26$ mm/s, $y_{max} = 45$ mm, $U_{max} = 24.2$ cm/s, Wo = 0.3, $\kappa = 0.4$) and U=14.9 cm/s ($u^* = 7.95$ mm/s, $y_{max} = 50$ mm, $U_{max} = 17.3$ cm/s, Wo = 0.3, $\kappa = 0.4$).

taken as the intercept of the linear fit to the Reynolds stress and the $\overline{u'v'} = 0$ axis. The wake parameter (W_o) was adjusted to obtain the best fit. A value of 0.3 was obtained for both flow rates. The predicted velocity profile ($u(y) = yu^{*2}/\nu$) within the viscous sublayer is also shown.

4.6 Experimental Protocol

The experimental protocol for each experiment is as follows. The desired water depth and chemistry in the flume was set. In the 12-meter flume, deionized water from

the Caltech water supply was used to fill the flume, to which a measured amount of salt was added. The resulting electrical conductivity and pH of the flume water were measured. For the 40-meter flume, Pasadena tap water was used, and no attempts were made to vary the chemistry. It was found that a delay of 24 hours or more was beneficial to allow the excess dissolved air to out-gas and prevent air bubbles from forming on the glass interface under the laser displacement meter.

A rectangular Lucite column was then bolted to the test plate utilizing the four corner mounting holes. Figure 4.15 shows the column mounted to the 40 cm test tray in the 40-meter flume. The Lucite column has a foam gasket around the mating edge to form a tight seal, and prevent the sediment from escaping.

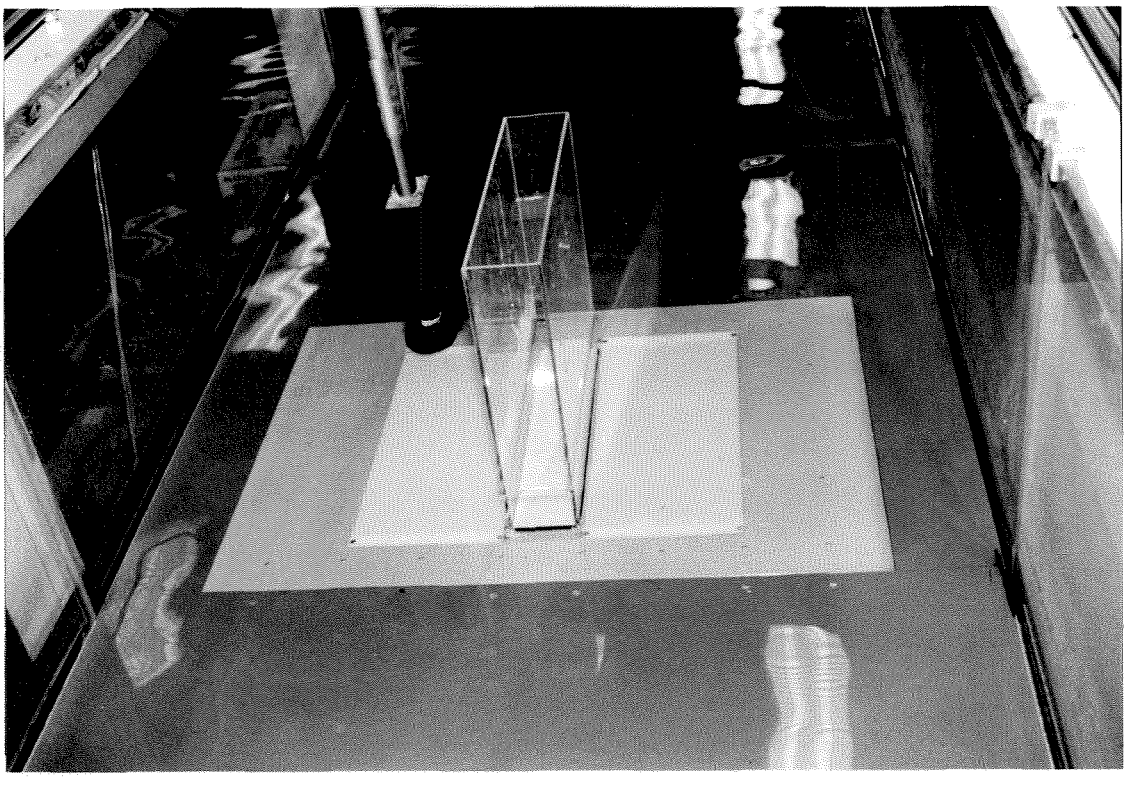

Figure 4.15: Lucite column used to obtain a flat bed by settling the glass beads into the test tray. Shown here on the 40 cm test tray in the 40-meter flume.

To prepare the test bed, the required volume of clean glass beads was measured out in a graduated cylinder to match the volume of the recessed cavity, and added to the water column over the test patch. Next, a propeller–type stirrer was used to uniformly suspend the material in the water column. The suspension was then left to settle quiescently, typically for 6 – 12 hours to ensure a consolidated bed.

After this period of time, the Lucite column was carefully removed without disturbing the bed, and the LB laser meter was scanned over the test patch once, to ensure that the test patch was smooth and relatively flush with the edges of the tray. If the elevation of the sediment bed was too high or low, the column was replaced and more material was added (removed); the bed re-mixed and allowed to settle again.

The desired data acquisition sequence was then entered into the computer. This included the number of iterations to measure the bed surface, the interval between measurements, and the grid pattern and spacing to use. Generally, scans of the 40-cm test plate were made every 10 minutes for 2 to 8 hours, depending on the expected transport rate. The grid pattern used included about 10 measuring points on the upstream lip of the test plate. These values provided a reference to correct for any instrumental drift over the duration of the experiment.

The slope of the flume was set to approximate that required for uniform flow at the desired flow rate. However, since the slope required was less than the unevenness in the flume bottom, the flume was left at an approximately level slope.

The flow in the flume was then gradually (over several minutes) ramped up to the desired flow rate, and the data acquisition was started. The computer software created a

file of the measured bed elevation at each location (X, Z) for each time iteration. This file was processed after the experiment was concluded.

The experiment was concluded when either the bedform troughs had scoured the depth of the test section (3 mm), or the desired time had elapsed. Since the majority of sediment transport occurred as bed load, this material was located immediately downstream of the test section after each experiment. Instead of measuring out new sediment for each trial, the material was gently scraped back into the test tray, resettled, and the procedure was repeated.

During the experiments, water was allowed to drip into the flume at the rate required to counteract evaporation and leakage (from pump bearing). In the 40-meter flume, a constant water level was achieved by means of an overflow tube attached to the reservoir at the downstream end. In the 12-meter flume, a constant water level was maintained by adjusting the rate at which water dripped into flume.

The experimental conditions, results and detailed analysis are presented in the next two chapters.

5 Results

5.1 Experimental Overview

Experiments were conducted in two recirculating laboratory flumes to investigate how flow parameters and water chemistry affect the sediment transport rate of silt-sized particles. Each experiment measured the sediment transport rate under constant flow parameters and water chemistry. This chapter presents the experimental conditions, computational procedure, and results. Further discussion and interpretation of the results are given in Chapter 6.

The experimental results are presented by series, in chronological order. The test plate length, particle diameter, and water composition remained constant throughout each series. Experiments within each series differ by the fluid shear stress (flow rate, flow depth). The first six series of experiments were conducted in the 40-meter flume to ascertain the suitability of the dimensionless shear stress (τ^*) and dimensionless transport rate (q_s^*) parameters to collapse the results. The effect of turbulence (via Reynolds number) and the length of the test section were investigated. In the 12-meter flume, the first three series of experiments were undertaken in tap water to verify similar behaviour as observed in the 40-m flume. The remaining experiments used specific electrolytes and deionized water to vary the solution chemistry, which changed the particle-particle cohesion.

In all experiments the mean bed shear stress ($\tau = \rho u^{*2}$) was computed with equation (5.1) from the calculated friction factor (f, equation 4.4), and mean flow rate

(U). The flume bottom and side-walls were hydraulically smooth, so no additional correction to the shear stress was made for the side-walls.

$$\frac{u^*}{U} = \sqrt{\frac{f}{8}} \tag{5.1}$$

Except where noted, two-dimensional bedforms (ripples) developed from the initially flat sediment bed, increasing in amplitude and wavelength as time progressed. The ripples grew faster with increasing sediment transport rate. These ripples were approximately straight across the entire width of the sediment bed, with some curvature at the edges of the test bed. Some experiments produced ripples that merged and branched, but moved primarily downstream.

Each experiment produced a data file containing a time series of the sediment bed elevation profiles. From this data, the mean transport rate, the local transport rate, $q_s(x)$, and the mean decrease in bed elevation were computed with the following computational procedure.

The measured sediment bed elevation, $\eta(x, t)$, is integrated over the length (0 to L) of the test bed, for each time step, to give the volume per unit width (b):

$$\frac{Volume(t)}{width} = \int_0^L \eta(x,t)\partial x \approx \sum_{i=0}^{N} \eta(x_i,t)\Delta x \tag{5.2}$$

where N measurements were made over the sediment bed, spaced Δx apart, and the integration is approximated by a numerical summation of the measurements.
The correction for instrumental drift is computed by averaging the N_C measurements made on the frame of the test tray upstream of the sediment bed ($-x_1$ to 0):

$$Correction(t) = \frac{1}{x_1}\int_{-x_1}^{0}\eta(x,t)\partial x \approx \frac{1}{N_C}\sum_{j=0}^{N_C}\eta(x_j,t)\Delta x \tag{5.3}$$

Subtracting this correction from Equation (5.2), the volume/width is obtained, to within an arbitrary constant. The corrected bed volume is take to be zero at t=0, so the sediment volume transported off the test bed is given by:

$$\begin{aligned}\frac{V(t)}{b} &= \int_0^L \eta(x,0)\partial x - \int_0^L \eta(x,t)\partial x - \frac{L}{x_1}\left(\int_{-x_1}^{0}\eta(x,0)\partial x - \int_{-x_1}^{0}\eta(x,t)\partial x\right) \\ &\approx \sum_{i=0}^{N}\eta(x_i,0)\Delta x - \sum_{i=0}^{N}\eta(x_i,t)\Delta x - \frac{N}{N_C}\left(\sum_{j=0}^{N_C}\eta(x_j,0)\Delta x - \sum_{j=0}^{N_C}\eta(x_j,t)\Delta x\right)\end{aligned} \tag{5.4}$$

This is converted into a mean bed elevation ($\bar{\eta}$) by division by the bed length (L):

$$\bar{\eta}(t) = \frac{V(t)}{bL} \tag{5.5}$$

The rate of decrease of the mean bed elevation ($d\bar{\eta}/dt$), or the mean erosion rate ($\dot{E}$), may be re-expressed as the transport rate off the test section (x=L):

$$q_s(L) = L\frac{dE}{dt} \tag{5.6}$$

Both the mean erosion rate ($\dot{E}$) and the transport rate (5.6) are computed from the change in volume of the sediment bed and are thus independent of the nature of sediment transport (bedload, suspended load). If the sediment transport occurs primarily as bed load, the transport rate will reach a constant value, independent of downstream position. In this case, the mean erosion rate would decrease if viewed over a longer sediment bed. However, if material was entrained into the mean flow and carried off the sediment bed, the erosion rate would remain constant, while the transport rate would increase linearly with distance. The measured bed profiles also allow the transport rate to be computed at each location (x) along the sediment bed:

$$q_s(x,t) = \int_0^x \frac{d}{dt}\eta(\xi,t)d\xi - \frac{x}{x_1}\int_{-x_1}^{0} \frac{d}{dt}\eta(\xi,t)d\xi \tag{5.7}$$

$$\approx \sum_{i=0}^{m} \frac{1}{\Delta t}\left[\eta(i,t-\Delta t) - \eta(i,t)\right]\Delta x$$

$$-\frac{x}{x_1}\sum_{j=0}^{N_c}\left(\eta(j,t-\Delta t) - \eta(j,t)\Delta x\right)$$

where $x = m \cdot \Delta x$

where ξ is an integration variable. Evaluated at x = L, this is equivalent to equation (5.6). The relation of the sediment transport rate (q_s) to the downstream position (x) is used to determine if the sediment is being suspended into the mean flow. The formation of ripples and the presence of material deposited immediately downstream of the sediment bed provide additional evidence of bedload transport.

5.2 Experimental Results

Tables 5.1 through 5.6 contain the basic hydraulic data and measured sediment flux for all the experiments. The experiments are grouped by the flume used, the length of sediment bed used, and by the mean sediment grain size. A description of the experimental conditions and results is contained in the sections following these tables. A description of each variable listed in the tables is provided below.

Expt. No.: experiment number. The letter indicates the experimental series (constant particle size, preparation, and water chemistry). The number indicates experiments within each series, in chronological order.

***d**: mean diameter* (d, d_g), the geometric mean diameter of the sediment, as determined from the Coulter Counter, Model TA-II (see Section 4.X). The symbols d_g and d both refer to the geometric mean diameter in this work. (um) indicates microns (μm), 10^{-6} meters.

***Q**: flow rate*, the recirculation flow rate as measured by Venturi meter/manometer combination (see Section 4.2).

***D**: water depth*, the elevation difference between free surface and the upstream edge of the sediment tray.

***Temp.**: water temperature*, the temperature of the flume water, in degrees Centigrade.

ν: kinematic viscosity of the flume water; inferred from the measured water temperature.

***U**: mean velocity*, the average stream velocity over the cross section of the channel. U = Q/BD, where B is the flume width, 110 cm in 40-meter flume, and 26.5 cm in 12-meter flume.

***Re**: the mean flow Reynolds number based on the hydraulic diameter (four times the hydraulic radius).* $\mathrm{Re}_{Dh} = \dfrac{U 4\left(\dfrac{BH}{B+H}\right)}{\nu}$

***f**: Darcy-Weisbach friction factor.* $f = 8(u^*/U)^2$.

u^*: shear velocity, $u^* = \sqrt{\dfrac{\tau}{\rho}}$

Re^*: bed Reynolds number, $\mathrm{Re}^* = \dfrac{u^* d_g}{\nu}$

τ^*: dimensionless shear stress (τ^*), also Shields' parameter. $\tau^* = \frac{\tau}{(\rho_s - \rho) g d_g}$

where ρ_s is the sediment density (2500 kg/m^3), ρ the fluid density (998 kg/m^3), and g, gravity.

E: erosion rate ($\dot{E}$), the rate of decrease of the mean sediment bed elevation ($d\eta/dt$).

q_s: transport rate, the rate of material moving downstream from the sediment bed (x=L). Expressed as a bulk volume of sediment per unit width per unit time. $q_s = \dot{E} \cdot L$.

q_s^*: dimensionless transport rate, $q_s^* = \frac{q_s \mu}{\tau d^2} = \frac{q_s \nu}{u^{*2} d^2}$ where τ ($=\rho u^{*2}$) is the fluid shear stress, μ ($= \rho\nu$) the fluid viscosity.

K': measured specific electrical conductance of the flume water in μmho/cm.

Salt: electrolyte (if any) that was added to the flume water.

pH: measured pH of the flume water during the experiment.

5.3 40-m flume

The primary purpose of these experiments (Series A-F) was to measure the effect of flow Reynolds number on the sediment mobility. The test section was lengthened after series C to reduce the fraction of sediment affected by the initial scour region, and to verify that the results were independent of the length of the sediment bed.

Expt. No.	d (μm)	Q (l/s)	D (cm)	Temp. (°C)	ν (cm^2/s)	U (cm/s)	Re (-)	*f* (-)	u* (mm/s)	Re* (-)	τ* (-)	E (μm/hr)	q_s (mm^2/s)	q_s* (-)
A-1	41	13.42	11	20	0.01	11.09	40663	0.0223	5.85	0.240	0.057	2.88	1.60E-4	0.0028
A-2	41	16.80	11	20	0.01	13.89	50921	0.0210	7.12	0.292	0.084	11.1	6.17E-4	0.0072
A-3	41	21.09	10.95	20	0.01	17.51	63951	0.0199	8.73	0.358	0.126	46.1	2.56E-3	0.0200
A-4	41	24.78	11	20	0.01	20.48	75078	0.0191	10.00	0.410	0.166	219.8	1.22E-2	0.0726
A-5	41	28.54	10.9	20	0.01	23.80	86607	0.0184	11.42	0.468	0.216	502.1	2.79E-2	0.1272
A-6	41	18.90	11.5	20	0.01	14.94	56857	0.0205	7.56	0.310	0.095	18.2	1.01E-3	0.0105
A-7	41	18.87	10.9	20	0.01	15.74	57265	0.0204	7.95	0.326	0.105	23.9	1.33E-3	0.0125
A-8	41	18.87	11.4	20	0.01	15.05	56834	0.0205	7.61	0.312	0.096	18.4	1.02E-3	0.0105
A-9	41	20.70	11.45	20	0.01	16.43	62291	0.0200	8.22	0.337	0.112	27	1.50E-3	0.0132
A-10	41	21.94	11.35	20	0.01	17.58	66145	0.0197	8.72	0.358	0.126	49.7	2.76E-3	0.0216
A-11	41	23.09	11.35	20	0.01	18.50	69615	0.0195	9.12	0.374	0.138	51.9	2.88E-3	0.0206
A-12	41	24.53	11.35	20	0.01	19.65	73932	0.0192	9.61	0.394	0.153	93.3	5.18E-3	0.0334
A-13	41	24.39	11.45	20	0.01	19.36	73401	0.0192	9.49	0.389	0.149	78.6	4.37E-3	0.0289
B-1	41	62.90	38.9	20	0.01	14.70	133975	0.0165	6.68	0.274	0.074	11.2	6.22E-4	0.0083
B-2	41	86.51	40.25	20	0.01	19.54	181650	0.0153	8.55	0.350	0.121	30.3	1.68E-3	0.0137
B-3	41	99.04	40.25	20	0.01	22.37	207948	0.0148	9.62	0.394	0.153	122.3	6.79E-3	0.0437
B-4	41	114.10	39.55	20	0.01	26.23	241362	0.0143	11.07	0.454	0.203	549.1	3.05E-2	0.1480
B-5	41	85.44	40	20	0.01	19.42	179866	0.0153	8.50	0.349	0.120	46.1	2.56E-3	0.0211
B-6	41	63.65	39.8	20	0.01	14.54	134284	0.0165	6.60	0.271	0.072	5.81	3.23E-4	0.0044

Table 5.1: Summary of data for the 20 x 8 cm sediment bed in the 40-meter flume (continued on next page). All experiments were conducted in Pasadena tap water (conductance ~ 850 μmho/cm, pH ~ 8.5).

Expt. No.	d (μm)	Q (l/s)	D (cm)	Temp. (ºC)	ν (cm^2/s)	U (cm/s)	Re (-)	*f* (-)	u* (mm/s)	Re* (-)	τ* (-)	E (μm/hr)	q_s (mm^2/s)	q_s* (-)
B-7	41	55.28	39.8	20	0.01	12.63	116619	0.0171	5.84	0.239	0.056	1.61	8.94E-5	0.0016
B-8	41	46.86	39.8	20	0.01	10.70	98868	0.0178	5.05	0.207	0.042	0.565	3.14E-5	0.0007
B-9	41	63.93	40.45	20	0.01	14.37	133965	0.0165	6.53	0.268	0.071	4.9	2.72E-4	0.0038
B-10	41	74.04	40.15	20	0.01	16.76	155629	0.0159	7.48	0.307	0.093	20.8	1.16E-3	0.0123
B-11	41	56.74	40.25	20	0.01	12.82	119136	0.0170	5.91	0.242	0.058	1.96	1.09E-4	0.0019
C-1	69	23.59	11.35	20	0.01	18.90	71112	0.0194	9.29	0.641	0.085	96.4	5.36E-3	0.0130
C-2	69	20.76	11.45	20	0.01	16.48	62489	0.0200	8.24	0.569	0.067	24.5	1.36E-3	0.0042
C-3	69	28.87	11.4	20	0.01	23.02	86957	0.0184	11.04	0.762	0.120	299	1.66E-2	0.0286
C-4	69	17.83	11.45	20	0.01	14.15	53658	0.0208	7.21	0.498	0.051	10.8	6.00E-4	0.0024
C-5	69	29.36	11.25	20	0.01	23.73	88639	0.0183	11.35	0.783	0.127	442	2.46E-2	0.0400

Table 5.1 (*continued*): Summary of data for the 20 x 8 cm sediment bed in the 40-meter flume. All experiments were conducted in Pasadena tap water (conductance ~ 850 μmho/cm, pH ~ 8.5).

Expt. No.	d (μm)	Q (l/s)	D (cm)	$Temp.$ (°C)	ν (cm^2/s)	U (cm/s)	Re (-)	f (-)	u^* (mm/s)	Re^* (-)	τ^* (-)	E (μm/hr)	q_s (mm^2/s)	q_s^* (-)
D-1	69	22.22	12.26	23	0.0094	16.48	70295	0.0194	8.12	0.60	0.06	10.9	1.21E-3	0.0036
D-2	69	25.62	12.36	23	0.0094	18.84	80909	0.0187	9.12	0.67	0.08	30.5	3.39E-3	0.0080
D-3	69	30.01	11.91	23	0.0094	22.90	95413	0.0180	10.86	0.80	0.12	156	1.73E-2	0.0290
D-4	69	19.19	12.41	23	0.0094	14.06	60573	0.0201	7.05	0.52	0.05	0.127	1.41E-5	0.0001
E-1	120.6	31.12	12.16	23	0.0094	23.27	98592	0.0178	10.98	1.41	0.07	62	6.89E-3	0.0037
E-2	120.6	34.84	11.86	23	0.0094	26.71	110880	0.0173	12.43	1.59	0.09	274	3.04E-2	0.0127
F-1	41	63.93	38.56	23	0.0094	15.07	145395	0.0162	6.78	0.30	0.08	2.75	3.06E-4	0.0037
F-2	41	50.51	27.96	23	0.0094	16.42	129532	0.0167	7.49	0.33	0.09	10.7	1.19E-3	0.0118
F-3	41	61.80	28.06	23	0.0094	20.02	158311	0.0158	8.91	0.39	0.13	35	3.89E-3	0.0274
F-4	41	48.16	20.8	23	0.0094	21.05	135170	0.0165	9.55	0.42	0.15	64.1	7.12E-3	0.0436
F-5	41	62.57	21.66	23	0.0094	26.26	173659	0.0155	11.55	0.50	0.22	283.65	3.15E-2	0.1321

Table 5.2: Summary of data for experiments conducted with the 40 x 8 cm sediment bed in the 40-meter flume. All experiments were conducted in Pasadena tap water (conductance ~ 850 μmho/cm, pH ~ 8.5).

Expt. No.	d (μm)	Q (l/s)	D (cm)	Temp. (°C)	ν (cm^2/s)	U (cm/s)	Re (-)	*f* (-)	u* (mm/s)	Re* (-)	τ* (-)	E (μm/hr)	q_s (mm^2/s)	q_s* (-)
G-1	41	4.09	10.3	23	0.0094	14.98	36935	0.0228	7.99	0.35	0.11	24.26	2.70E-3	0.0236
G-2	41	5.00	10.2	23	0.0094	18.48	45321	0.0217	9.62	0.42	0.15	70.8	7.87E-3	0.0476
G-3	41	5.84	10.3	23	0.0094	21.40	52764	0.0208	10.92	0.48	0.20	190	2.11E-2	0.0989
G-4	41	3.29	10.3	23	0.0094	12.05	29707	0.0241	6.61	0.29	0.07	1.7	1.89E-4	0.0024
G-5	41	4.12	10.2	23	0.0094	15.24	37370	0.0227	8.12	0.35	0.11	29.1	3.23E-3	0.0274
G-6	41	3.91	10.1	23	0.0094	14.62	35649	0.0230	7.84	0.34	0.10	21.3	2.37E-3	0.0215
G-7	41	4.94	10.3	23	0.0094	18.10	44632	0.0217	9.43	0.41	0.15	52	5.78E-3	0.0363
G-8	41	4.01	10.4	23	0.0094	14.54	36053	0.0229	7.79	0.34	0.10	16.7	1.86E-3	0.0171
G-9	41	4.96	10.4	23	0.0094	18.00	44624	0.0217	9.38	0.41	0.15	55.6	6.18E-3	0.0392
G-10	41	3.20	10.4	23	0.0094	11.62	28807	0.0243	6.40	0.28	0.07	0.356	3.96E-5	0.0005
H-1	41	3.96	10.3	23	0.0094	14.52	35808	0.0230	7.78	0.34	0.10	0.56	6.22E-5	0.0006
H-2	41	5.00	10.3	23	0.0094	18.32	45174	0.0217	9.54	0.42	0.15	0.31	3.44E-5	0.0002
H-3	41	5.84	10.1	23	0.0094	21.82	53216	0.0208	11.13	0.49	0.21	106.8	1.19E-2	0.0536
I-1	69	4.88	10.3	23	0.0094	17.88	44082	0.0218	9.33	0.69	0.09	32.8	3.64E-3	0.0083
I-2	69	5.65	10.2	23	0.0094	20.91	51275	0.0210	10.71	0.79	0.11	369.1	4.10E-2	0.0706
I-3	69	5.27	10	23	0.0094	19.87	48190	0.0213	10.26	0.75	0.10	150.5	1.67E-2	0.0314
I-4	69	4.30	10.4	23	0.0094	15.59	38661	0.0225	8.28	0.61	0.07	18.1	2.01E-3	0.0058
I-5	69	5.11	10.4	23	0.0094	18.53	45955	0.0216	9.63	0.71	0.09	72.9	8.10E-3	0.0173

Table 5.3: *Summary of data for experimental Series G, H, and I. Experiments were conducted in the 12-meter flume with the 40 x 8 cm sediment bed and Pasadena tap water (conductance ~ 850 μmho/cm, pH ~ 8.5).*

Expt. No.	d (μm)	Q (l/s)	D (cm)	Temp. (°C)	ν (cm^2/s)	U (cm/s)	Re (-)	f (-)	u^* (mm/s)	Re^* (-)	τ^* (-)	E (μm/hr)	q_s (mm^2/s)	q_s^* (-)	K' (μmho/cm)	Salt	pH
J-1	41	4.33	10.8	23	0.0094	15.14	38326	0.0226	8.04	0.35	0.107	5.4	0.0006	0.005187	12.05		6.92
J-2	41	4.37	10.8	23	0.0094	15.26	38631	0.0225	8.10	0.35	0.109	19.2	0.002133	0.018188	15.1		7.05
J-3	41	4.44	10.7	23	0.0094	15.66	39448	0.0224	8.29	0.36	0.114	22.1	0.002456	0.019976	17.2		7.1
J-4	41	5.70	10.6	23	0.0094	20.29	50842	0.0210	10.41	0.45	0.179	73.4	0.008156	0.042118	19.2		7.1
K-1	69	4.96	10.6	23	0.0094	17.64	44205	0.0218	9.21	0.68	0.083	53.4	0.005933	0.01382	12.16	$NaHCO_3$	7.26
K-2	69	4.09	10.6	23	0.0094	14.58	36525	0.0229	7.79	0.57	0.060	19.7	0.002189	0.00712	13.45	$NaHCO_3$	7.23
K-3	69	5.51	10.4	23	0.0094	19.97	49526	0.0212	10.28	0.75	0.104	220	0.024444	0.045684	15.81	$NaHCO_3$	7.19
L-1	69	4.95	10.6	23	0.0094	17.62	44160	0.0218	9.20	0.68	0.083	89	0.009889	0.023073	1076	NaCl	7.33
L-2	69	4.12	10.6	23	0.0094	14.68	36797	0.0228	7.84	0.58	0.061	21.5	0.002389	0.00767	1025	NaCl	7.3
L-3	69	5.51	10.5	23	0.0094	19.82	49397	0.0212	10.20	0.75	0.102	219	0.024333	0.046174	1074	NaCl	7.3
L-4	69	5.01	10.4	23	0.0094	18.18	45072	0.0217	9.46	0.69	0.088	73	0.008111	0.017876	1061	NaCl	7.36
M-1	41	4.09	10.5	23	0.0094	14.71	36679	0.0228	7.86	0.34	0.102	12.7	0.001411	0.012769	1054	NaCl	7.31
M-2	41	4.87	10.4	23	0.0094	17.67	43804	0.0218	9.23	0.40	0.141	59.5	0.006611	0.04338	1075	NaCl	7.34
M-3	41	3.36	10.4	23	0.0094	12.21	30267	0.0240	6.68	0.29	0.074	3.12	0.000347	0.004344	1079	NaCl	7.34
N-1	41	4.11	10.4	23	0.0094	14.90	36944	0.0228	7.95	0.35	0.105	26.06	0.002896	0.025597	13.36	$NaHCO_3$	7.12
N-2	41	4.85	10.4	23	0.0094	17.61	43666	0.0219	9.21	0.40	0.140	56.3	0.006256	0.041274	15.1	$NaHCO_3$	7.1
N-3	41	3.29	10.5	23	0.0094	11.82	29457	0.0241	6.49	0.28	0.070	5.4	0.0006	0.007969	16.07	$NaHCO_3$	7.11
N-4	41	4.90	10.4	23	0.0094	17.78	44079	0.0218	9.28	0.40	0.143	73.3	0.008144	0.052859	17.35	$NaHCO_3$	7.02

Table 5.4: Summary of data for experimental Series J, K, L, M, and N. Experiments were conducted in the 12-meter flume with the 40 x 8 cm sediment bed.

Expt. No.	d (μm)	Q (l/s)	D (cm)	Temp. (°C)	ν (cm^2/s)	U (cm/s)	Re (-)	*f* (-)	u^* (mm/s)	Re^* (-)	τ^* (-)	E (μm/hr)	q_s (mm^2/s)	q_s^* (-)	K' (μmho/cm)	Salt	pH
O-1	15	3.33	10.2	23	0.0094	12.31	30181	0.0240	6.74	0.11	0.2056	11.6	1.29E-3	0.1186			
O-2	15	4.15	10.1	23	0.0094	15.50	37806	0.0227	8.25	0.13	0.3084	41	4.56E-3	0.2796	10.1		7.13
O-3	15	2.59	10.3	23	0.0094	9.51	23440	0.0255	5.37	0.09	0.1307	0	0.00E+0	0.0000	17.1		7.22
O-4	15	2.89	10.2	23	0.0094	10.70	26248	0.0248	5.96	0.10	0.1610	4	4.44E-4	0.0522	17.9		6.99
O-5	15	3.56	10.6	23	0.0094	12.68	31773	0.0237	6.90	0.11	0.2155	9	1.00E-3	0.0878	20.1		6.92
P-1	15	3.57	10.5	23	0.0094	12.83	31970	0.0236	6.97	0.11	0.2201	8.9	9.89E-4	0.0850	130.8	NaCl	7.16
P-2	15	3.19	10.5	23	0.0094	11.48	28615	0.0243	6.33	0.10	0.1813	3.3	3.67E-4	0.0383	131.4	NaCl	7.14
P-3	15	4.15	10.4	23	0.0094	15.05	37327	0.0227	8.03	0.13	0.2918	21.5	2.39E-3	0.1550	131.4	NaCl	7.23
P-4	15	2.71	10.4	23	0.0094	9.83	24384	0.0253	5.53	0.09	0.1385	0	0.00E+0	0.0000	130	NaCl	7.24
Q-1	15	3.36	10.4	23	0.0094	12.18	30199	0.0240	6.67	0.11	0.2014	6.3	7.00E-4	0.0658	7.6		6.6
R-1	15	3.57	10.4	23	0.0094	12.95	32105	0.0236	7.03	0.11	0.2242	0	0.00E+0	0.0000	867	NaCl	7.25
R-2	15	4.13	10.3	23	0.0094	15.13	37321	0.0227	8.07	0.13	0.2949	0.4	4.44E-5	0.0029	934	NaCl	7.47
R-3	15	4.88	10.2	23	0.0094	18.07	44317	0.0218	9.43	0.15	0.4027	1.22	1.36E-4	0.0064	905	NaCl	7.3

Table 5.5: Summary of data for experiments with 15 μm particles (Series O, P, Q, R, S, and T). Experiments were conducted in the 12-meter flume with the 40 x 8 cm sediment bed. Continued on next page.

Expt. No.	d (μm)	Q (l/s)	D (cm)	Temp. (°C)	ν (cm^2/s)	U (cm/s)	Re (-)	*f* (-)	u* (mm/s)	Re* (-)	τ* (-)	E (μm/hr)	q_s (mm^2/s)	q_s* (-)	K' (μmho/cm)	Salt	pH
S-1	15	3.56	10.4	23	0.0094	12.92	32041	0.0236	7.02	0.11	0.2234	0.8	8.89E-5	0.0075	75.8	$CaCl_2$	7.2
S-2	15	4.11	10.2	23	0.0094	15.19	37259	0.0227	8.10	0.13	0.2973	13.1	1.46E-3	0.0927	76.2	$CaCl_2$	7.17
S-3	15	3.80	10.3	23	0.0094	13.93	34344	0.0232	7.50	0.12	0.2550	1	1.11E-4	0.0082	78.1	$CaCl_2$	6.68
S-4	15	4.74	10.4	23	0.0094	17.20	42639	0.0220	9.02	0.14	0.3683	7.7	8.56E-4	0.0440	77.4	$CaCl_2$	7.24
O-6	15	3.59	10.2	23	0.0094	13.28	32571	0.0235	7.20	0.11	0.2350	16.85	1.87E-3	0.1508	7.5		6.8
T-1	15	4.19	10.3	23	0.0094	15.35	37866	0.0227	8.17	0.13	0.3025	22.1	2.46E-3	0.1537	72.4	$CaCl_2$	7.06
T-2	15	4.84	10.5	23	0.0094	17.41	43390	0.0219	9.11	0.15	0.3757	37.5	4.17E-3	0.2099	71.6	$CaCl_2$	7.06
T-3	15	3.57	10.5	23	0.0094	12.83	31970	0.0236	6.97	0.11	0.2201	6.8	7.56E-4	0.0650	71.5	$CaCl_2$	7.1
Q-2	15	3.36	10.4	23	0.0094	12.18	30199	0.0240	6.67	0.11	0.2014	6.1	6.78E-4	0.0637	6.77		6.55

Table 5.5 (continued): Summary of data for experiments with 15 μm particles (Series O, P, Q, R, S, and T). Experiments were conducted in the 12-meter flume with the 40 x 8 cm sediment bed.

Expt. No.	d (μm)	Q (l/s)	D (cm)	Temp. (°C)	ν (cm^2/s)	U (cm/s)	Re (-)	*f* (-)	u^* (mm/s)	Re^* (-)	τ^* (-)	E (μm/hr)	q_s (mm^2/s)	q_s^* (-)	K' (μmho/cm)	Salt	pH
U-1	26.5	3.73	10.5	23	0.0094	13.42	33456	0.0234	7.25	0.204	0.135	19.25	2.14E-3	0.0544	23	$NaHCO_3$	7.5
U-2	26.5	3.06	10.5	23	0.0094	10.98	27375	0.0246	6.09	0.172	0.095	3.8	4.22E-4	0.0153	23.7	$NaHCO_3$	7.6
U-3	26.5	4.17	10.5	23	0.0094	14.98	37332	0.0227	7.98	0.225	0.163	37.5	4.17E-3	0.0875	26.3	$NaHCO_3$	7.63
U-4	26.5	2.74	10.6	23	0.0094	9.75	24431	0.0253	5.48	0.154	0.077	2.12	2.36E-4	0.0105	28.3	$NaHCO_3$	7.66
U-5	26.5	2.21	10.5	23	0.0094	7.94	19783	0.0266	4.58	0.129	0.054	0.95	1.06E-4	0.0067	30.7	$NaHCO_3$	7.7
V-1	26.5	3.76	10.6	23	0.0094	13.39	33556	0.0233	7.23	0.204	0.134	9.25	1.03E-3	0.0263	1118	NaCl	7.73
V-2	26.5	4.20	10.7	23	0.0094	14.82	37339	0.0227	7.90	0.223	0.160	17.3	1.92E-3	0.0412	1108	NaCl	7.7
V-3	26.5	2.96	10.7	23	0.0094	10.45	26319	0.0248	5.82	0.164	0.087	0.53	5.89E-5	0.0023	1105	NaCl	7.66
V-4	26.5	2.96	10.7	23	0.0094	10.45	26319	0.0248	5.82	0.164	0.087	0	0.00E+0	0.0000	1114	NaCl	7.72
U-6	26.5	3.73	10.3	23	0.0094	13.68	33740	0.0233	7.39	0.208	0.140	23.6	2.62E-3	0.0643	15	$NaHCO_3$	7.19
W-1	26.5	3.73	10.4	23	0.0094	13.53	33537	0.0234	7.31	0.206	0.137	1.42	1.58E-4	0.0040	756	$CaCl_2$	7.18
W-2	26.5	4.33	10.4	23	0.0094	15.70	38922	0.0225	8.32	0.235	0.178	2.6	2.89E-4	0.0056	746	$CaCl_2$	7.35
W-3	26.5	4.31	10.3	23	0.0094	15.79	38930	0.0225	8.37	0.236	0.180	1.19	1.32E-4	0.0025	783	$CaCl_2$	6.15
W-4	26.5	4.31	10.3	23	0.0094	15.79	38930	0.0225	8.37	0.236	0.180	0	0.00E+0	0.0000	807	$CaCl_2$	6.23
X-1	26.5	3.67	10.55	23	0.0094	13.14	32838	0.0235	7.12	0.201	0.130	16.8	1.87E-3	0.0493	14.95	$NaHCO_3$	7.06
X-2	26.5	3.68	10.3	23	0.0094	13.48	33248	0.0234	7.29	0.206	0.136	18.5	2.06E-3	0.0517	107.1	$NaHCO_3$	8.25
X-3	26.5	3.67	10	23	0.0094	13.86	33615	0.0233	7.49	0.211	0.144	10	1.11E-3	0.0265	1061	NaCl	8.72
X-4	26.5	3.62	10.3	23	0.0094	13.28	32749	0.0235	7.20	0.203	0.133	11.6	1.29E-3	0.0333	1111	NaCl	6.65

Table 5.6: Summary of data for experiments with 26.5 μm particles (Series U, V, W, and X). Experiments were conducted in the 12-meter flume with the 40 x 8 cm sediment bed.

5.3.1 20x8 cm Sediment Bed

Experiments in series A, B, and C were conducted with a sediment bed 20 cm in streamwise length, and 8 cm wide. The bed elevation was measured along four transects 15 mm apart, symmetric about the center of the sediment bed. The laser displacement meter measured the bed elevation at 124 points along each transect. Each measurement point was 1.5875 mm (1/16 inch) apart. The surface of the upstream edge of the test tray was measured in each transect to provide a correction for any instrumental drift (14 points per transect). The maximum correction from these measurements was about 8 μm. Each measured point represents the average of 20 values (approximately 1/2 s) obtained from the analog output of the displacement meter.

For illustration, detailed results from experiment B-10 are shown in Figure 5.1 through Figure 5.4. Other than sediment transport rate and rate of bedform growth, all other experiments are qualitatively similar. A time series of bed surface elevation measurements for experiment B-10 is presented in Figure 5.1, showing longitudinal profiles at half-hour intervals from the start of the experiment (t=0). Only the third transect is shown (four transects were measured, each 15 mm apart), consisting of 124 measurement points, 1.5875 mm apart. The initial bump at the upstream (x~10 mm) is due to the transport that occurred while the flow was being increased to the final flow rate (several minutes), and during the measurement of the first two transects (about 15 minutes). The vertical scale is greatly exaggerated, being about 66 times the horizontal. The images are displaced downwards by 200 μm for each time-step shown. Downstream of an initial scour region, a series of bedforms is seen to form and propagate downstream. These bedforms continue to grow in amplitude and wavelength for the duration of the

experiment. After three hours had elapsed, the crest-to-trough amplitude was about 0.8mm for the initial scour ripple, and only 0.3 mm for the ripples downstream of it. The typical wavelength of these ripples was about 25mm, or about 80 times the height. Compared to ripples formed on a sand bed, these have an unusually low height-to-wavelength ratio.

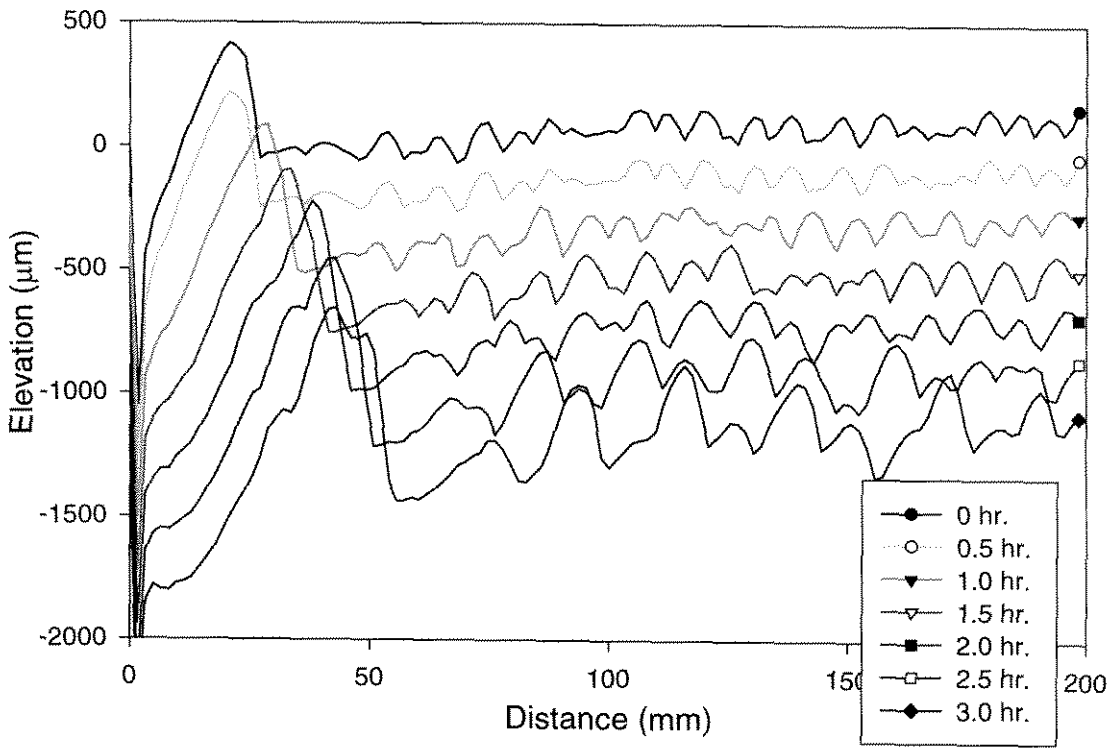

Figure 5.1: Surface elevation profiles for Experiment B-10, transect #3. Conducted in 40-meter flume with 20x8 cm sediment bed (d = 41μm, $\tau^* = 0.093$, $q_s^* = 0.012$). Each profile is displaced downward by 200 μm to separate the curves. The legend gives the elapsed time in hours.

The mean surface elevation along each transect is computed as the integral of the surface elevations measurements along each transect, normalized by the length of the test bed and corrected for instrumental drift. The average of the four transects is plotted vs. time in Figure 5.2 as the deviation from the initial surface elevation. The correction shown on the right ordinate is the measured average elevation of the upstream portion of

the test tray and represents the instrumental drift (Equation (5.3)). The mean erosion rate (rate of decrease of the bed surface) is found from the linear regression to the mean bed elevation over the period from 0.5 to 3.0 hours. After 3 hours, the bedform propagation velocity became sufficiently small (~15 mm/hr) compared to the wavelength (~25 mm), that the rate of erosion varied as they progressed off the test section. For this experiment, the first profile was also excluded because of the (relatively) large instrumental drift.

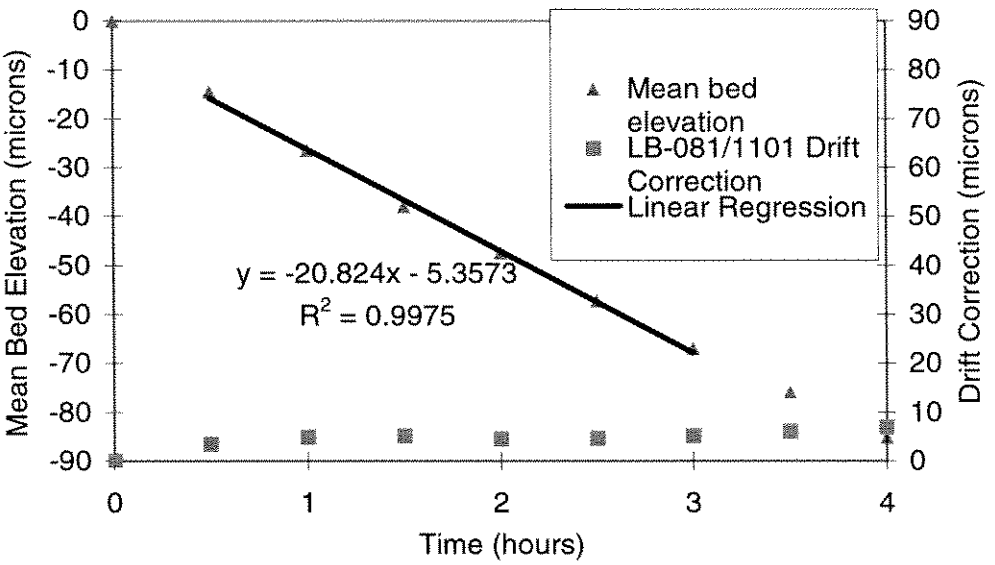

Figure 5.2: Mean depth of sediment erosion during Experiment B-10 plotted against the elapsed time, in hours. The instrumental drift is shown on the right ordinate.

The assumption that the sediment transport is two-dimensional is verified by computing the sediment transport rate along each of the four transects independently (Figure 5.3). The corresponding estimations for the volume flux of sediment are 21.9 μm/hr, 22.9 μm/hr, 20.5 μm/hr, and 18.9 μm/hr for transects one through four, respectively. These vary by +/- 10% of the mean (20.8 μm/hr), indicating that the sediment transport is essentially two-dimensional in nature.

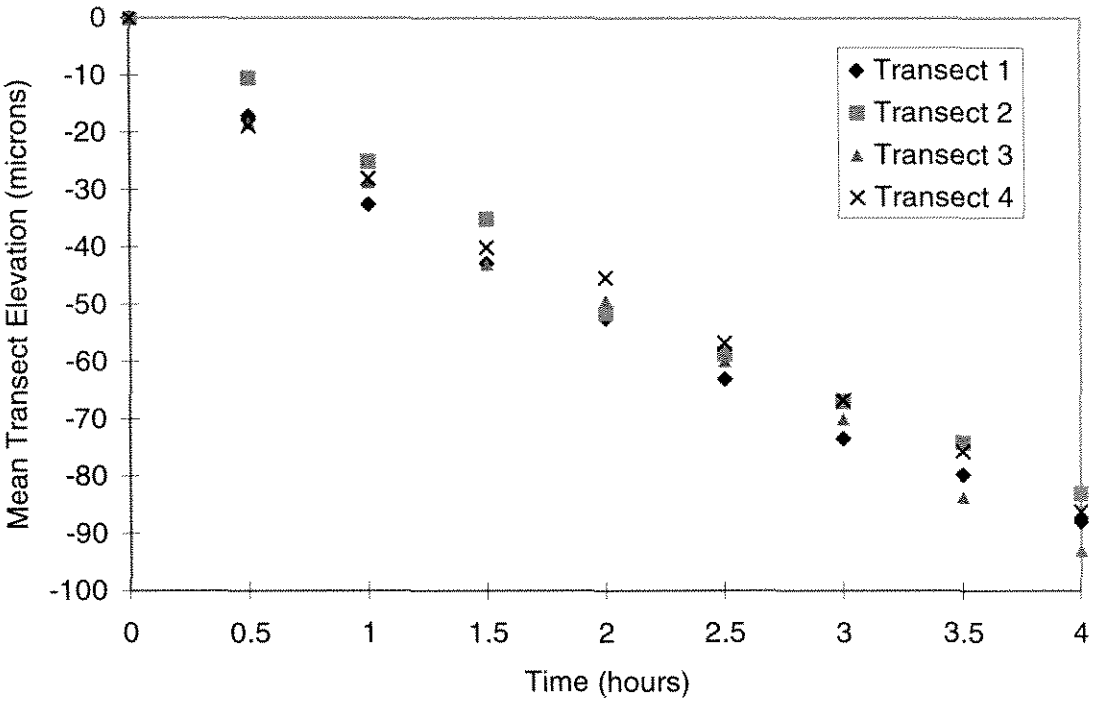

Figure 5.3: Variation in mean bed elevation along each of the four transects measured in experiment B-10.

Figure 5.4 shows the local sediment transport rate, $q_s(x)$, for experiment B-10 as a function of distance. These transport rates were calculated using equation (5.7) with Δt = 0.5 hours and the average of all four transects. The transport rate is constant in time, as shown by the overlapping curves Figure 5.4 (A). These curves are separated out in Figure 5.4 (B) for clarity.

The transport rate is, on average, independent of position over the downstream half of the sediment bed. The local variation in transport increases with time, and corresponds to ripple growth. The mean transport rate does not appear to vary as the

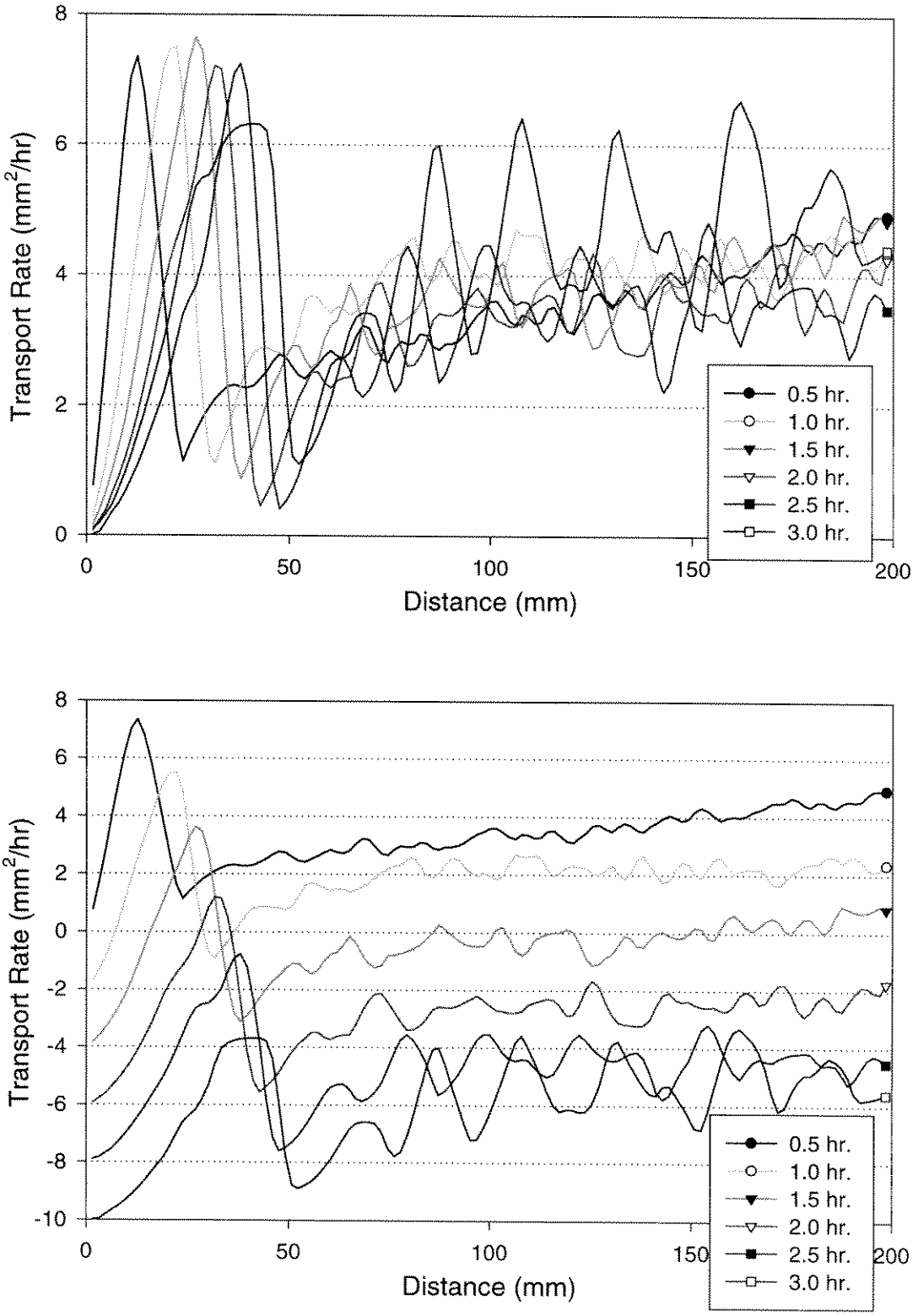

Figure 5.4: Total sediment transport rate as a function of distance from the leading edge of the test section for experiment B-10. (A) 1/2 hour averages, superimposed. (B) offset by 2mm²/hr. Curves are labeled by the elapsed time, in hours.

mean flow ripple amplitude increases. The effect of bedforms on the sediment transport rate is discussed further in Section 6.7.3.

The non-dimensional sediment transport rate (q_s*, Section 3.1) is plotted for all experiments (Series A, B, C) in Figure 5.5. The curve fit (dashed line in Figure 5.5) is the least squares regression for the logarithms of the variables:

$$q_s^* = 12.44(\tau^*)^{3.04} \qquad (5.8)$$

The regression was fit to the 41 μm data only (Series A and B). It will be used in graphs throughout this chapter as a basis for comparison.

The four-fold increase in flow depth from 11 cm to 40 cm between Series A and B caused no discernable difference in the dimensionless transport rates (Figure 5.5). The Reynolds number, based on the hydraulic radius, increased by a factor of 2.7 from

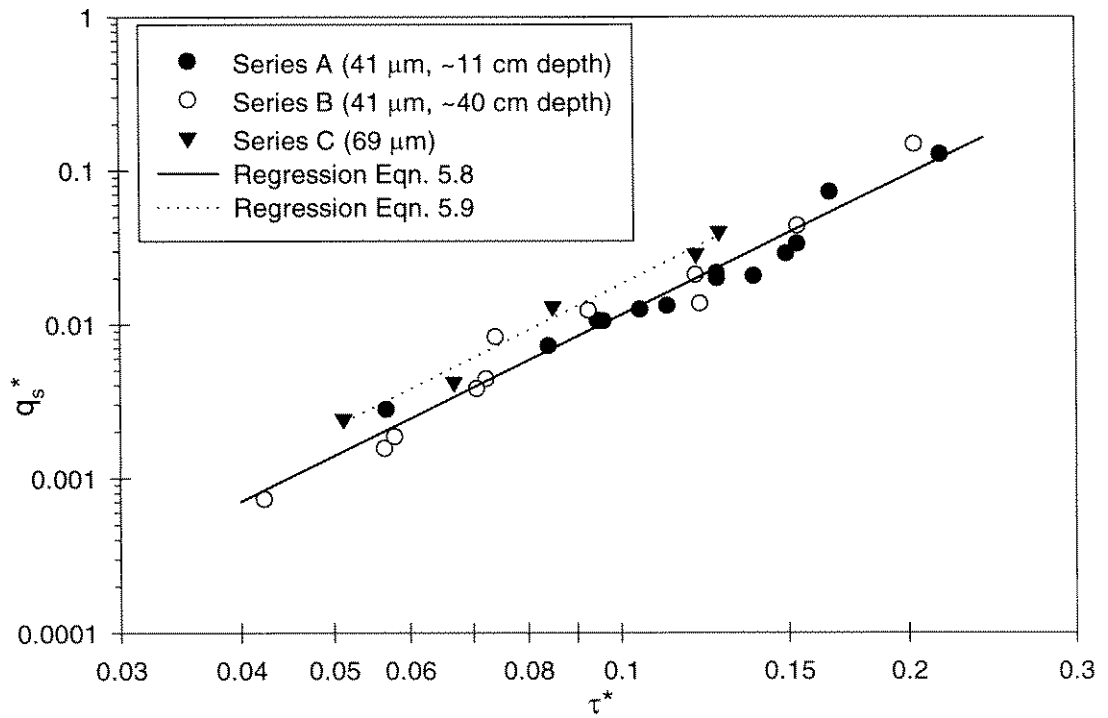

Figure 5.5: Dimensionless sediment transport rates (q_s*)for Experimental Series A, B, C plotted against dimesionless shear stress (τ*).

Series A ($4 \cdot 10^4$ - $9 \cdot 10^4$) to Series B ($1.2 \cdot 10^5$ - $2.4 \cdot 10^5$). From this insensitivity to the Reynolds number, experiments at the lower depth (10 cm) were inferred to be satisfactory for further experiments.

Series C, utilizing 69 μm glass beads, exhibited similar characteristics to series A and B. The normalized transport rates tended to be about 50% higher than that of series A and B. The regression line fit to Series C was:

$$q_s^* = 22.88(\tau^*)^{3.10} \qquad (5.9)$$

5.3.2 40x8 cm Sediment Bed

The experimental conditions of series A, B, and C were repeated with a test section 40 cm in streamwise length to ascertain if the transport rate truly reached a value independent of position (Series D, F).

Additionally, two experiments (Series E) were conducted with a fine quartz sand (d_g = 120.6 μm). This sand was used "as is," and no chemical washing was done in its preparation.

The bed's surface elevation was measured along streamwise transects over the test section. For experiments in series D, E, F, only one transect was made, with 249 points 1.5875 mm (1/16-inch) apart. The transect followed the centerline of the sediment bed, and the elevations were recorded as the laser displacement meter moved over the sediment bed in both directions. The calculations compared the sediment bed elevations (η) obtained in each direction with the subsequent transect in the same direction. The average of both directions is reported.

The experimental parameters for Series D, E, F are given in Table 5.2. The corresponding dimensionless transport rates are plotted in Figure 5.6. Also shown in Figure 5.6 is the regression Equation (5.8) to the 41 μm data in obtained in Series A and B with the 20 cm test section. The differences in q_s^* observed between the 20 cm and 40 cm sediment test beds was negligible.

The time series of the measured sediment bed elevations for the experiment F-2 are plotted in Figure 5.7. These results are illustrative of the experiments conducted with in the 40-meter flume, with the 40 cm sediment bed. The calculated local transport rates for experiment F-2 are plotted in Figure 5.8, and the rate of decrease of the sediment bed's elevation is shown in Figure 5.9. The experimental conditions (shear stress, mean

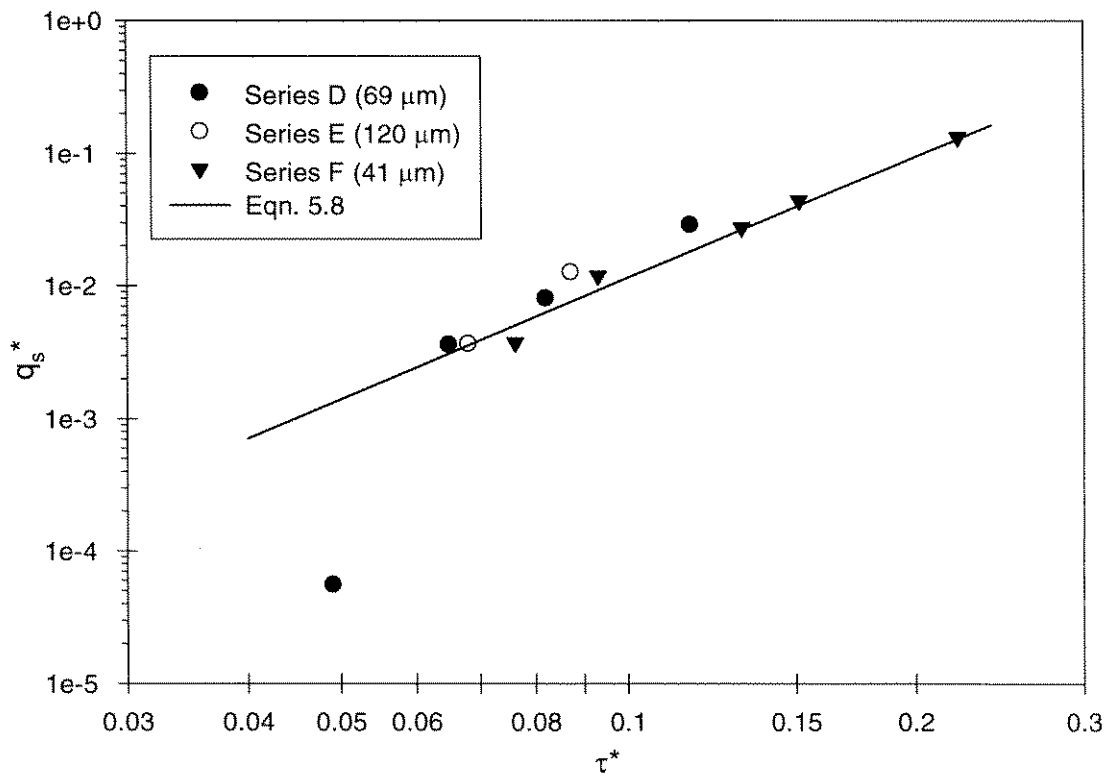

Figure 5.6: Dimensionless sediment transport rates for Series D (69 μm), E (120 μm sand), and F (41 μm). Regression line is from Figure 5.5, Equation (5.8).

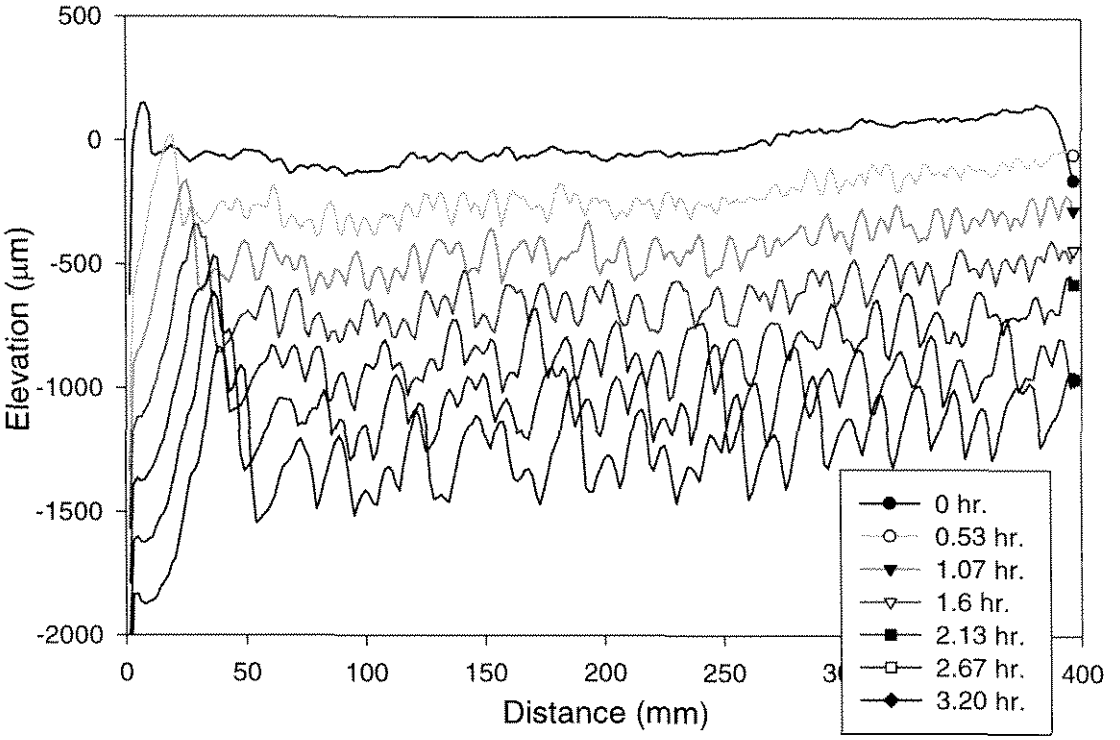

Figure 5.7: Surface elevation measurements for experiment F-2. Conducted in 40-meter flume with 40x8 cm sediment bed (d = 41μm, $\tau^* = 0.093$, $q_s^* = 0.012$). Each profile is displaced downward by 200 μm to separate the curves. The legend denotes the elapsed time in hours.

velocity) in this experiment are very similar to those in experiment B-10 which was illustrated in Figure 5.1 through Figure 5.4. However, the mean erosion rate in experiment B-10 was 20.8 μm/hr, almost double the 10.7 μm/hr measured for experiment F-2. The transport rates for the two experiments were similar, as a result of the longer length of the sediment bed in experiment F-2. Thus, the rate material is removed from the test section appears to be limited by the transport rate.

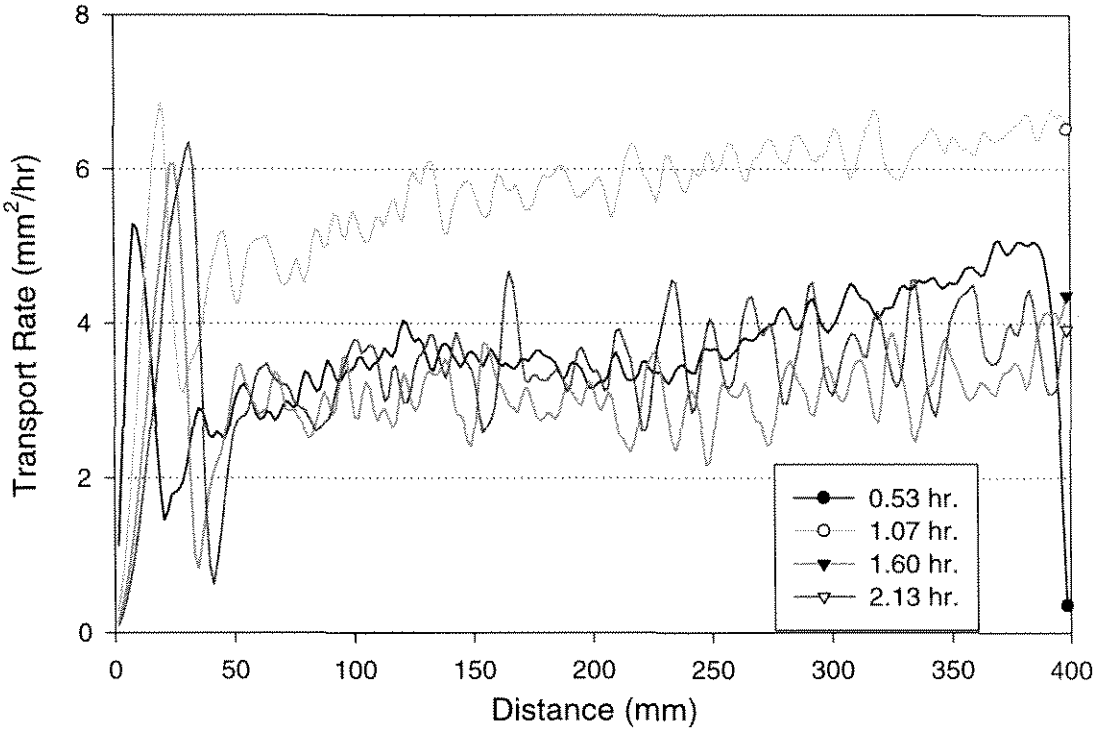

Figure 5.8: Half-hour averaged transport rates for experimental run F-2. Corresponding bed elevations are shown in Figure 5.7. The results are not offset. The legend denotes the elapsed time in hours.

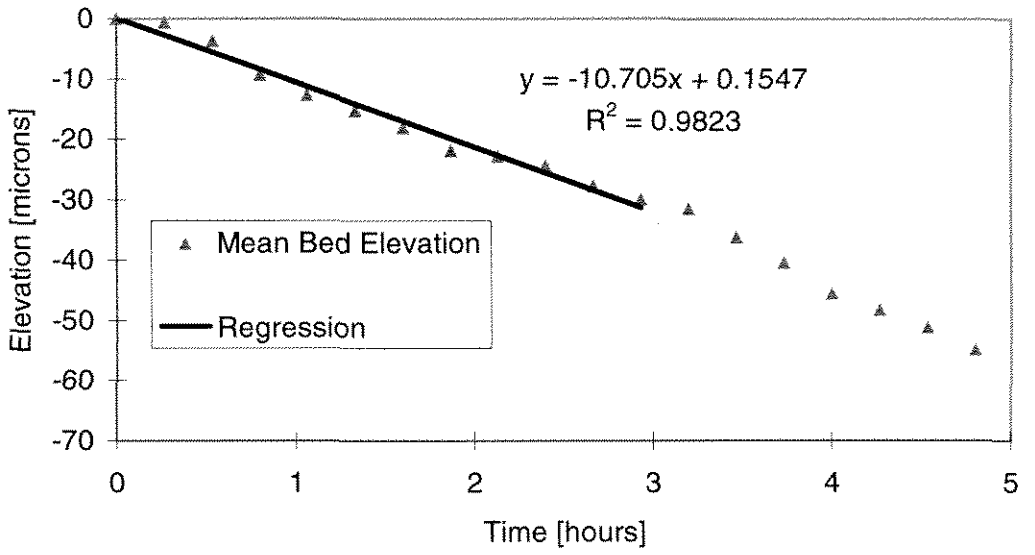

Figure 5.9: Mean bed elevation for experimental run F-2, and the rate of decrease (10.7 μm/hr). Variation due to bedform propagation can be seen for t > 3 hours. The corresponding bed elevations are shown in Figure 5.7.

5.4 12-meter Flume Experiments

The experimental apparatus was transferred to the smaller 12-meter flume to enable control over the flume water composition. The total water volume was reduced to 600L from the 30,000 L required for the 40-meter flume. The results from the 40-meter flume suggested that the slightly smaller flow Reynolds numbers ($3 \cdot 10^4 - 5 \cdot 10^4$) in this flume would not affect the results.

The LB-081/1101 laser displacement meter was fixed along the flume centerline. It recorded bed surface elevations as it moved in both directions along this transect. Each measurement point was 1.9949 mm (π/40 in.) apart. Surface elevations were recorded at 199 points over the sediment bed, and 10 to 12 points on the upstream surface of the sediment tray. In other aspects, the surface elevation measurements are identical to those in the 40-meter flume.

All experiments in the 12-meter flume used the 40x8 cm sediment bed, which comprised 30% of the flume's width, versus 7.3% in the 40-meter flume.

5.4.1 Series G, H, I (Pasadena Tap Water)

The first set of experiments were conducted with Pasadena tap water to verify similar behaviour in a flume with a smaller width/depth ratio (about 2.5 vs. 2.7 to 10 in the 40-meter flume). The water depth was constrained to be greater than 10 cm by the laser displacement meter requiring immersion under the water surface. Two sets of experiments (G, I) were conducted with 41 and 69 μm particles, as summarized in Table 5.3 and Figure 5.10. Compared to the regression line from Series A and B, higher dimensionless transport rates were observed with the 41 μm particles in the region near

$0.1 < \tau^* < 0.11$, and lower transport rates for $\tau^* < 0.1$. The 69 μm particles had similar dimensionless transport rates to what was observed in the 40-meter flume, as shown by the agreement with Equation (5.9) in Figure 5.10. However, experiment I-2 ($\tau^* = 0.11$) exhibited a transport rate almost three times larger than would be expected based on the 40-meter flume results. As in the 40-meter flume, the 69 μm sediment has a dimensionless transport rate 1.5 to 2 times that shown by the 41 μm particles under the same dimensionless shear stress.

The particles used in Series G and H were identical, except the particles used in Series G were subjected to an additional base/acid rinse immediately before use. Originally, these particles were washed according the procedure outlined in Section 4.3. Following this, they remained submerged in deionized water, in a closed container, for 3 months. No evidence of bacterial growth was apparent, and the particles were readily resuspended by shaking the container.

The particles in Series G were immersed in an equal volume of 1.0N NaOH overnight, rinsed with deionized water, then immersed in an equal volume of 1.0N HCl for a further 12 hours. This was followed by rinsing in deionized water until the pH no longer changed. On the other hand, the particles in Series H were only rinsed with deionized water prior to use.

The influence of this chemical treatment on the sediment transport rates is evident in Figure 5.10. Series G, as mentioned above, falls around the regression line found for freshly cleaned material (Series A, B), but the transport rate for Series H varied from only 0.6% (H-2) to 50% (H-3) of that observed for Series G.

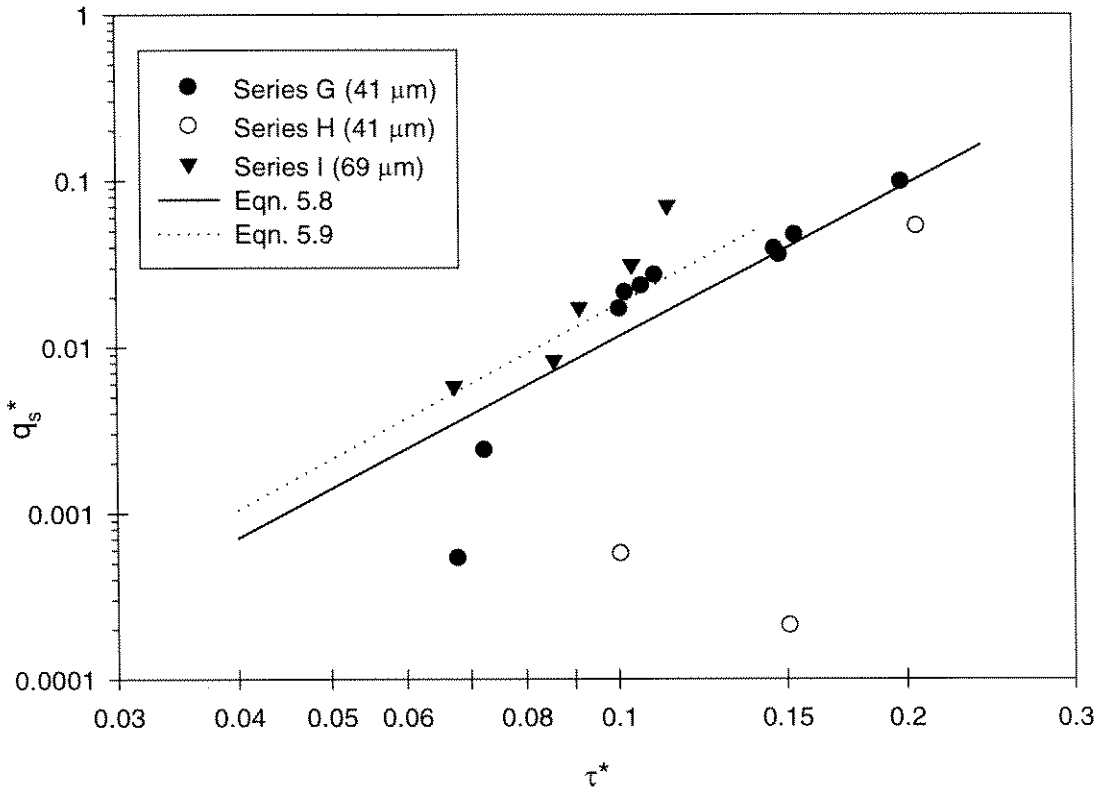

Figure 5.10: Dimensionless transport rate curves for experimental Series G (41 μm), H (41 μm, aged), and I (69 μm). Experiments were conducted in the 12-meter flume with the 40x8 cm sediment bed.

With the exception of experiments G-10 ($\tau^* = 0.068$), bedforms (ripples) developed during all experiments in Series G and I. Experiments G-10, H-1 and H-2 remained as a flat bed. Experiments G-10 and H-1 showed a constant transport rate in time, with a significant amount of scatter due to the small amount of material removed. Experiment H-2 had an initial transient period of rapid transport, followed by a reduced rate of transport (Figure 5.11). This type of transport behaviour was typical of "cohesive" experiments that exhibited a reduced transport rate. The rate of transport after the intial period ($t > 1$ hour) is reported for experiments that demonstrated this behaviour. This corresponds to the long term transport rate that sediment would exhibit. Use of the

initial rate would over-predict the sediment eroded by nearly 5 times over the 5.5 hours of this experiment, and much more over longer time periods.

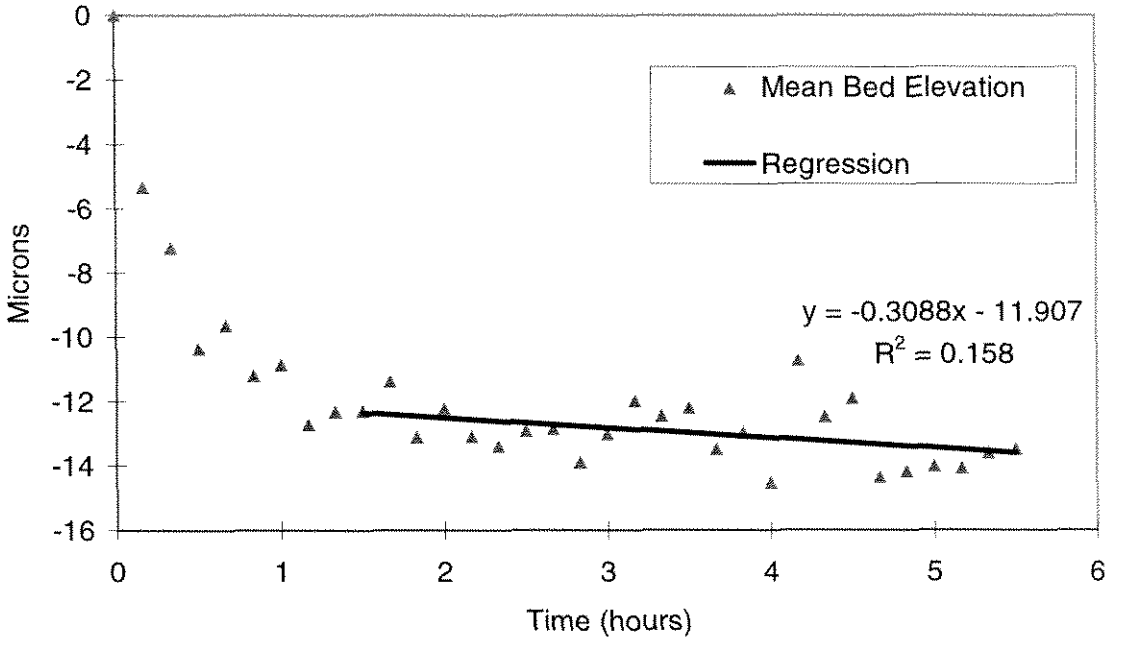

Figure 5.11: Mean bed elevation vs. time for experiment H-2 (41 μm, aged). The rate of decrease after t = 1 hour was taken to be representative of the long term rate.

5.4.2 Series J-N: 41, 69 μm Particles

To investigate the effect of flume water composition, experiments were performed in a simple electrolyte solution of known concentration. The flume was rinsed and filled with de-ionized water from the Caltech central supply, and the flume was left circulating for 12 hours to equilibrate with the atmosphere. For all experiments in Series K-N, 4.0g $NaHCO_3$ was added to the flume as a pH buffer. The particles were rinsed overnight in 1.0N NaOH, rinsed with de-ionized water, then rinsed overnight in 1.0N HCl, as described for Series G. The pH and conductivity were measured during each experiment.

The experimental conditions for these experiments are listed in Table 5.4 and Figure 5.12 summarizes the dimensionless transport rates as a function of τ^*. The transport rates for the 69 μm glass beads are virtually identical (<10% difference) for deionzed water (10^{-4} M $NaHCO_3$) and 10^{-2} M NaCl, with the exception of experiment L-1 (q_s^* was 1.8 times greater than experiments K-1, L-4).

In contrast, a significant decrease in transport rate (~ 50%) was observed for the 41 μm particles in 10^{-2}M NaCl solution, compared to the 10^{-4} M $NaHCO_3$ solution. The difference in the transport rates was less at higher dimensionless shear stresses, similar to what was observed with series H. In this case, there was no difference in the dimensionless transport rate between experiments M-2 and N-2 ($\tau^* = 0.14$, $q_s^* = 0.043$ vs. 0.041).

Compared with the results obtained in Pasadena tap water, the transport rates observed in deionized water (10^{-4}M $NaHCO_3$) are two to three times larger. To aid in comparison, Figure 5.12 shows the regression equations obtained from experiments with tap water in the 40-meter flume, equation (5.8) for 41 μm and equation (5.9) for 69 μm sediment. These results suggest that water with a higher ionic strength reduces the rate of sediment transport.

Series J was also run in deionized water, and had smaller amounts of transport that series N. The experiments with 41 μm glass beads in deionized water were rerun (series N) because it was felt that the washing of the beads had not removed all of the cohesion. This illustrates the important difference particle preparation can have on the results.

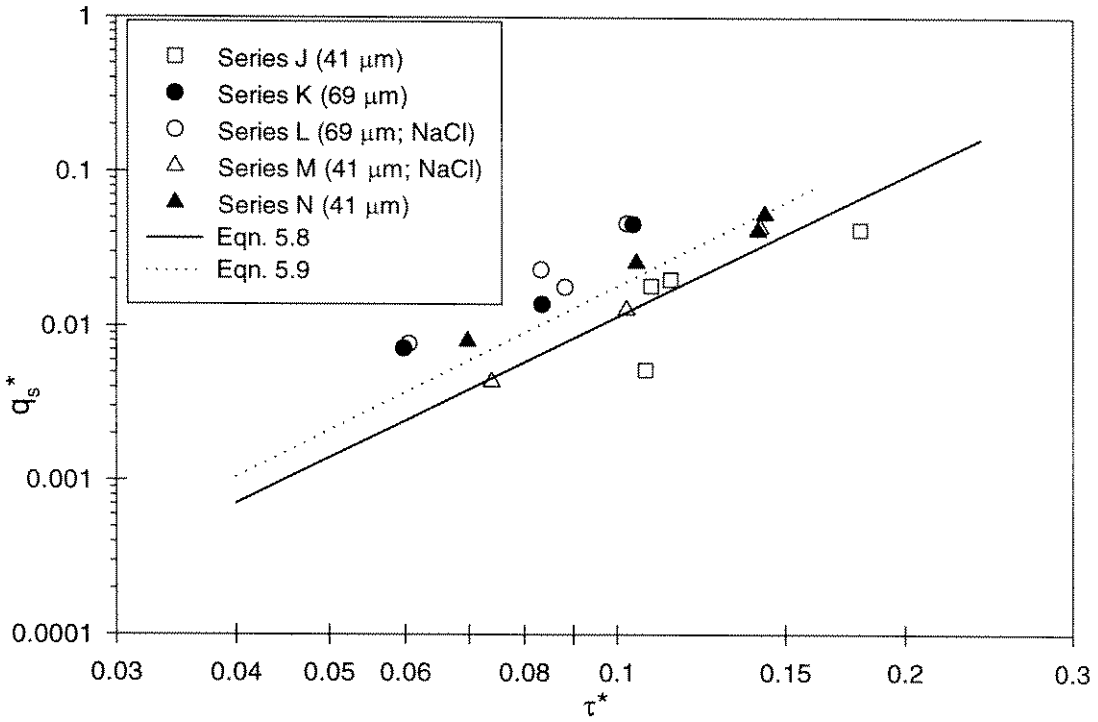

Figure 5.12: Dimensionless transport rates for Experimental Series J, K, L, M, N. 40x8 cm sediment bed in 12-m flume, with deionized water or 10^{-2} M NaCl solution.

5.4.3 Series O-T: 15 μm Particles

Experiments were conducted with glass beads having a geometric mean diameter of 15 μm, a standard deviation of 1.3, that had been cleaned according to the proceedure outlined in section 4.7. Each series had used flume water with a different chemical composition, obtained by addition of NaCl or $CaCl_2$ to de-ionized water. The results are summarized in Table 5.5 and Figure 5.13.

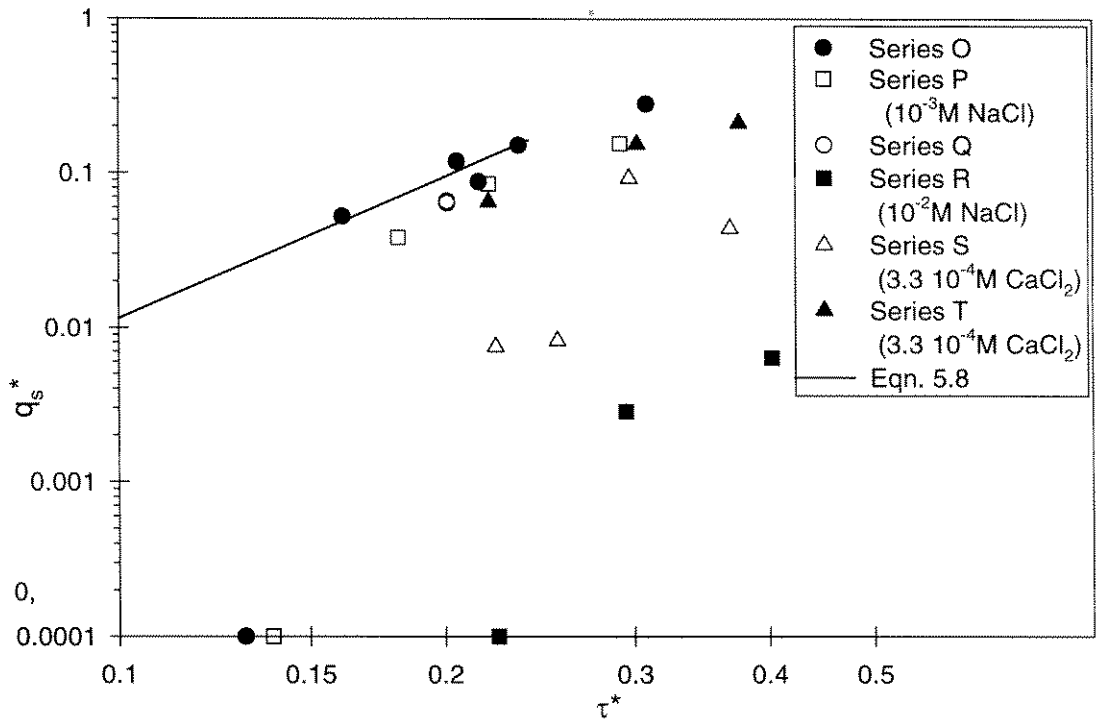

Figure 5.13: Dimensionless transport rates for 15 μm particles with varying water compositions. Series O and Q, deionized water; P, 10^{-3}M NaCl; R, 10^{-2}M NaCl; S, 3.3 10^{-4}M $CaCl_2$; T, 3.3 10^{-4}M $CaCl_2$). Experiments were conducted in the 12-meter flume with the 40x8 cm sediment bed.

Experiments O-1 through O-5 were conducted in DI water, without any additional electrolyte. The ionic strength was estimated at 10^{-4} M from the conductivity (10 to 20 μmho) of the flume water. The deionized water used to fill the flume had a conductivity of about 0.5 – 1 μmho. The increase in conductivity (and ionic strength) is a result of the dissolution of materials in the flume, primarily scale accumulated from past experimental work and dissolution of the iron and zinc components.

In these experiments 2-D bed-forms developed and propagated downstream. A series of surface elevation measurements from Experiment O-4 are shown in Figure 5.14. The corresponding transport rates are shown in Figure 5.15, but are not offset with each

time period, so it is easier to appraise the variation in transport rate with time. The transport rates are given as the time average over each three hour period, so t=3.0 hours corresponds to the transport from t=0 to t=3 hours. In this experiment, the t=3 hour transport rate increases linearly in distance. By t=6 hours, the transport rate appears to be relatively constant over final 200mm of the sediment bed. This initial increase in sediment transport rate was observed in multiple experiments, and is discussed further in Chapter 6.

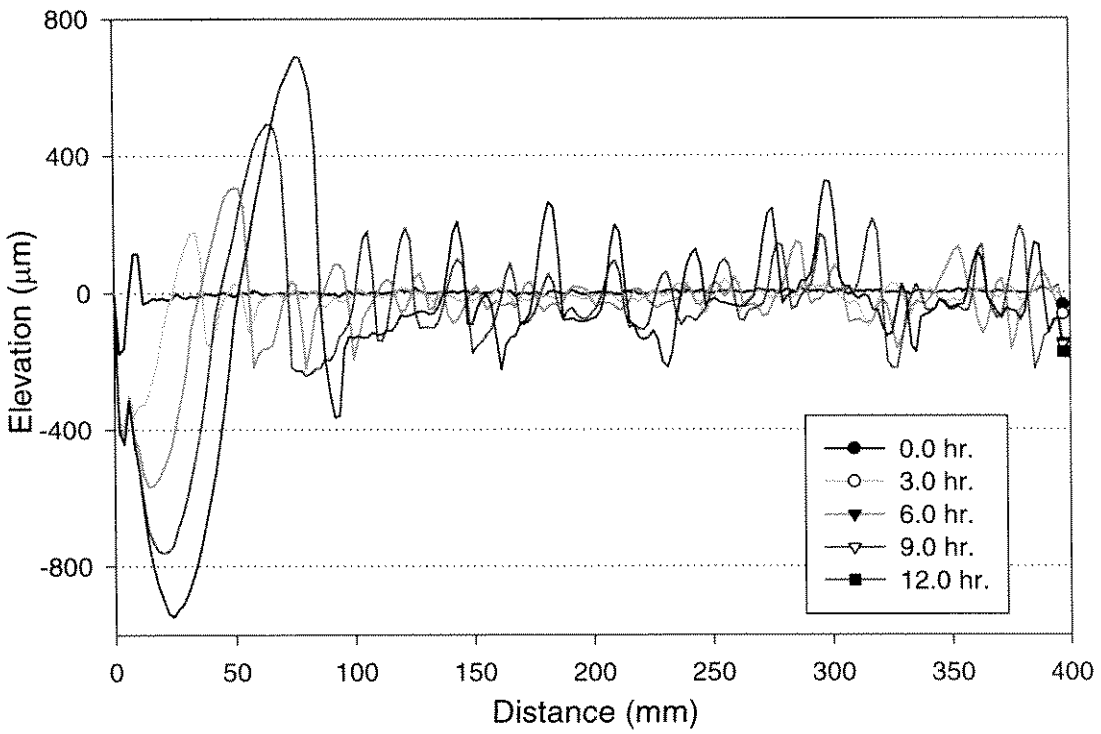

Figure 5.14: Surface elevation measurements from experiment O-4. Conducted in 12-meter flume with 40x8 cm sediment bed (d = 15μm, $\tau^* = 0.16$, $q_s^* = 0.052$). The bed profiles are not displaced downward in this figure. The legend denotes the elapsed time in hours.

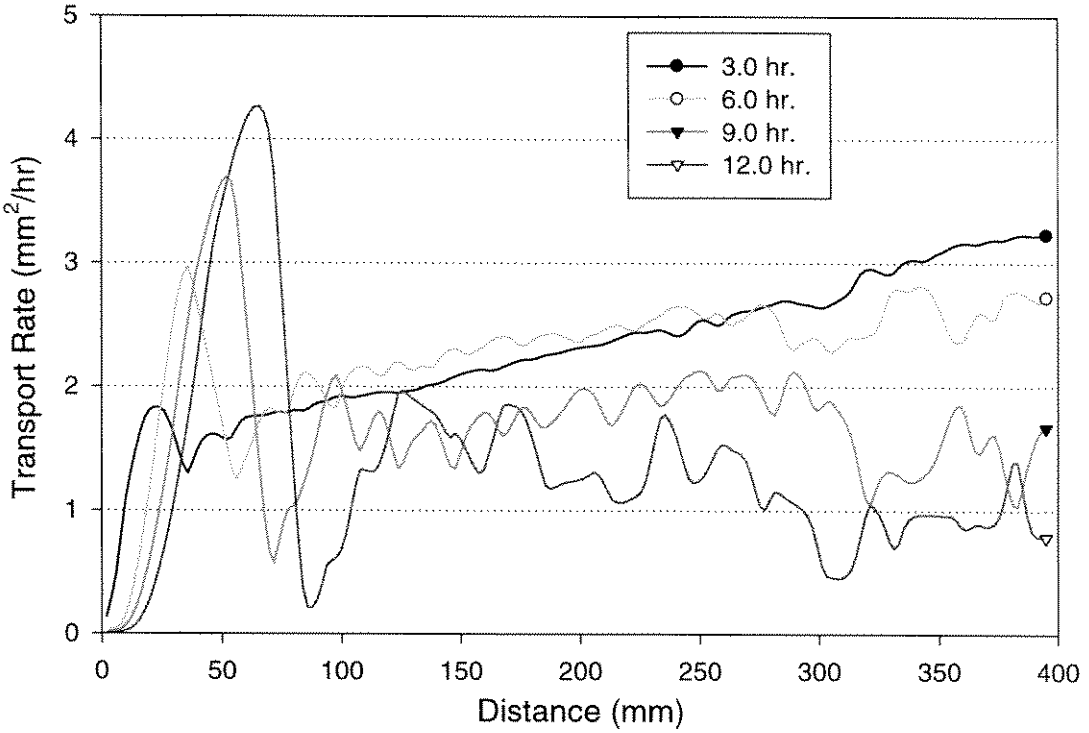

Figure 5.15: 3-hour averaged transport rates from experimental run O-4. Corresponding bed elevations are shown in Figure 5.14. The results are not offset. The legend denotes the elapsed time in hours.

The dimensionless transport rates (Figure 5.13) for Series O (15 μm) were similar to the regression obtained from Series A, Equation (5.8). However, an experiment at $\tau^* = 0.13$ (O-3) did not result in any measurable transport. This raises the possibility that these particles developed a slightly cohesive nature during these experiments.

Experiments in series P were conducted after adding 28.4g NaCl to the flume, creating an ionic strength of $8 \cdot 10^{-4}$ M. No measurable transport was observed in Experiment P-4 ($\tau^* = 0.14$). The transport rate in this series was about 60 – 80% of Series O, the difference increasing for the experiments at lower shear stresses.

After this experiment, the flume was drained, rinsed, and refilled with deionized water, and the pH was adjusted by addition of NaOH. The subsequent experimental run

(Q-1) resulted in a transport rate 45% lower than that observed in O-1 under similar flow conditions.

Subsequently, 284g NaCl was added to the flume to create an $8x10^{-3}$M NaCl solution for experiment R-1. Following this experiment, an additional 36g of NaCl was added to create a $9x10^{-3}$M solution for experiments R-2 and R-3. At $\tau^* = 0.22$ (R-1) no transport was observed, and at higher shear stresses a significant reduction in transport (99% for R-2) was observed compared to Series O and P (Figure 5.13). In experiments R-2, R-3, no ripples formed on the test bed. During these two experiments, the sediment bed remained smooth; sediment was visible on the flume bottom immediately downstream of the sediment bed.

After Series R, the flume was then drained and refilled with deionized water and 23.6g $CaCl_2 \cdot 2H_20$ (2.7×10^{-4}M $CaCl_2$). In experiment S-1 ($\tau^* = 0.22$) an initial lip of sediment formed, and moved downstream as a solitary ripple, but the remainder of the bed remained flat. Experiments S-2 and S-4 formed ripples, while no bedforms were observed to form during experiment S-3.

A subsequent experiment (not listed) in deionized water produced no transport, so the particles were removed and washed in 1.0N NaOH, followed by 1.0N HCl. The flume was drained, rinsed with chlorinated water, rinsed, and refilled with deionized water. Experiment O-6 was then conducted (labeled as series O because the particles were freshly cleaned). The measured sediment transport rate is in good agreement with the other experiments of Series O (Figure 5.13).

For the T series, 23.5g $CaCl_2 \cdot 2H_2O$ was added to the flume to create a similar electrolyte composition to Series S ($[CaCl_2] = 2.7 \times 10^{-4}$M). These experiments measured

a significantly higher transport rate than observed in Series S. Bedforms (ripples) were observed in all experiments in Series T. This discrepancy emphasizes the importance of the sediment's surface chemistry in determining the transport rate.

A final experiment (Q-2), run after draining the flume, and refilling with deionized water again produced a lower transport rate than series O, but similar to experiment Q-1.

5.4.4 Series U-X: 26.5 μm Particles

Table 5.6 presents the results obtained with particles of 26.5 μm mean diameter, which are summarized as a plot of q_s^* vs. τ^* in Figure 5.16. All of these experiments were conducted using de-ionized water with 4.0g $NaHCO_3$ (~$8x10^{-5}$ M) added to buffer the pH. Either $CaCl_2$ or NaCl was added as an ionic media. In experiments X-2 and X-4 the pH of the flume water was varied by addition of NaOH or HCl, respectively.

An increase in the ionic strength to ~10^{-2}M by addition of NaCl (350g) for Series V reduced the transport rate by ~50% compared to the results of Series U (no additional electrolyte). Experiments V-1 and V-2 formed ripples along the sediment bed, while experiment V-3 eroded as a flat bed. Following this, the particles sat (submersed) in the flume for a 4-day period between experiments V-3 and V-4. No transport could be measured for experiment V-4, despite a higher shear stress than experiment V-3.

At this time, the particles were removed and placed in 1.0N HCl overnight. Spectrophotometer measurements on the resulting solution indicated an absorbance of 0.288 at 335nm (corresponding to $FeCl_2^+$, see Section 4.3). This corresponds to [Fe] ~ 140 μM. The particles were removed from the acid, rinsed with deionized water until no

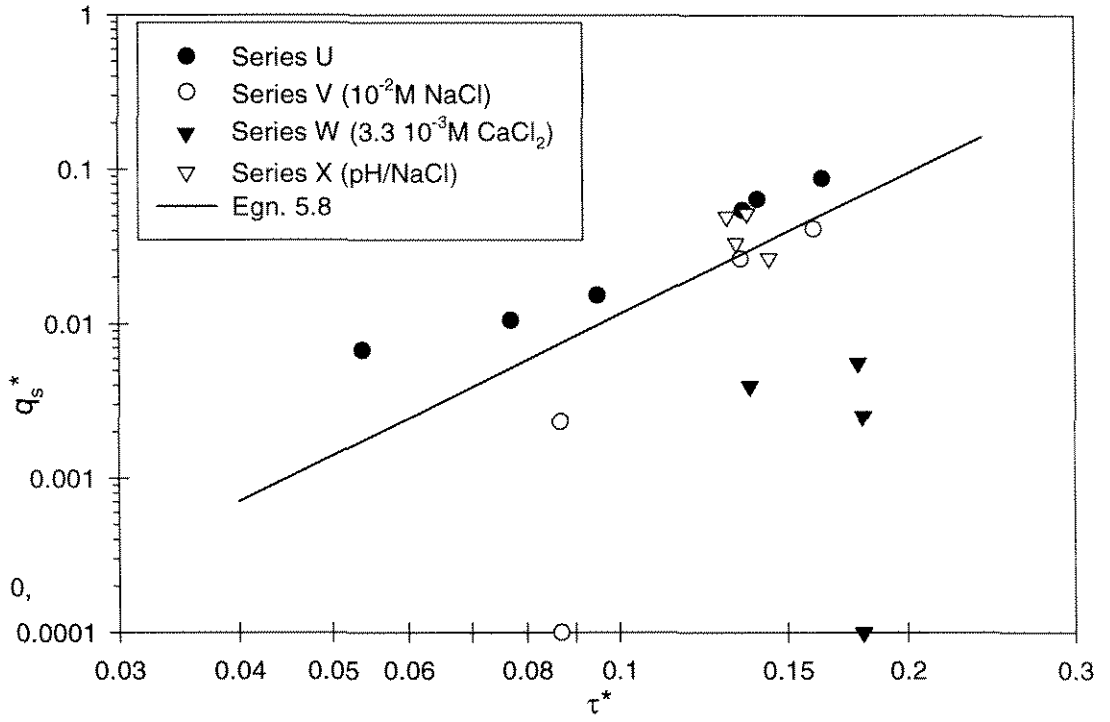

Figure 5.16: Dimensionless sediment transport rates for 26.5 μm particles. See Table 5.6 for details.

further pH change, and returned to the flume. The subsequent experiment, U-6, shows excellent agreement with the rest of series U, indicating that the presence of iron can create cohesive conditions. The source of iron is oxidation (rust) of the flume, visible along portions of the flume. See Appendix A for a discussion of modeling the water chemistry within the flume.

Series W was run in a 3.2 x 10^{-4} M $CaCl_2$ (281.6g $CaCl_2 \cdot 2H_20$) solution. This resulted in decreased transport rates compared with experiments using sodium chloride solution at the same ionic strength (Series V). Experiment W-1 eroded as a flat bed, while experiments W-2, W-3, and W-4 formed barchans (crescent shaped ripples) on the sediment bed. It appeared that these were formed from the upper layer of sediment, and the sediment beneath them was undergoing significantly less transport. Once the

barchans had propagated off the sediment test section, no new bedforms developed. The transport rates reported in Table 5.6 correspond to the transport rate after the barchans had propagated off the test section.

Immediately following these experiments, the particles were removed from the flume and placed in an equal volume of 1.0N HCl overnight. The resulting solution contained ~100 μM Fe. After rinsing with deionized water, the particles were returned to the flume, and experiment X-1 agrees well with Series U. Variation in pH over 2 pH units had little effect on the transport rate compared to the effect of ionic strength, as indicated by differences between X-2 and X-3. The change in ionic strength from 10^{-4}M or 10^{-3}M (X-1, X-2) to 10^{-2}M NaCl (X-3, X-4) reduced the transport rate by 50%, while the transport rate varied by ~10% from a 2 unit pH change (8.7 to 6.6 between X-3 and X-4).

5.5 Summary

Experiments were conducted with sediment beds having two different lengths in two large recirculating flumes. In each experiment, the surface elevation of the sediment bed was measured along streamwise transects, repetitively in time. From these measurements, the total volume of sediment material that eroded could be computed and expressed as a transport rate. This required the assumption that there was little cross-stream variation in the sediment transport rate, which was supported by a maximum 20% variation in transport rate computed along four transects.

The sediment was transported as bedload and formed ripples in the majority of experiments. The bedforms grew progressively grew in both amplitude and wavelength. The transport rate, averaged over the ripple wavelength, did not continue to increase with distance after an initial zone of scour. This implies that the particles were not suspended into the mean flow, but were moving in a layer along the bed. Exceptions to this and the effect of ripples on the transport rate are discussed in Chapter 6.

For mean flow Reynolds numbers ranging from $3 \cdot 10^4$ to $2.5 \cdot 10^5$, there was no measurable effect of the flow Reynolds number on the sediment transport rate. This supported conducting experiments at the lower flow Reynolds numbers ($2 \cdot 10^4 - 5 \cdot 10^4$) in the smaller 12-meter flume at depths of about 10 cm to investigate the effect of water composition on the transport rate. Experiments were conducted with four particle sizes (15, 26.5, 41, 69 μm) in deionized water, sodium chloride and calcium chloride solutions. For the same particle size, experiments conducted at higher salt concentrations resulted in a decreased transport rate. The relative decrease in transport increased at lower dimensionless shear stresses and with smaller particle sizes. The effect of water composition on the transport rate is discussed further in Chapter 6, and experiments conducted at similar salt concentrations are analyzed.

6 Discussion

This chapter contains a further discussion of the experimental results. The experiments with non-cohesive and cohesive characteristics are identified. The relationship of the non-cohesive experiments to the extension of the Shields curve to lower bed Reynolds numbers is given. The models developed in Chapter 3 are compared to both the non-cohesive and cohesive results and are shown to provide a reasonable fit to the results. The model predictions are then compared with experimental data from the literature. The technique for measuring sediment transport with a laser displacement meter is unique; the effectiveness of the experimental procedure, and sources of uncertainty in the measurements are discussed. Finally, the experimental observations of an initial transient transport rate and the effect of large bedforms (~1 mm) are presented.

6.1 Experimental Results

Length of sediment bed

Doubling the length of the sediment bed length did not change the transport rate by a measurable amount (Figure 5.6). The 40-cm test section provides a longer length to verify that the transport rate has indeed reached a constant value. For this reason it was used in all subsequent experiments.

Comparison of results for 10 and 40 centimeter depths

The flow Reynolds number was varied by changing the water depth to determine if turbulent eddies could entrain fine particles into suspension. The inability to distinguish any effects of flow depth (Reynolds number) between 10 and 40 centimeters suggests that the presence of the relatively impermeable sediment bed (wall) sufficiently dampens the vertical velocity fluctuations (due to turbulent eddies), preventing direct suspension of the sediment bed at shear stresses slightly above critical. This negative finding justified utilizing the smaller 12-meter flume for the tests with controlled water chemistry.

Comparison of silt and fine sand

Series E measured the transport rates of a fine quartz sand, 120.6 mm in diameter. While the dimensionless transport rates (Figure 5.6) are in agreement with Series D, the ripples formed so quickly that the test plate was scoured to its depth (3 mm) after 2 (E-2) or 5 (E-1) bed profiles were measured. The transport rates are correspondingly uncertain.

Effect of using Pasadena tap water

In light of the experiments conducted with deionized water in the 12-m flume (see Figure 5.12), it appears that the higher dimensionless transport rates (q_s^*) for the 69 μm sediment (Series C, D) compared with the 41 μm sediment (Figures 5.5, 5.6) is due to additional interparticle forces. Relative to experiments conducted with 10^{-4} M $NaHCO_3$, a 10^{-2}M NaCl solution resulted in a ~50% reduction in transport rate for the 41 μm sediment, and no variation for the 69 μm sediment.

Figure 5.12 shows that the transport rate of the 69 μm sediment also increased in deionized water. The Pasadena tap water used in these experiments was variable in composition, but characteristic values were pH ~8.5; ionic strength, I~1.5x10^{-2}M; specific conductance, K ~ 850 μmho/cm. Typical concentrations of the major cations were calcium (~1.5 mM), magnesium (~1 mM), and sodium (~3 mM). A greater reduction in transport is expected from the bivalent cations (Ca, Mg) than the sodium chloride electrolyte (10 mM) used for these particle sizes in the 12-meter flume. Thus, it is likely that even the 69 μm sediment was slightly cohesive in experiments with tap water.

6.2 Non-Cohesive Results

Cohesion between particles presents an additional force to be overcome by the fluid shear, resulting in lower transport rates. Thus, "non-cohesive" results are selected as the series of results that produced the greatest transport rates. For each particle size, this corresponded to the results obtained in deionized water with a nominal 10^{-4}M ionic strength. On this basis, series K, N, O, and U are identified as "non-cohesive," and plotted together in Figure 6.1. It is possible that even in these experiments, an attractive cohesive force was present, and under different water and surface chemical compositions, higher transport rates may be observed under similar shear stresses. However, the particles in these experiments (Series K, N, O, and U) are believed to be relatively cohesionless.

These four series of experimental results collapse onto a single curve, as predicted from the dimensional analysis in Section 3.1. A log-log regression to the data points resulted in the curve fit:

$$qs^* = 3.81\tau^{*2.22} \qquad (6.1)$$

This relation increases with a smaller power of τ^* than the relations found for q_s^* in tap water, in which equation (5.8) was $q_s^* = 12.4\tau^{*3.04}$. Since the experiments conducted in tap water were shown to be slightly cohesive (Figure 5.12), this difference is consistent with the observations that cohesion decreases q_s^* by a greater fraction as τ^* decreases.

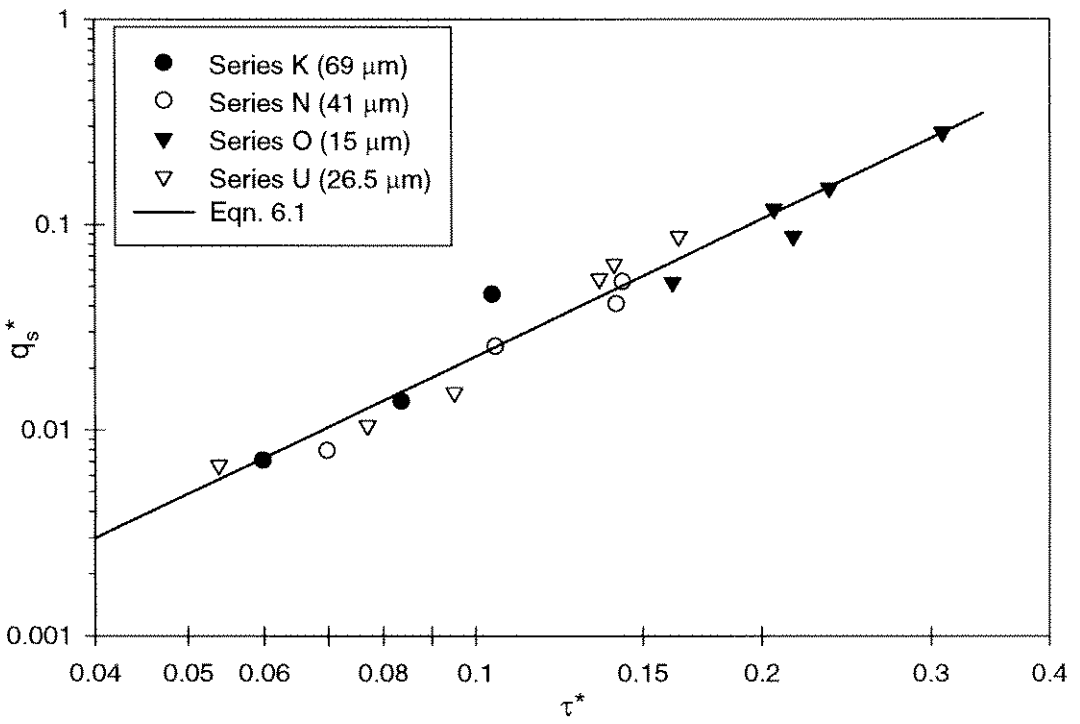

Figure 6.1: Dimensionless transport rates of non-cohesive sediments, Series K, N, O, U. The regression line to these results is also shown.

While the Shields curve theoretically represents the division between a stable and moving bed, experimentally it corresponds to a small, defined transport rate. B. Taylor (1972) suggests that the Shields curve corresponds to:

$$\frac{q_s}{u^* d_g} = 10^{-2}$$

This dimensionless group is applicable to large ($Re^* > 1$) particles. Following the physical interpretation of q_s^* (Section 3.1.3), this grouping corresponds to a layer of particles (thickness d) moving along the bed with a characteristic velocity u*. For silt-sized particle ($Re^* < 1$), the characteristic velocity is $u^{*2}d/\nu$, or $u^* Re^*$. The transition between these two dimensionless parameters should occur in the range of $1 < Re^* < \sim 5$, when the characteristic velocity changes from $u^{*2}d/\nu$ to u* as the particle protrudes from the viscous sublayer. Both parameters correspond to the fraction of the bed in motion, which is taken to be a logical description for initiation of motion. Thus $q_s^* = 10^{-2}$ is taken as the extension of Shields' curve to lower bed Reynolds numbers (Re^*), giving a critical shear stress of $\tau^* = 0.075$, independent of Re^*. These curves, along with the non-cohesive experiments, are presented in Figure 6.2. The line $\tau_c^* = 0.075$ crosses the data set at a transport rate of $q_s^* = 0.01$; higher data points correspond to higher values of q_s^*, and lower points, lower q_s^*.

Measurement of a "critical" value was not pursued in this work, because there was no way to define it except by the amount of sediment transport (q_s^*). Measurements of extremely small transport rates ($q_s^* < 10^{-4}$) were not attempted because it became obvious that small amounts of cohesion had a substantial influence on the transport rate as it approached zero. Additionally, it was recognized that colloidal iron from rust in the

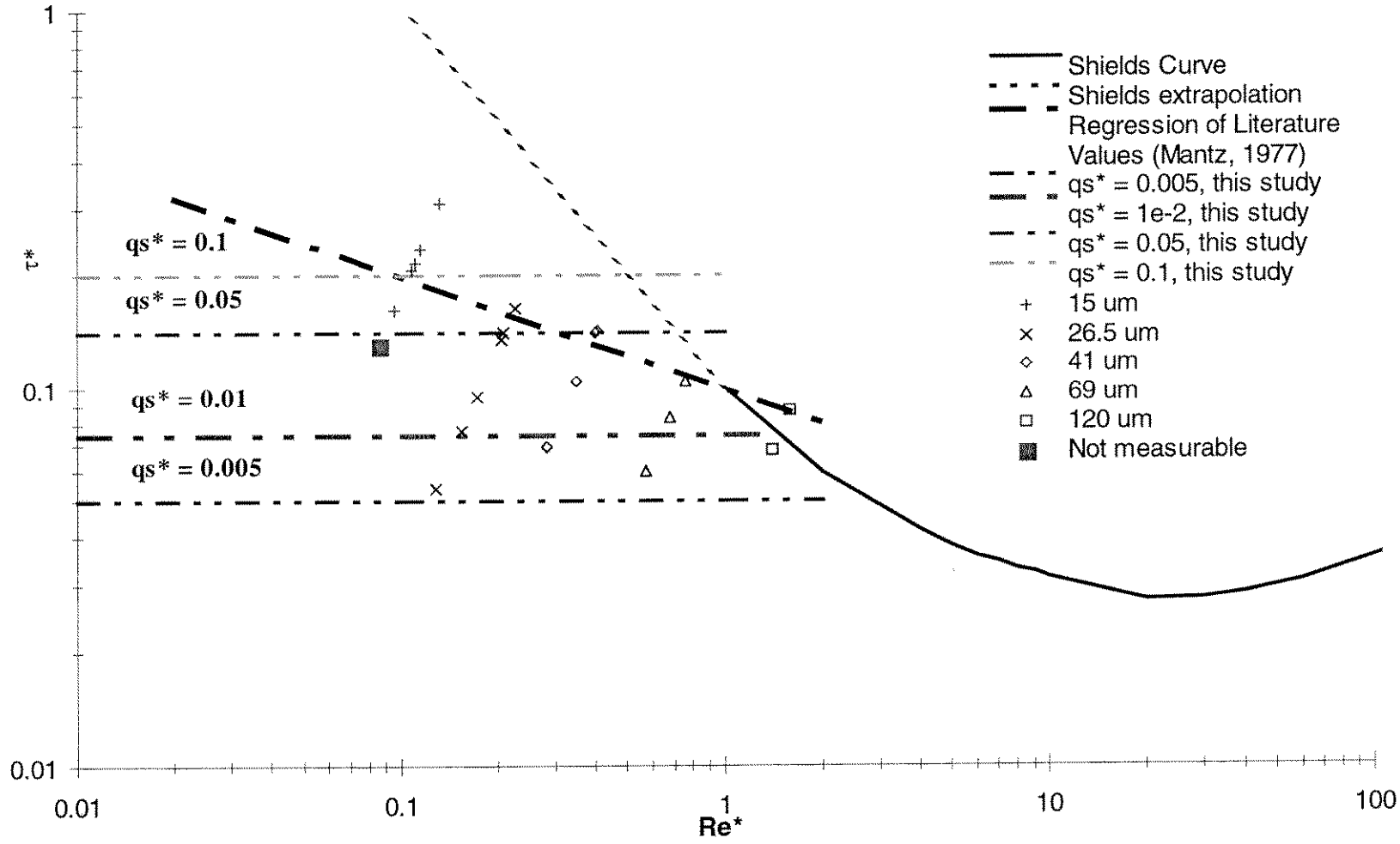

Figure 6.2: Proposed extension to Shields curve for non-cohesive sediments, corresponding to $q_s^* = 10^{-2}$. Non-cohesive experiments are shown, along with curves for constant values of q_s^*.

flumes was contributing towards stabilization of the particles. This has the greatest effect on slowly moving sediment beds.

6.3 Modeling

For non-cohesive particles, Figure 6.3 shows that the transport model (Section 3.6) does a reasonable job of predicting the dimensionless transport rate, q_s^*, given the dimensionless shear stress. The distribution of particle elevations in the model was adjusted to range from -0.56 to 0.56 (from –0.5 to 0.5) to produce better agreement with the experimental results. This adjustment indicates that the sediment bed was less stable than hypothesized. The model agreement with the data gives support to the choice of the dimensionless parameter $q_s^* = \frac{q_s \mu}{\tau d^2}$, which is different from all other formulations in the literature.

Cohesion is incorporated into the model through the dimensionless parameter $Fc^* = \frac{Fc}{\frac{\pi}{6}(\rho_s - \rho) g d^3}$. The parameter Fc* is a function of both the water/surface chemistry and particle diameter. The cohesive force (Fc) is expected to have a linear dependence on d (see Section 3.7) if it results from a combination of electrostatic, van der Waals or other surface forces. For constant water composition and surface chemistry, the parameter Fc* will become increasingly important for smaller particles, varying as d^{-2}.

All the results obtained with deionized water/NaCl for 41 μm and 69 μm particles are given in Figure 6.4, along with modeled transport rates. The parameter Fc* was

adjusted to fit each experimental series. The non-cohesive model (Fc* = 0) was used as an approximation to Series K, L, N. Fc* was increased to 0.2 to fit series J and M.

The corresponding graphs for the 26.5 and 15 μm particles are shown in Figure 6.4 and Figure 6.5, respectively. The curves are generally representative of the data, although the results indicate zero transport (or below instrument sensitivity) at higher τ* than the model predicts. The nature of the cohesion is explored further in the following section.

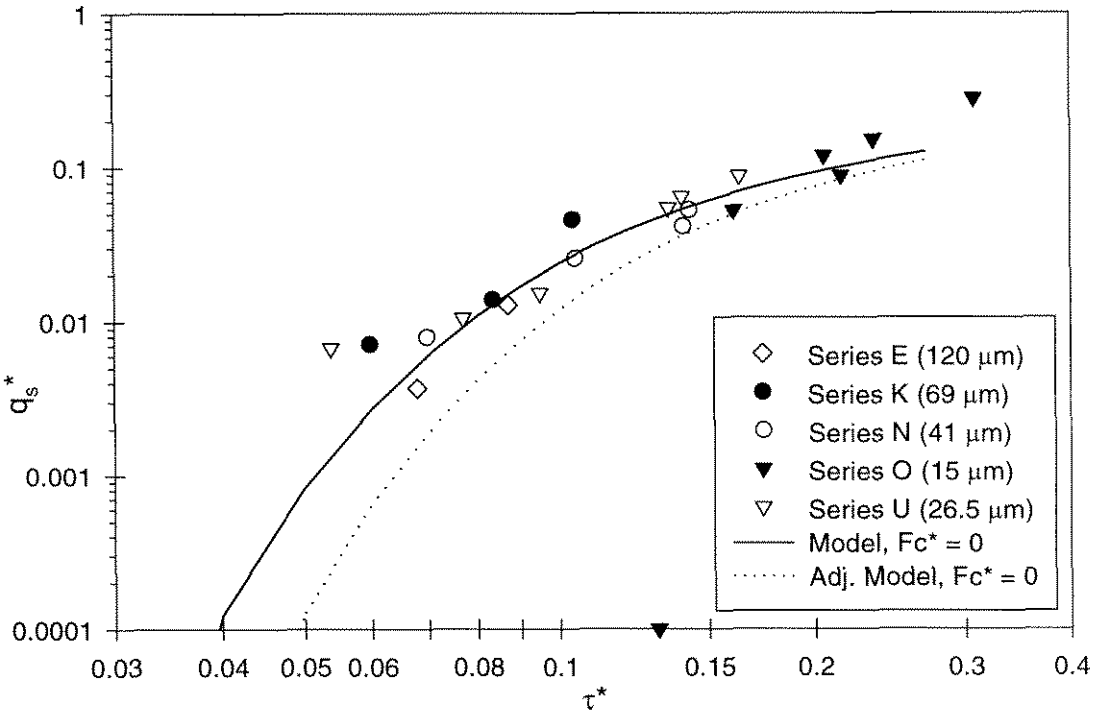

Figure 6.3: Comparison of non-cohesive experimental results with model predictions. Distribution of normalized sediment particle heights is –0.5 to 0.5 for dashed curve; adjusted model heights are –0.56 to 0.56.

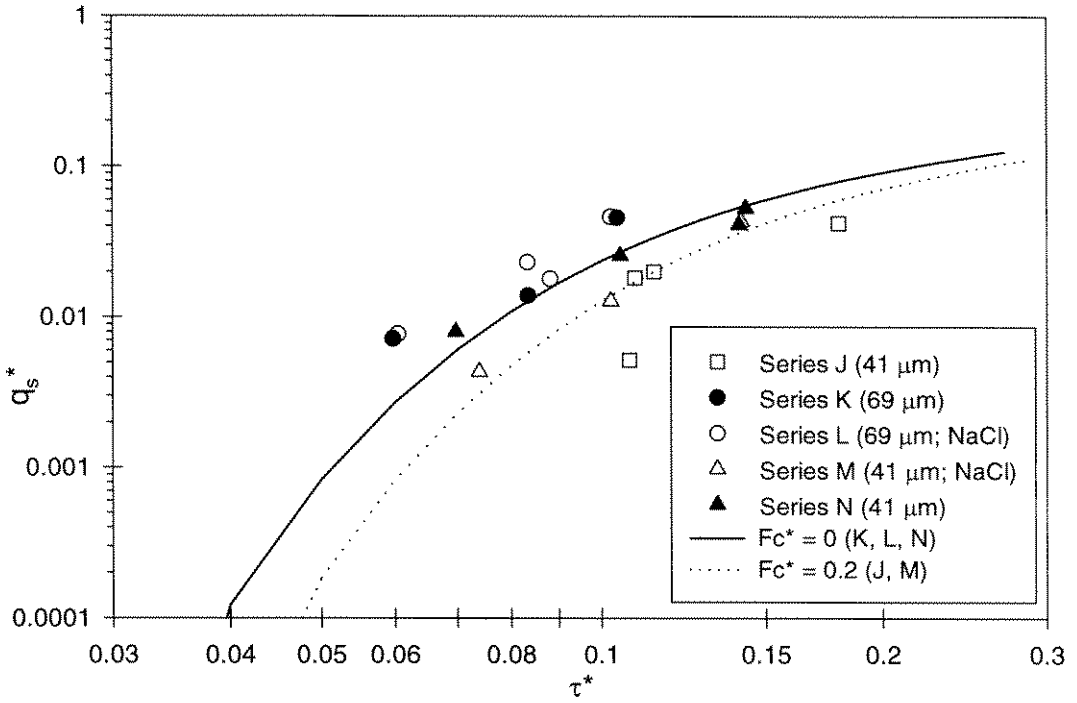

Figure 6.4: Experimental results and fitted model curves for 41 μm results (Series K, L, N – Fc* = 0; Series J, M – Fc* = 0.2) with and without cohesive forces (Fc*).

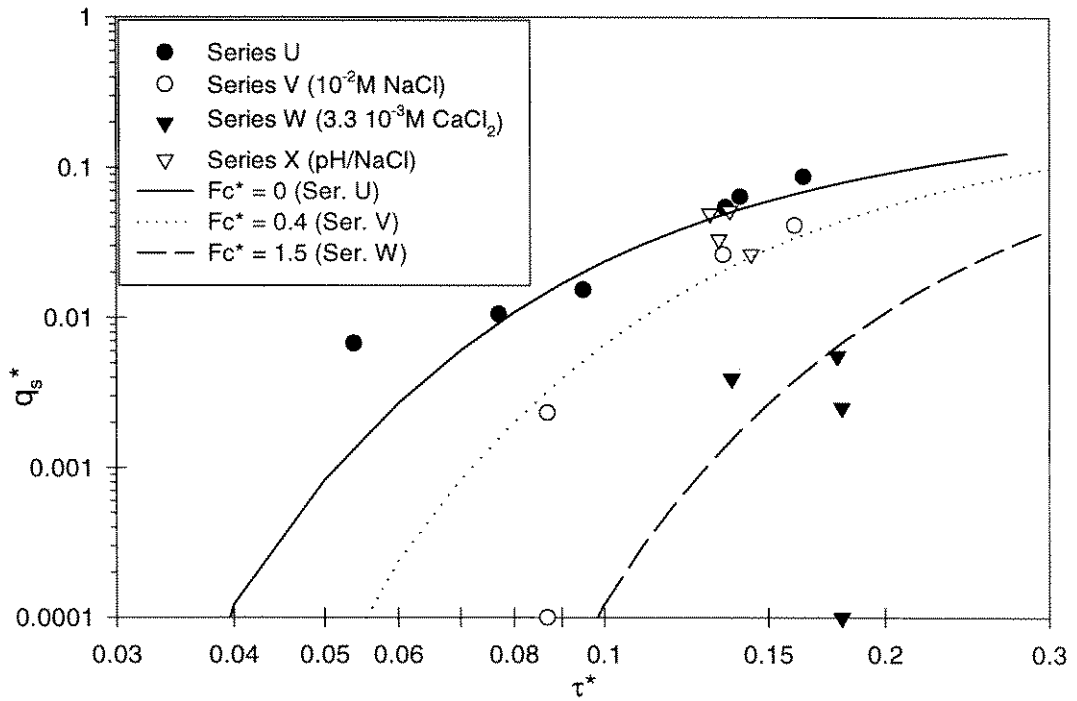

Figure 6.5: Experimental results and fitted model curves for 26.5 μm results (Series U, Fc* = 0; V, Fc* = 0.4, W, Fc* = 1.5; X, not modeled).

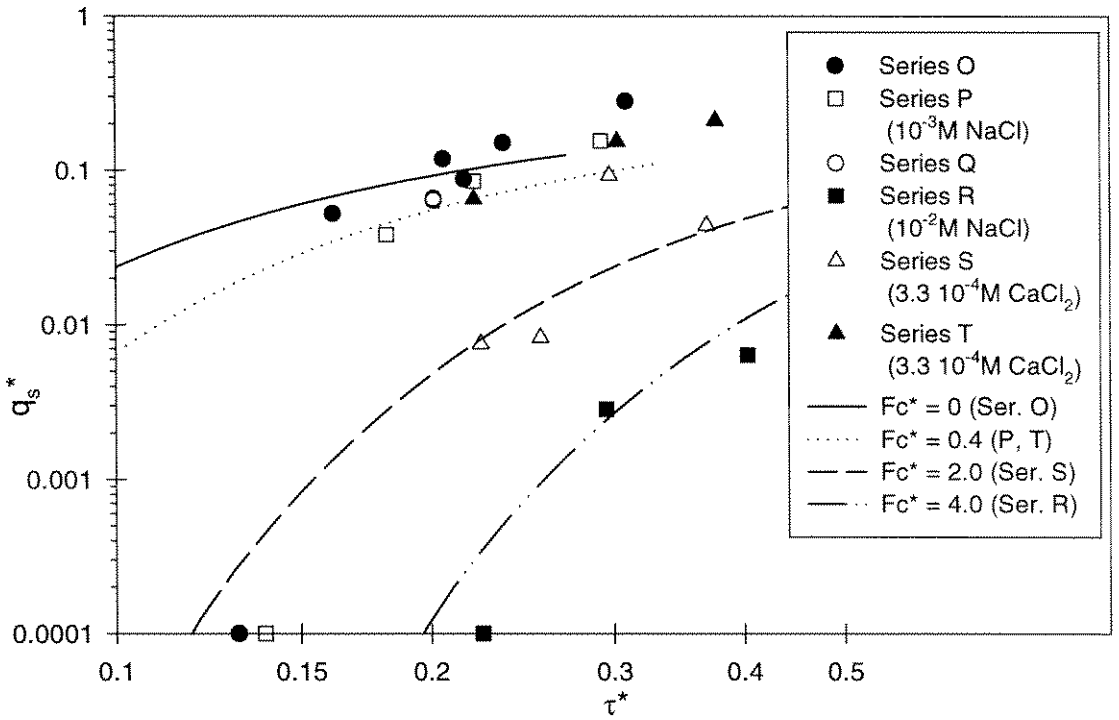

Figure 6.6: Experimental results and fitted model curves for 15 μm results (Series O and Q, Fc* = 0; P and T Fc* = 0.4 to 0.6; R, Fc* = 4.0; S, Fc* = 2.0).

6.4 Cohesion

The reduction in sediment transport rate under similar flow conditions is attributed to a cohesive (attractive) force between the particles. The decrease in transport rate (increase in cohesion) is in qualitative agreement with theory and observation in other systems, such as the coagulation of colloidal particles or behaviour of clay particles. Cohesion increases with salt concentration, in which calcium (bivalent ion) is more effective than sodium (monovalent ion), at equal ionic strength (Figure 6.6).

Under similar chemical conditions, the dimensionless transport rates decrease with particle size. Experiments were run for all particle sizes in water containing 10^{-2}M

NaCl, which provided some cohesion for the smaller particle sizes. Table 6.1 summarizes the values of Fc* that were fit to each of these four series of experiments (L, M, V, R). The third column of the table gives the relative ratio of Fc* to that for the 41 μm particles. Fc* was expected to scale as the minus two power of the diameter (see Section 3.8). The relative ratios based on this assumption are given in column four. Comparison of columns three and four indicates that the experimental results fall both above and below the predicted values.

Particle Diameter (μm), Series	Fc* (fit from results)	Fc*/Fc*(41μm)	$Fc^* = \frac{\text{const} \cdot d}{(\rho_s - \rho) g d^3}$
69, Series L	0	0	0.35
41, Series M	0.2	1	1
26.5, Series V	0.4	2.0	2.4
15, Series R	4.0	20	7.5

Table 6.1: Values of Fc* obtained by adjusting the model to fit experiments with 10^{-2} M NaCl and predicted dependence on diameter.

The Fc* value for the 15 μm may be overestimated, as it is uncertain if an constant transport rate was reached before the end of the test patch in these experiments. The transport rates for the 15 μm sediment were so low that the measurement of transport rate against distance was dominated by the uncertainty in the drift correction. Thus it was impossible to verify that a transport rate independent of distance had been achieved. The sediment transport rate for all other particle sizes was sufficient to observe a constant transport rate.

Results and description of the surface chemistry modeling is provided in Appendix A. Direct application of the results to modeling the present system is difficult because of the numerous variables (e.g., particle history, colloidal iron in the flume) that could not be completely controlled or quantified. However, the model provides qualitative support for the trends observed in the experiments. The diffuse layer potential computed for a silica surface under different electrolyte concentrations are summarized in Table 6.2. A larger diffuse potential implies a greater electrostatic repulsive force between particles, and thus less cohesion. Depending on the equilibrium constants chosen, the model also predicts calcium to adsorb strongly to the surface, in agreement with the observed increase in cohesion for $CaCl_2$ solution over NaCl at the same ionic strength. The range of potential for $CaCl_2$ corresponds to the different equilibrium constants obtained from the literature.

Electrolyte	Diffuse layer potential (Ψ_d)
1e-4 M NaHCO3	-78 mV
1e-3 M NaCl	-68 mV
1e-2 M NaCl	-38 mV
3.3e-4 M CaCl2	-54 mV to –1 mV
3.3e-3 M CaCl2	-24 mV to +12 mV

Table 6.2: Diffuse layer potential calculated for silica surfaces in varying electrolytes (triple layer model). See Appendix A for details.

While the attractive force of the secondary minima, described in Section 3.8, does not predict the magnitude of the cohesive forces observed, the cohesive force should

scale proportionate to the particle diameter, and Fc* would vary as d^{-2}. Relating this information back to Shields' curve, the dimensionless shear stress can be computed for a constant solution chemistry and constant dimensionless transport rate. The 'threshold' condition corresponding to different chemical environments, is plotted on Shields' curve (Figure 6.7) for two cases.

The threshold curves correspond to constant q_s*, and chemical conditions. Adding the cohesive force to the particle's weight in the definition of τ* the threshold condition becomes:

$$\frac{\tau d^2}{(\rho_s - \rho) g d^3 + Fc} = \frac{\tau}{(\rho_s - \rho) g d \left[1 + \frac{\Phi d}{(\rho_s - \rho) g d^3} \right]}$$

$$= \frac{\tau^*}{\left[1 + \frac{\Phi}{(\rho_s - \rho) g d^2} \right]}$$

Where Fc = Φd, Φ is the interaction potential (energy), and the geometrical coefficients of order (1) have been combined into Φ. For non-cohesive materials, constant τ* implies the ratio of drag force to resisting force (gravity) is constant. Here the resisting force is the sum of gravitation and cohesive forces, so:

$$\tau^* = \tau^*_{NC} \left[1 + \frac{A^*}{(\rho_s - \rho) g d^2} \right] \qquad (6.2)$$

where τ^*_{NC} is the constant critical shear stress observed under non-cohesive conditions.

Experimentally, there were several processes that affected the cohesion of the glass beads. These are difficult to quantify, but are briefly described here. More detail is given in Appendix A.

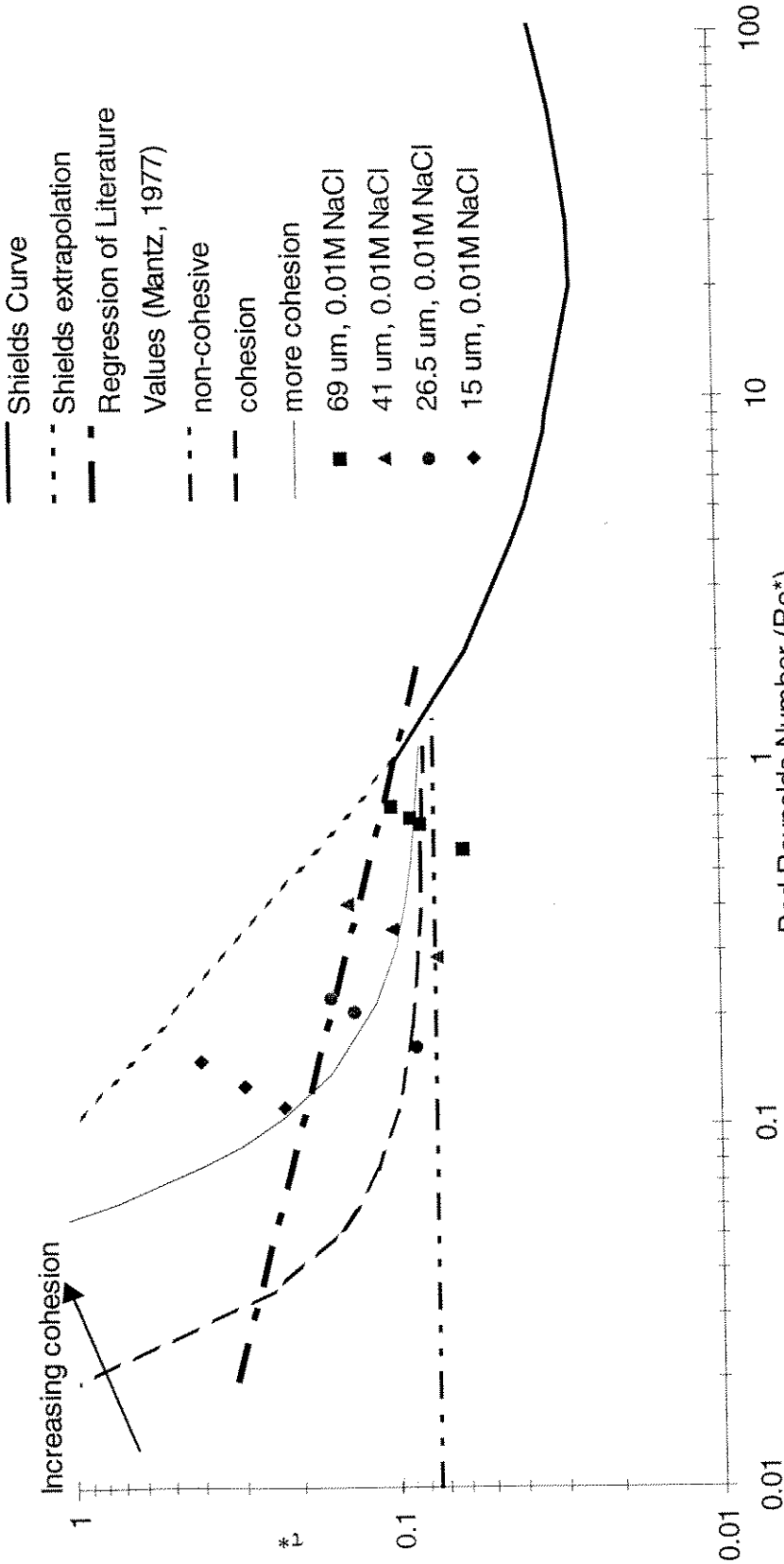

Figure 6.7: Proposed threshold relationship for cohesive materials. Experiments conducted in 0.01M NaCl solution are also shown.

Upon immersion in water, the Na^+ ions begin to diffuse out of the glass matrix, and are replaced with hydronium (H_3O^+) ions from solution. Doremus (1994) indicates that the depletion of sodium from the surface layer proceeds as a diffusion process until it reaches a depth of 0.5 – 0.6 μm, which occured after 540 hours at 90°C. This process suggests a possible explanation for the aging effect that was observed with series (H) and other particles. The porous glass surface may allow cations (H^+ in particular) to diffuse into the glass, reducing the charge (and the repulsive force) on the particle's surface.

Alternatively, this silica matrix structure may promote conversion of silica into a polymeric chain, which has been suggested as the start of a sintering process. (Vigil, 1994).

The thicker double layer at low ionic strengths means that the electrostatic repulsion between particles occurs at larger separations, increasing the repulsion between particles. In addition, fewer ions are adsorped to the surface, resulting in a larger diffuse potential and increased repulsion. This all suggests that relatively less cohesion will be present at low ionic stengths.

Colloidal iron oxide-hydroxide was produced in the flume as the iron components (piping, side-walls) rusted. Some of this iron oxide was captured on the polyester air filter in the flume, and is visible under a microscope as colloidal particles attached to the filter. It is likely that these colloidal particles also attached to the glass beads, creating a small positively charged patch to bind with a neighbouring silica particle.

In addition, the particles were obtained with contamination with iron. The cleaning procedure (Section 4.3) was developed to remove this contamination. However, this process was stopped when the iron concentration reached 5-15 μM. This

would still correspond to a surface coverage of 0.5 to 1% of the surface sites. At this point, further washings did not result in a continuing improvement of the amount of iron released. Additionally, it seemed futile to work for lower Fe concentrations, given the presence of rust in the flumes.

6.5 Comparison with Other Results

As mentioned in Sections 2.2 and 2.3, G. Unsold (1984) measured sediment transport of silt-sized quartz particles. In his experiments, the particles were captured downstream of a test section against a horizontal bar that protruded from the flume bottom. The sediment accumulated against this bar was collected and weighed to determine the sediment transport. He observed that the quartz silt became obviously cohesive for particle sizes below 15 μm. The measured transport rates were expressed in dimensionless terms with the parameters q_b^*, τ^*, and Re^*, where $q_b^* = q_s/u^*d_g$. The experimental results produced individual transport curves of q_b^* vs. τ^* for each sediment size, but did not collapse onto a single curve, as shown in Figure 2.4.

His data is re-expressed in Figure 6.8 in terms of the dimensionless parameters (q_s^*, τ^*) presented in this work (assuming a porosity of 0.4). The resulting dimensionless transport rate curves are still slightly dependent on particle size, but less so than in Unsold's variables. Chemical interactions were likely important in his experimental system. However, no information was given about the preparation of the sediment, or of the chemical composition of the water. It is also apparent that his measured sediment transport rates (q_s) depend on a higher power of τ^* than the results presented here.

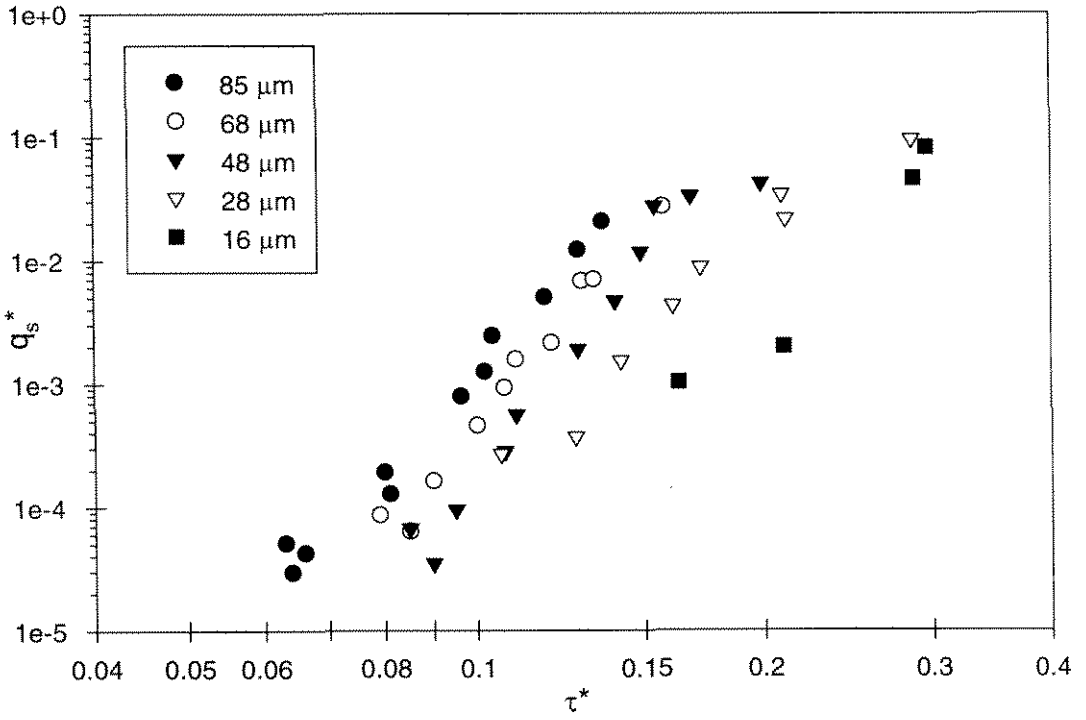

Figure 6.8: Results of Unsold (1984) replotted using q_s^* and τ^*. The original scaling is shown in Figure 2.5.

The particles used in this study were of similar size to Unsold's study, facilitating direct comparison between the results. The results for similar sized particles are plotted in Figure 6.9 (68/69 μm), Figure 6.10 (48/41 μm), Figure 6.11 (28/26.5 μm), and Figure 6.12 (16/15 μm sediments). Comparison between each particle size reveals that, for the same τ^*, Unsold measured lower transport rates than observed in this study.

Experimentally, Unsold collected the material transported off his sediment bed (50 cm long by 29.4 cm wide) in a bedload trap, and weighed the total mass of material after each experiment. This method is advantageous for very small transport rates because a wide sediment bed may be used to increase the amount of material collected.

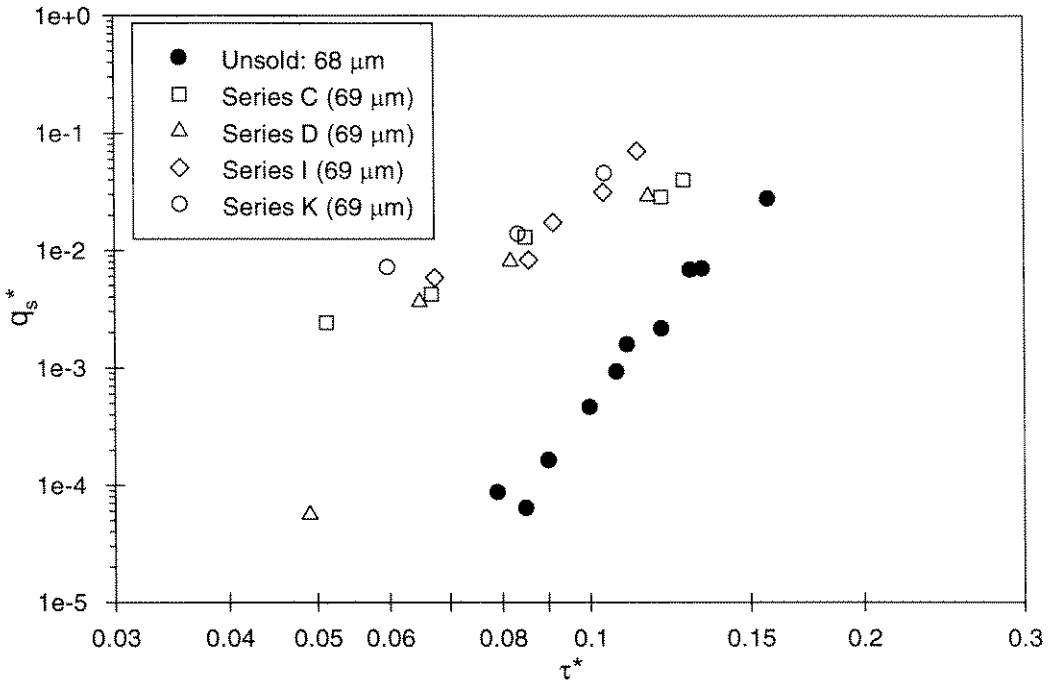

Figure 6.9: Comparison of experimental results from Unsold (1984) (68 μm), and this study (69 μm).

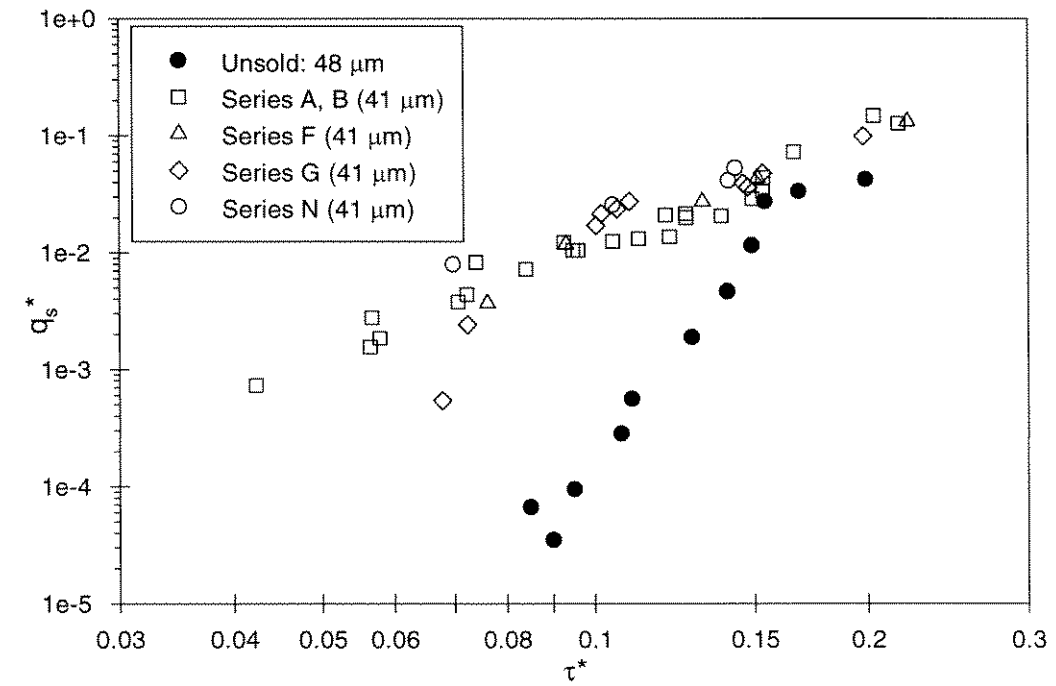

Figure 6.10: Comparison of experimental results from Unsold (1984) (48 μm), and this study (41 μm).

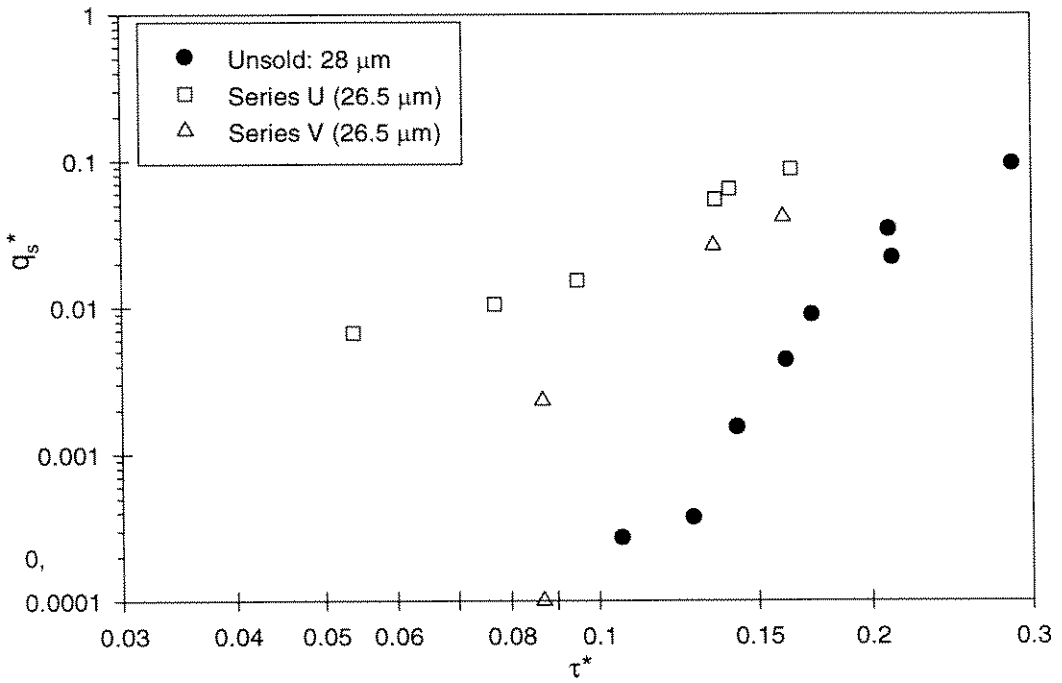

Figure 6.11: Comparison of experimental results from Unsold (1984) (28 μm), and this study (26.5 μm).

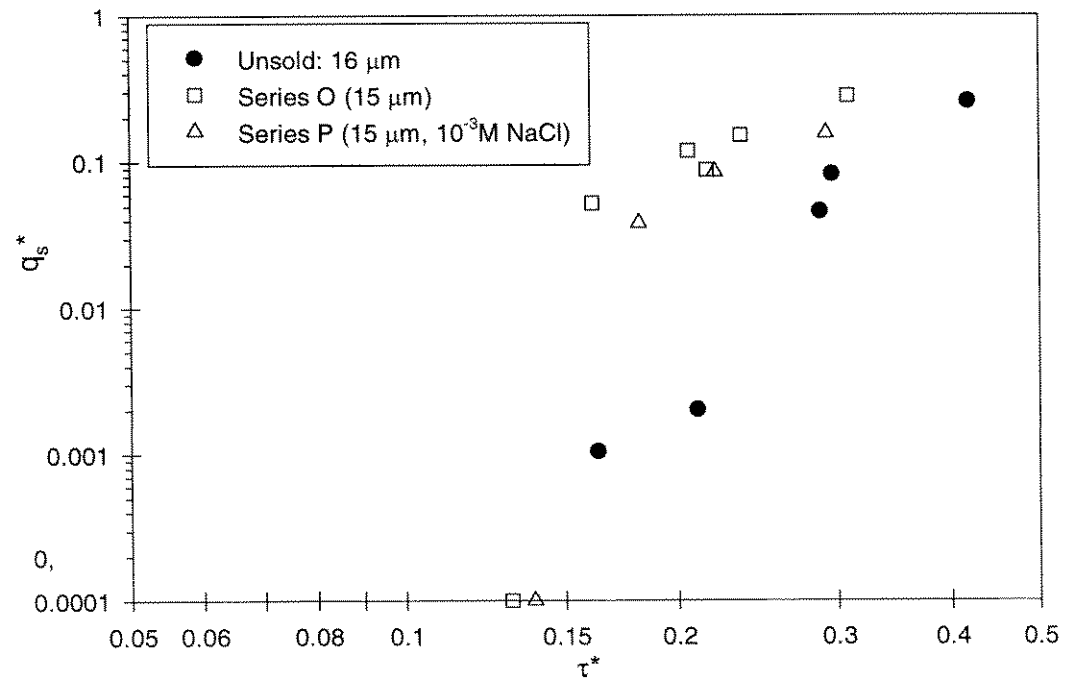

Figure 6.12: Comparison of experimental results from Unsold (1984) (16 μm), and this study (15 μm).

However, this method appears problematic, as the sediment particles that moved off the sediment bed in the present study accumulated immediately downstream, making the separation of where the sediment bed ended difficult to determine. Additionally, Unsold's method only collects particles transported off the test section as bed load, and thus underpredicts the total sediment transport by the amount of material moved as suspended load. It is possible that particles in Unsold's experiments may have escaped the bedload trap, but given the observations of the present experiments, this seems unlikely.

The difference between the two studies may be a result of the nature of the sediment used. Unsold used a crushed, angular crystalline quartz, whereas spherical glass beads were used in this experiment. As mentioned in Section 3.6, Miller and Bryne (1966) measured the angle (ϕ) at which particles of different shapes will move off a fixed bed. ϕ was reported to be about 50° for spheres, 60° for natural materials, and 70° for angular material. This angle corresponds to the distribution of particle heights (δ) assumed in the transport model. Specifically,

$$\cos\phi = \frac{\delta_{max}}{\sqrt{3}/2}$$

where $\frac{\sqrt{3}}{2}$ is the projection of the particle's radius onto the X direction from assuming the particle rolls over the gap between two adjacent particles. Thus for the distribution assumed in Section 3.7, δ_{max} is 0.5, corresponding to a contact angle of 55°. If this angle is increased, to correspond to more angular materials, δ_{max} decreases. The non-cohesive sediment transport rate corresponding to a contact angle of 63° is shown in Figure 6.13, and demonstrates reasonable agreement with Unsold's results for 85 μm sediment

(assumed to be non-cohesive). Thus it is believed that the primary difference between the two studies, for non-cohesive material, is the angularity of the particles.

As the sediment particle size decreases, Unsold's results require an increasing τ^* for the same dimensionless transport rate. Since no mention was made in Unsold's report of any chemical parameters, it is assumed that some cohesion was present in his system, so as the particle diameter decreases, the cohesion requires a higher shear stress for a given transport rate.

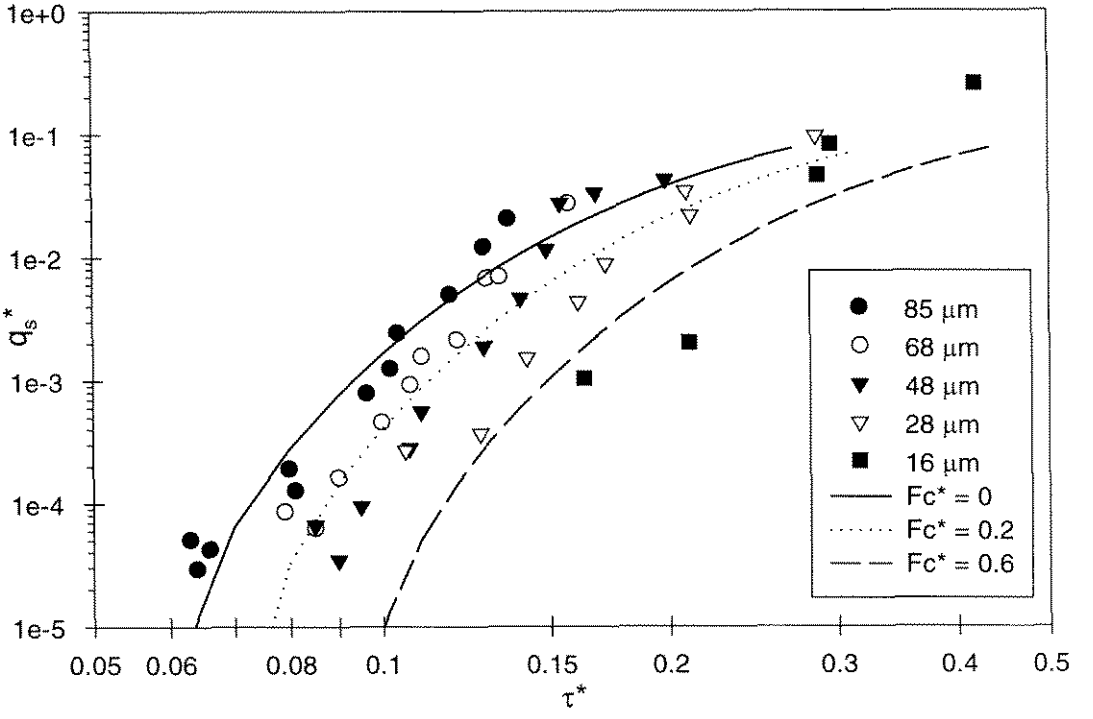

Figure 6.13: Experimental results of G. Unsold (1984), and model predictions. Transport rates are made dimensionless using q_s^* as defined in this work. Model curves stop at limit of model approximations.

6.6 Experimental Technique

Calculation of the sediment transport rate from a series of bed profiles proved to be a highly accurate and reliable method. The most significant sources of uncertainty are believed to be natural variations in the evolution of bedforms and three-dimensional sediment transport.

6.6.1 Laser Displacement Meter

The LB-081/1101 laser displacement meter proved to be an extremely effective instrument to measure sediment transport. It provided a non-intrusive, accurate, and repeatable measurement technique to record the changing sediment bed elevation in time. Data collection was easily automated, allowing sequential profiles to be taken over short time intervals (10 minutes), and facilitating long-term (12-24 hours) experiments. Relative to the natural variability in sediment transport, and the slight three-dimensional nature of the sediment transport, the laser displacement meter contributed trivial error except at extremely low transport rates. For a typical 4 hour period, the mean rate of bed decrease was accurate to 0.2 μm/h, with a 95% level of confidence. This corresponds to an uncertainty of 0.08 mm^2/hr in the measured sediment transport rate.

The LB-1101 laser displacement meter occasionally exhibited a slow drift in time, which was corrected for by measuring the elevation of the upstream surface of the test tray. Temperature fluctuations were the primary cause of this drift, which was particularly noticeable after the displacement meter was turned on. Otherwise, the random variation in each measurement had a standard deviation of about 5 μm. The

primary effect of this variation was to create uncertainty in the measurement of the reference elevation of the upstream edge of the test tray.

The standard deviation of the mean test plate elevation was approximately 1 μm, from the average of this random noise over the measurements made on the upstream surface of the test tray (56 for Series A-C, 20-24 for Series D-X). For experiments recording low transport rates, this was the greatest source of error. A longer averaging time, or more measurements, would slightly improve the accuracy of this correction for instrumental drift.

This random uncertainty of the displacement meter also corresponds to an expected standard deviation of 0.35 μm in the mean bed height (for 200 measurement locations). An apparent increase or decrease of the mean bed elevation, due to these uncertainties, would appear as a linear increase or decrease of the transport rate with distance. A 1 μm elevation change corresponds to:

$$\frac{\partial q_s}{\partial t} = \frac{0.001 mm}{\Delta t}$$

For the 10-minute time intervals typically used with the 40-cm sediment bed, this corresponds to an uncertainty of 0.006 mm/hr, or 2.4 mm^2/hr for the entire length of the sediment bed. This was reduced by computing the transport rate between non-sequential transects (i.e., every sixth transect). Increased time intervals result in the spatial variations of transport over each bedform appearing smoothed out as the bedforms propagate downstream.

The accuracy of the elevation measurement could also be improved by utilizing a more accurate laser displacement meter. The LB-081/1101 was chosen for this study because its long working distance (10 cm) allowed large Reynolds number flows (10-40

cm water depths) to be obtained with minimal disturbance of the flow near the sediment bed. Keyence Corp. produces other models of laser displacement meters that have sub-micron accuracy with a working distance of 2-4 centimeters.

Experiments measuring high transport rates are constrained by the time required for the laser probe to complete a measurement transect of the test bed. If the sediment movement is too great, the measured bed elevation is no longer a good approximation to the instantaneous bed elevation. In an attempt to minimize this problem, the mean bed elevations were computed from transects moving in both the upstream and downstream directions. The importance of this error increases as the measurement time and sediment transport rate increase. Thus, the sediment transport rates measured for Series E are relatively uncertain, as rapid sediment transport and ripple growth occurred in both experiments.

The LB-1101 displacement meter operates by triangulating the location of the reflected laser beam. The beam is a rectangle 1 mm x 2 mm. In the configuration used, the 1 mm dimension corresponded to the streamwise width. This provided a reasonable point measurement compared to the ripple wavelengths that developed. According to the manufacturer's specifications, this displacement meter is insensitive to the relative angle of the surface. The instrument's sensitivity varies by 1% between surfaces positioned at –30° to +30°. This was not considered to be a significant source of error in these experiments.

6.6.2 Shear Stress Measurements

The sediment transport rate is highly sensitive to the fluid shear stress, thus an accurate value of the shear is required to minimize error and facilitate comparison with

other studies. In this work, the fluid shear stress was calculated by assuming a smooth boundary and applying Blasius's equation

$$f = \mathrm{Re}_{Dh}^{-1/4} \tag{4.4}$$

to obtain the friction factor. The fluid shear is then computed from the relation:

$$\tau = \frac{f}{8}\rho U^2$$

The Reynolds number used in this computation was based on the hydraulic diameter (four times the hydraulic radius) of the flow, in place of the pipe diameter. The advantage of this method was that the required variables (flow depth, flow rate) are easily and accurately measured, insuring little relative error (<2%) between experiments.

The accuracy of this method was verified at two flow rates by measuring the velocity profile and Reynolds stresses with a commercial (TSI) LDV system. The two methods agreed to within 6% of each other (Section 4.5). However, the Reynolds stress profiles were not linear to the free surface as expected for an infinitely wide channel. This is believed to be a result of the small width/depth ratio (~2.5) of the flow, in which ~40% of the total shear force is taken by the side walls.

It was not feasible to determine the shear stress directly from the force balance equation, $\tau = \rho g R_h S$, as the slope (S) of the water's surface (energy grade line) was too small (10^{-5} to 10^{-4}) to measure accurately.

Based on the measurement uncertainties, and the LDV measurements, the shear stress values reported appear to be accurate to within +/- 5%. This implies an uncertainty of +/- 5% in the dimensionless shear stress (τ^*) and dimensionless transport rate (q_s^*) parameters.

6.6.3 Sediment Bed Preparation

Significant effort was placed into separating the glass beads into reasonably uniform size distributions. This is reflected in the geometric standard deviation, σ_g = 1.28-1.30, of the particles used in these experiments (Chapter 4.2). Even such a narrow distribution has almost a factor of 3 difference between the settling velocity of particles whose diameter is a factor of σ_g above and below the geometric mean diameter. Because the sediment bed was prepared by creating a uniform suspension and allowing this to settle into the test tray, the upper layer of sediment will be enriched in smaller sized particles. Thus the effective diameter in the experiments may be smaller than assumed, and the resulting dimensionless shear stress (τ^*) and transport rate (q_s^*) parameters larger.

The process of creating the sediment bed by settling not only mimics natural processes, but made an extremely flat and reproducible bed surface. Use of an electric propeller-style mixer in suspending the particles within the settling column produced a much smoother bed than originally obtained when mixed by hand.

6.7 Further Experimental Observations

6.7.1 Initial Transient Behaviour

For most experiments q_s* was constant in time and position after the initial scour region. In some experiments the sediment transport rate was observed to increase with position (dq_s/dx) during an initial period. The transport rate decreased in time to become independent of time and distance. This was primarily observed with the 15 and 26.5 μm

particles, as indicated in the list (Table 6.3) of experiments in which this occurred. This phenomenon was difficult to observe in the initial experiments with the 41 and 69 μm particles due to its short duration (less than 10 minutes). This initial transient was observed over the first time interval in experiment J-1, as shown in Figure 6.14. Notice that a constant transport rate is reached after 10 minutes in this case. A longer decay period of this transient erosion was observed in experiments with smaller particles, as listed in Table 6.3. The initial rate of dq_s/dx is also listed, along with the rate of increase of q_s^*. One of the longest transients observed (6 hours) is shown in Figure 6.15 as two hour averages of the transport rate for 26.5 μm sediment in experiment U-4. The average transport rate (Equation 5.7) corresponds to the preceding interval, so T=2 hours is the average transport between T = 0 and T = 2 hours, and so on.

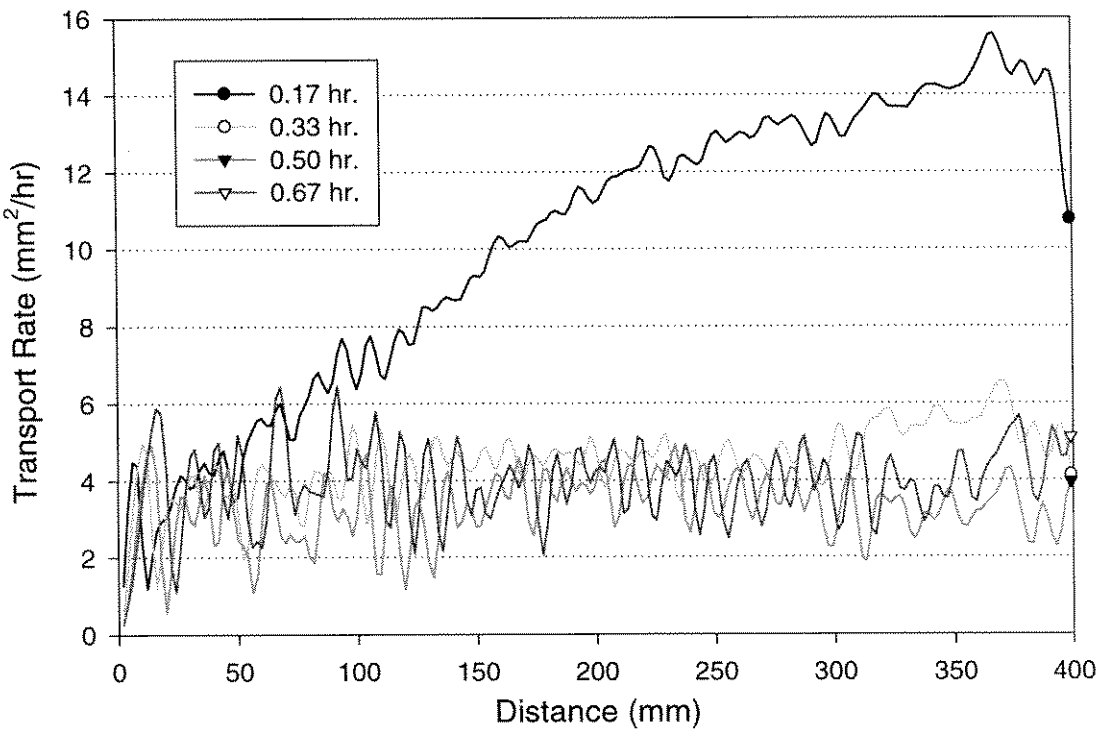

Figure 6.14: Sediment transport rate vs. distance for Experiment J-1 (41 μm) showing the initial transient behaviour (T < 1/6 hour). The curves are labeled with the elapsed time, in hours.

Expt. No.	τ^*	q_s^*	dq_s/dx mm/hr	Transient Period (hr)	dq_s^*/dx (1/mm)
15 μm					
O-1	0.21	0.119	0.01	2.00	0.92
O-2	0.31	0.280	0.04	1.50	3.68
O-3	0.13	0.000	0.004	4.00	0.37
O-4	0.16	0.052	0.005	6.00	0.46
O-5	0.22	0.088	0.01	2.00	0.92
P-1	0.22	0.085	0.005	1.00	0.46
P-3	0.29	0.155	0.016	3.00	1.47
Q-1	0.20	0.066	0.005	2.00	0.46
O-6	0.23	0.151	0.015	1.30	1.38
T-3	0.22	0.065	0.0074	2.00	0.68
Q-2	0.20	0.064	0.0067	0.67	0.62
26.5 μm					
U-1	0.13	0.054	0.0133	2.00	0.34
U-2	0.09	0.015	0.006	4-6	0.15
U-3	0.16	0.088	0.0267	1.00	0.68
U-4	0.08	0.010	0.0033	6.00	0.08
V-1	0.13	0.026	0.0133	1.00	0.34
U-6	0.14	0.064	0.01	1.00	0.25
X-3	0.14	0.027	0.01	1.00	0.25
X-4	0.13	0.033	0.018	0.33	0.46
41 μm					
J-1	0.11	0.005	0.04	0.17	0.35
69 μm					
K-1	0.08	0.014	0.025	0.17	0.22

dq_s/dx: rate of increase of the transport rate along the bed, or the erosion rate $\dot{E}$, in mm/hr. This value was estimated from the slope of q_s vs. x for the first time interval of the experiment.

Transient Period: the time elapsed before dq_s/dx ~0 along the downstream third of the test patch.

dq_s^*/dx: the rate of increase of q_s^* (mm^{-1}) $\frac{dq_s^*}{dx} = \frac{\mu}{\tau d^2}\frac{dq_s}{dx}$

Table 6.3: Rate of increase in sediment transport with distance. Only experiments conducted in the 12-meter flume that had an initial transient are listed.

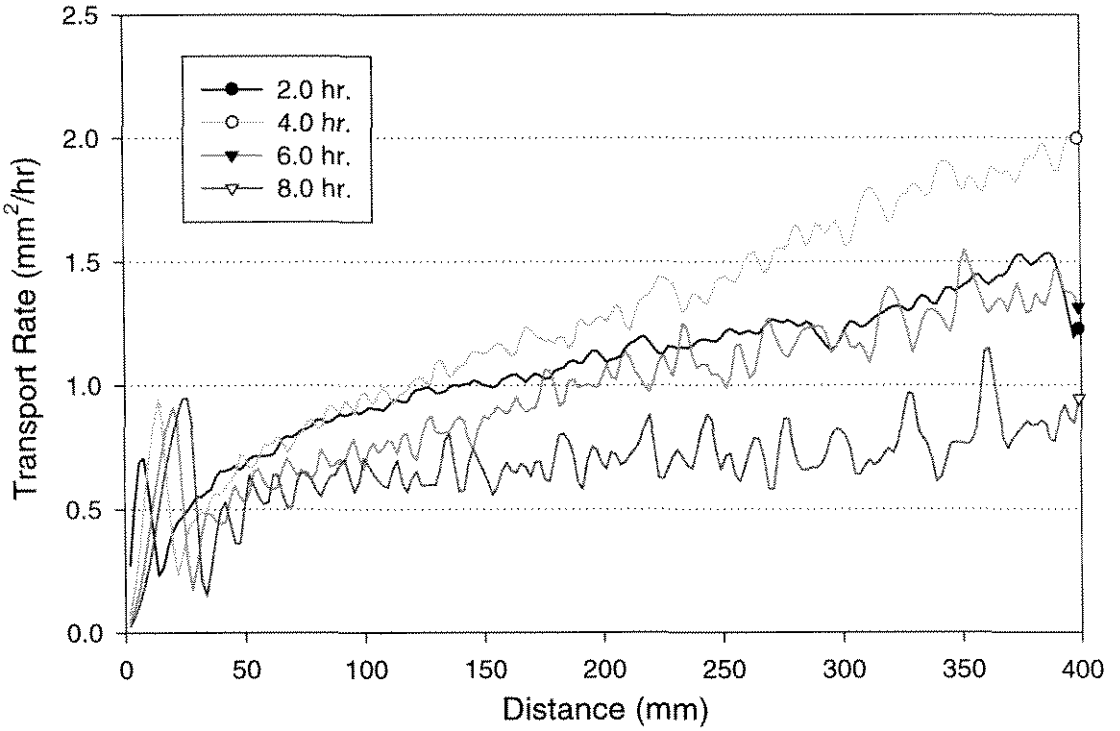

Figure 6.15: Sediment transport rate vs. distance for Experiment U-4 (26.5 mm) illustrating the initial transient behaviour (T<6 hours). Transport rate curves are the average transport for the preceding two hours.

The initial transient measured in experiment O-5 (15 μm) is shown in Figure 6.16. In this case, the transient disappears within two hours, and the transport rate becomes independent of position, except for the effect of bedforms. The transport rates reported in Chapter 5 correspond to the transport rate that existed after this initial transient had disappeared.

There was no indication that material was being directly suspended. On the contrary, a bedform was observed to form immediately downstream of the sediment bed. Additionally, if resuspension directly into the mean flow was occurring, no reason is evident as to why it should decrease in time. It is thought that this transient transport may be due to the initial surface layer containing particles that are smaller and less compacted.

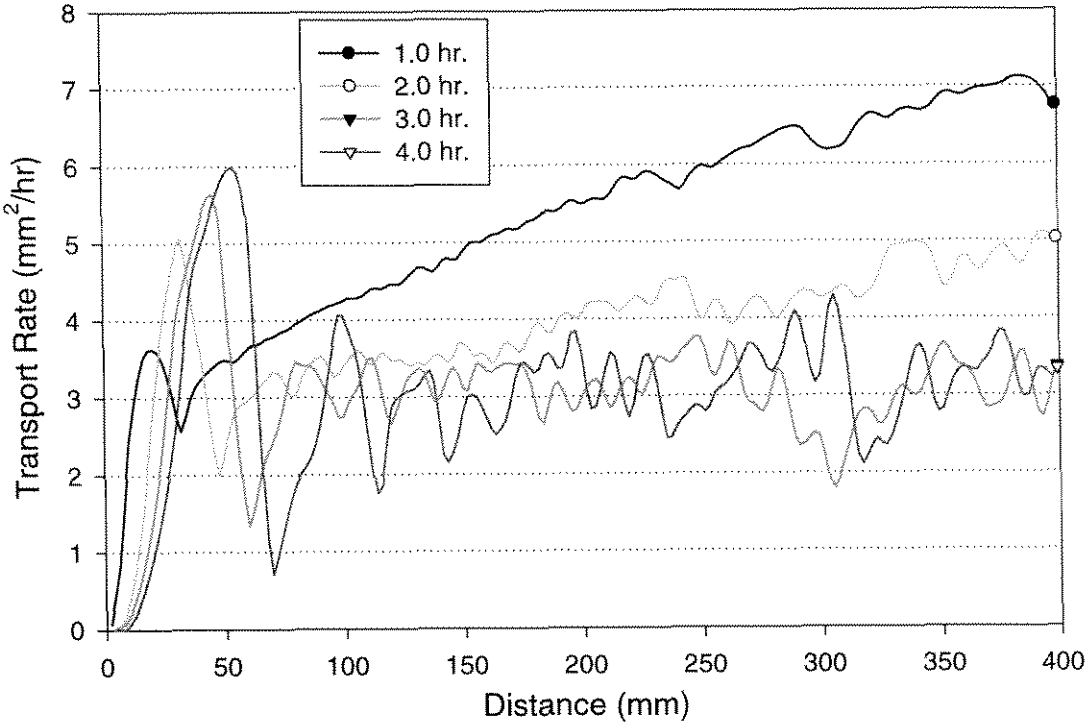

Figure 6.16: Sediment transport rate vs. distance for Experiment O-5 (15 μm) depicting the initial transient behaviour (T<2hours). The curves are labeled with the elapsed time, in hours.

6.7.2 Effect of Bedforms

The appropriateness of the dimensional analysis identifying q_s^* and τ^* as the appropriate parameters rests on the assumption that the material is transported as bed load, and is not directly suspended into the mean flow. This assumption is supported by the model of the turbulent fluctuations in the viscous sublayer, and previous experimental work with particles on solid beds.

All of these neglect the presence of bedforms. Ripples are seen to form in all non-cohesive experiments, and also in many experiments that possessed some cohesion. It is possible that flow over a rippled sediment bed could entrain particles into the mean flow. With sand-sized particles, such entrainment is observed at the crest of dunes. In

the plots of transport rate vs. distance, such entrainment would appear as a continual increase in the sediment transport rate with distance. The sediment bed is sufficiently small that any material ejected into the mean flow would be carried far downstream of the test section.

Considering only the experiments conducted in the 12-meter flume, those experiments in which sizeable bedforms (> 0.5 mm) developed are listed in Table 6.4. In these experiments, the transport rate was observed to increase after a certain time. It then appeared to remain constant at its new value. The experiments in which this increase was observed are all experiments with large transport rates, primarily because experiments with smaller transport rates were stopped before the bedforms developed to this extent. The bedform amplitude in Table 6.4 is the trough to crest distance, estimated from the bed profile at the time the transport rate began to increase. The initial scour bedform was not included in estimating the ripple heights, which were typically 0.6 to 0.8 mm. Normalization with the viscous wall unit (ν/u^*) results in a dimensionless ripple height H^* of 7-10. Thus, the ripple heights were on the same order of magnitude as the thickness of the viscous sublayer (~ 11.6), and are very small compared to the usual ripples or dunes (typically a few centimeters in height) observed in sand beds in laboratory flumes.

The effect of bedform growth is illustrated in Figure 6.17(a) and Figure 6.18(a), which show the mean sediment transport rate remaining constant in x, but increasing in time for experiments K-3 (69 μm) and N-2 (41 μm). The corresponding bed profiles are shown in Figure 6.17(b) and Figure 6.18(b), respectively. Averaged over the downstream half of the sediment bed, no substantial entrainment (dq_s/dx) (compared with overall

transport rates, and variation over a bedform wavelength) was observed to result from bedforms in any of these experiments. This is not to say that dq_s/dx is constant over a wavelength, rather that averaged over many wavelengths the transport rate appears to be constant.

Expt. No.	τ^*	q_s^*	Time (hours)	Bedform Height (mm)	$\frac{Hu^*}{\upsilon}$
H-3	0.21	0.205	0.5	0.8	9.47
I-1	0.09	0.086	0.66	0.7	6.95
I-2*	0.11	0.113	no effect	2.5	28.49
I-2*	0.11	0.113	< 0.17	0.8	9.12
I-3	0.10	0.104	0.1667	0.7	7.64
I-5	0.09	0.091	0.667	0.8	8.19
J-4	0.18	0.042	no effect	0.9	9.96
K-3	0.10	0.046	0.33	0.9	9.84
L-1	0.08	0.023	0.67	0.8	7.83
L-3	0.10	0.046	0.5	0.9	9.77
L-4	0.09	0.018	1	1	10.07
N-2	0.14	0.041	1.5	0.8	7.83
U-3	0.16	0.088	no effect	0.5	4.41

Table 6.4: Experiments conducted in the 12-meter flume which developed bedforms larger than ~0.5 mm. Bedforms in experiment I-2 were 0.8mm high by the time the second transect was measured.

As indicated in Table 6.4, the bedform amplitude H (dimensionless, $H^* = Hu^*/\nu$) at which an increased transport rate is observed corresponds to the thickness of the viscous sublayer ($H^* \sim 7$ to 10, sublayer ~ 11.6). This suggests that the increase in transport rate is due to the ripple amplitude extending outside the viscous sublayer and developing an appreciable increase in shear along the upstream ripple face. Flow

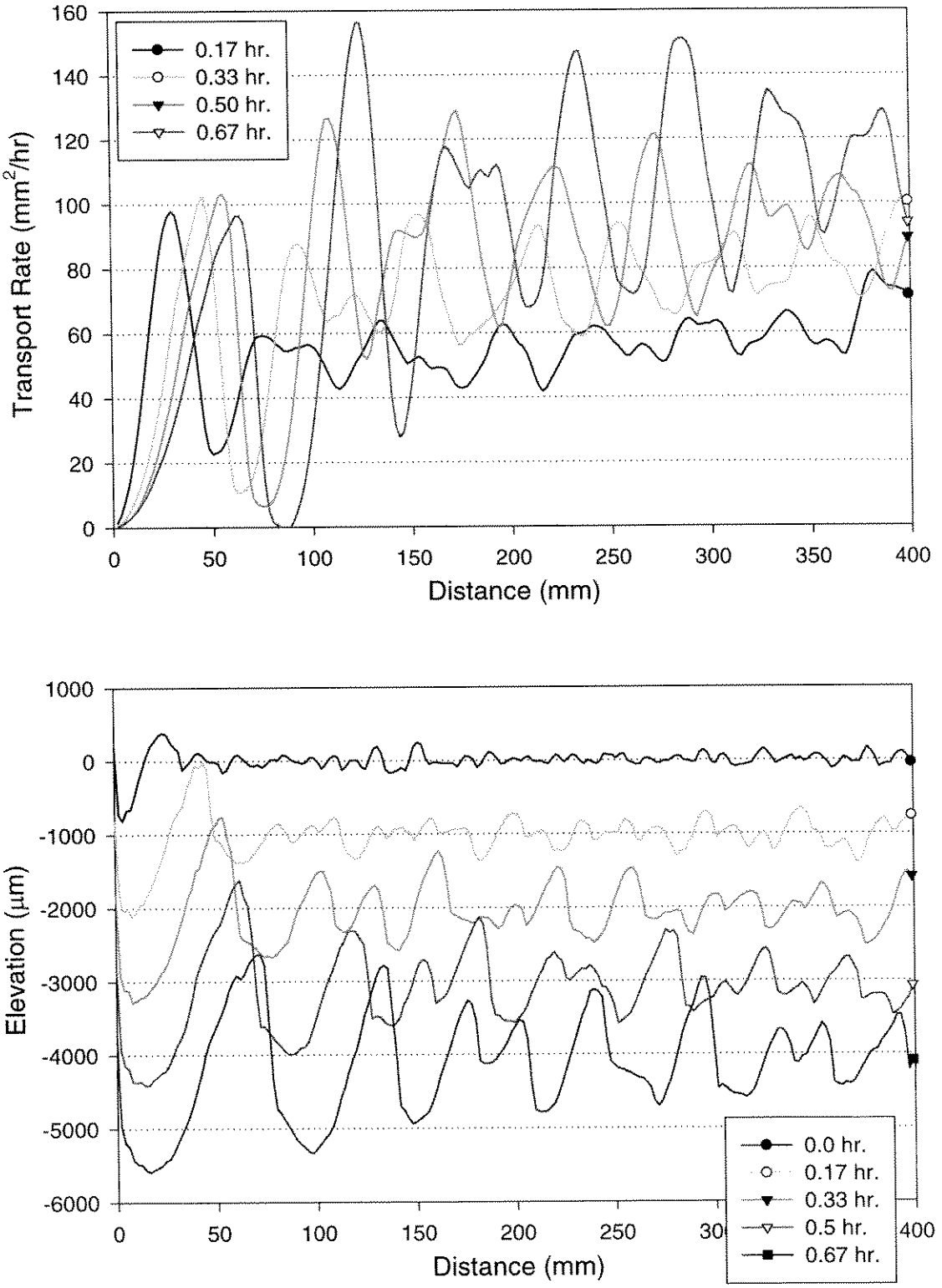

Figure 6.17: Experiment K-3 (69 μm) (a) Sediment transport rate, (b) corresponding bed elevation profiles, displaced by 1000 μm. Curves are labeled with the elapsed time, in hours.

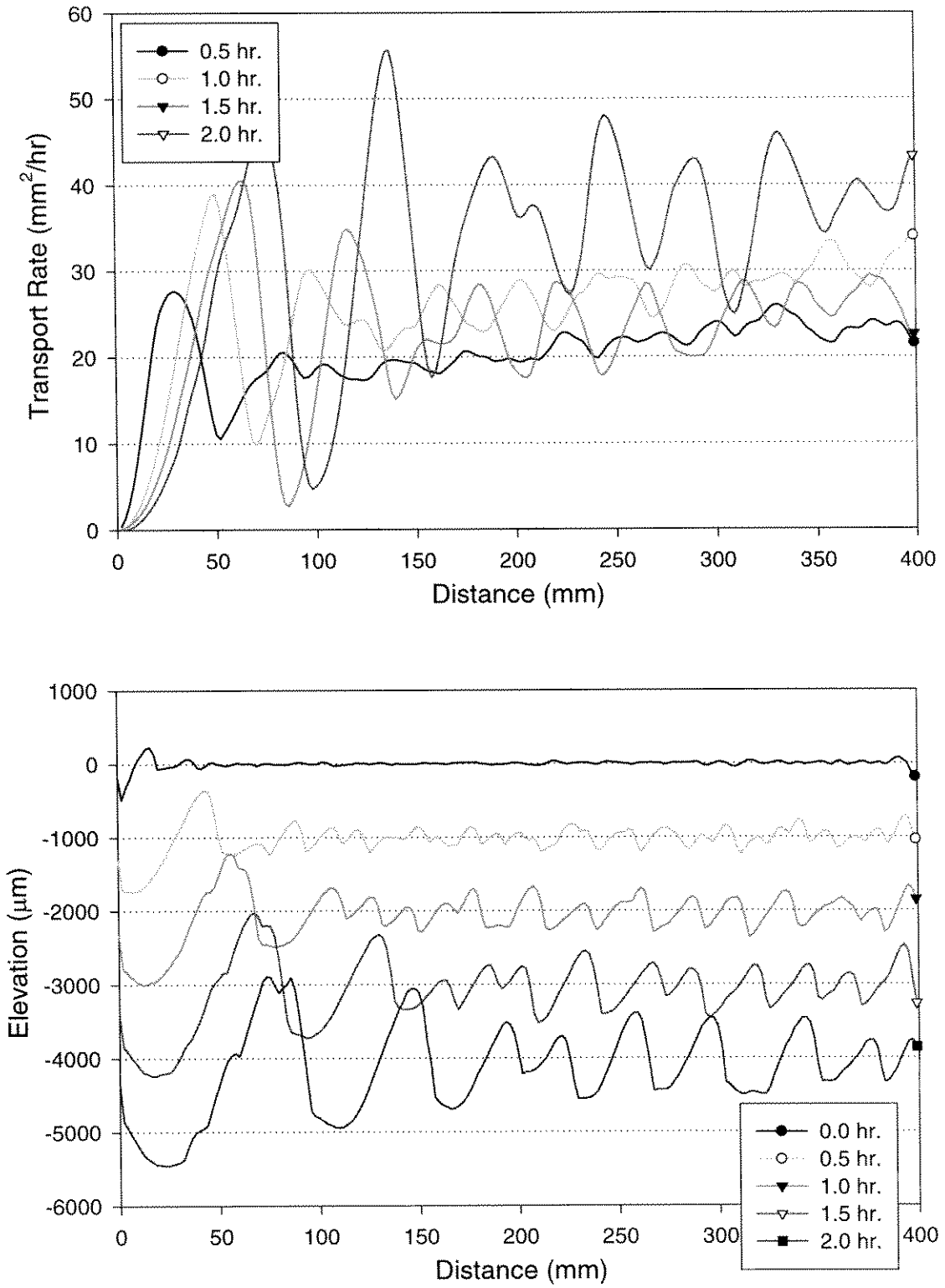

Figure 6.18: Experiment N-2 (41 μm) (a) Sediment transport rate, (b) corresponding bed elevation profiles, displaced by 1000 μm. Curves are labeled by the elapsed time in hours.

visualization with a small amount of dye indicated that the flow did separate over a ripple of ~2 mm in amplitude. Separation over ripples of other sizes was not investigated.

To correlate the mean bed shear with the measured transport rate, the bedform amplitude must be sufficiently small ($H^* < \sim 8$) to ensure that the average shear stress is not increased by ripple-flow interactions.

6.8 Summary

The experimental results obtained with a 10^{-4}M ionic strength solution resulted in the highest dimensionless transport rates observed. These transport rates, q_s^*, when plotted against the dimensionless shear stress τ^* defined a unique functional relationship within the limits of experimental errors, indicating that the dimensional and physical arguments of Chapter 3 are reasonable. However, a significant amount of care is required to obtain results that are non-cohesive at small particle diameters.

The effect of increased ionic strength is to decrease the transport rate at a given shear stress. The relative decrease in transport rate is smaller at higher shear rates, which is to be expected, as cohesion increases the threshold condition for motion.

The proposed model (Section 3.7) also provides reasonable agreement with the results of Unsold, if the assumed distribution of particle heights is modified. The modification is in a logical direction, and corresponds to a more angular material. From these modeling results, it appears that the transport rate, near the critical condition, is sensitive to both the water chemistry and the angularity of the sediment.

Measurement of the sediment transport rate with the laser displacement meter was repeatable and accurate for the range of sediment transport rates investigated. The

accuracy of this technique was limited for extremely small transport rates by random noise. Measurements of erosion rates below a 0.2 μm/hr decrease in the mean sediment bed elevation were highly uncertain. On the other extreme, the 10 minute time period that the instrument took to return to the same measuring point determined the maximum erosion rate that could be measured in these experiments. This was the limiting factor for the larger (120, 69 μm) sediment.

The sediment transport was, in general, constant with time. Two exceptions to this were observed. The first, an increase in transport rate correlated with increasing bedform amplitude, was most likely to occur with larger diameter sediments. It was observed that the bedform amplitude becomes important around a dimensionless ripple height (Hu^*/ν) of 8 to 10.

The second exception to a constant transport rate with time was an initial transient. Particularly for the smaller (26.5, 15 μm) sediments, a 2 hour decay time was typical of the non-cohesive experiments. The cause of this initial transient erosion is not understood, but may be related to the smaller particles deposited on the top of the sediment bed by the process of settling the particles into the test tray.

7 Summary and Conclusions

The transport rate of silt-sized sediments near the critical threshold of motion was measured and related to the bed shear stress and water chemistry. A novel method of measuring the total sediment transport rate was developed, using a highly accurate laser displacement meter to measure the elevation of the sediment bed. A unique scaling parameter for the sediment transport rate is derived from dimensional analysis for sediment transport conditions with bed Reynolds numbers less than one ($Re^* < 1$). Laboratory experiments in a recirculating flume showed that for non-cohesive particles, the results formed a single relation $q_s^* = \varphi(\tau^*)$, as predicted from the dimensional analysis. Increases in the electrolyte composition of the flume water reduced the sediment transport rate by up to two orders of magnitude, and demonstrated the importance of chemical interactions in predicting the sediment transport rate of silt-sized sediments.

7.1 Experimental Technique

A novel method of measuring the total sediment transport rate was developed, using a highly accurate laser displacement meter to measure the sediment bed's elevation. The transport rate is computed from the volume of sediment eroded from a small test bed, and experiments demonstrated that a 40 cm length of sediment bed was sufficient to achieve a transport rate independent of bed length.

Two large, recirculating laboratory flumes were equipped with a small sediment bed (20x8 cm, or 40x8 cm), from which the net volume of material eroded was calculated from measurements of the sediment's surface elevation with a laser displacement meter at various time intervals. The laser displacement meter contributed negligible error to the measurements, except at the lowest transport rates measured. The accuracy of each surface elevation measurement was +/- 10 μm. For typical experimental conditions, this created an uncertainty of about 0.2 mm^2/hr in the measured transport rate.

Experiments were conducted with four sizes of glass beads (d_g = 15 μm, 26.5 μm, 41 μm, 69 μm), which were cleaned to remove adsorbed metals and organic compounds. Two experiments used a 120 μm quartz sand instead of glass beads.

Experiments conducted with a sediment bed 40 cm long produced the same dimensionless sediment transport relation as obtained with the 20 cm long test bed (Figure 5.6). The ability to compute the sediment transport rate as a function of distance is a unique advantage of using surface elevation measurements to determine the transport rate. Typical experiments had an initial scour region, after which the transport rate became independent of distance, but varied over each bedform. These results demonstrated that a small sediment bed could be used to compute the sediment transport rate of silt-sized sediments. The majority of experiments in this study were conducted with the 40 cm long sediment bed.

7.2 Modeling

7.2.1 Dimensional Analysis

For silt-sized sediment at very low transport rates and bed Reynolds numbers less than one, the scaling relationship between variables was obtained from dimensional analysis. This analysis identified two dimensionless variables:

$$\tau^* = \frac{\tau}{(\rho_s - \rho)gd} \tag{7.1}$$

and

$$q_s^* = \frac{q_s \mu}{\tau d^2} \tag{7.2}$$

and predicted that non-cohesive material would have the relation $q_s^* = \varphi(\tau^*)$. This dimensionless transport rate parameter applies only for particles smaller than the viscous sublayer ($Re^* < 1$) at low transport rates, and is shown to be proportional to the fraction of the sediment bed that is in motion (n). The transport parameter q_s^* is different from those previously used by the inclusion of the dynamic viscosity μ, and the scaling on the shear stress τ instead of the shear velocity (u^*).

Dimensional analysis for the criterion for initiation of motion of particles smaller than the viscous sublayer ($Re^* = u^*d/\nu < 1$) produced only one dimensionless parameter, the Shields parameter, or dimensionless shear stress. This implied that the critical condition corresponds to a constant τ_c^*,

$$\tau_c^* = \frac{\tau}{(\rho_s - \rho)gd} = \text{constant for } Re^* < 1 \tag{7.3}$$

The condition for initiation of motion can be made objectively, instead of subjectively by visual observation, by defining the threshold as a value of q_s^*, such as $q_{sc}^* = 0.01$, corresponding to about 2% of the bed surface in motion. The corresponding τ_c^* is determined from the measured relation $q_{sc}^* = \varphi(\tau_c^*)$.

7.2.2 Transport Model

A sediment transport model was proposed that combines the distribution of viscous wall shear stresses, variable bed stability through a distribution of particle geometries, and a threshold of motion obtained by a torque balance. This model incorporates a simplistic view of the particle geometry, but the results agree with the dimensional analysis prediction, that the sediment transport rate can be described as a function of $q_s^* = \varphi(\tau^*)$

Scaling analysis of the Navier-Stokes equations suggested that the flow around a particle on the sediment bed would be adequately described by the quasi-steady Stokes equation. It is proposed that turbulent bursting along the bed can be modeled as a non-inertial stochastic process using the probability distribution of wall shear stresses.

The turbulent vertical velocity fluctuations near the bed are shown to be unable to lift particles off the sediment bed, supporting the use of a sediment transport rate parameter to describe the sediment mobility at or near the critical condition.

A parameter to describe a cohesive force (Fc) between particles is added to the model, with the result that $q_s^* = \varphi(\tau^*)$ for constant chemical conditions. Increased values of Fc shift the relation $q_s^* = \varphi(\tau^*)$ to predict lower transport rates. Finally, the cohesive

force between particles is shown to be proportional to the square of the particle's diameter, if the cohesion is described by a force per unit area between parallel plates.

The experimental results of Unsold (1984) were expressed in terms of the dimensionless quantities proposed in this work, and were found to collapse better than his original scaling (Figure 6.8). The predictions of the new transport model were found to provide reasonable agreement with these results if an adjustment was made to one parameter. This change had a physical meaning, corresponding to the increased angularity of the sediment material.

7.3 Experimental Results

Two recirculating laboratory flumes were used, one to enable high Reynolds number flow and the other to provide a sufficiently small volume for practical control of water composition. No effect of the flume size was observed, as the experiments conducted in the 12-meter flume with Pasadena tap water showed general agreement with the transport rate relations obtained in the 40-meter flume.

7.3.1 Non-Cohesive Results

The highest transport rates were observed for all particle sizes (d_g = 15 μm, 26.5 μm, 41 μm, 69 μm) in experiments conducted with lowest ionic strength, approximately 10^{-4}M. These were classified as non-cohesive, and formed a unique relation between τ^* and q_s^*. A least squares fit to the logarithms of the dimensionless parameters gave

$$q_s^* = 3.81\tau^{*2.22} \text{ for } 0.05 < \tau^* < 0.3 \quad (7.4)$$

All of the sediment beds in these experiments gradually developed ripple-like bedforms, which continued to grow in wavelength and amplitude.

For transport rates below $q_s^* \sim 0.1$, the sediment transport rate model provided a reasonable fit to the non-cohesive results. This gave a physical interpretation of the results in terms of the fraction of the bed surface moving, based on a stochastic view of turbulence and particle stability.

The finer sediments (15 μm, 26.5 μm) displayed an initial transient period, in which the transport rate increased with distance, but decayed in time (typically < 2 hours) to a value independent of position. This was also recorded in a few experiments with larger particles, but the decay time was always less than 10 minutes.

Experiments conducted in the 40-meter flume (110 cm wide x 60 cm deep) looked at the influence of large mean flow Reynolds numbers (up to $Re_{Dh} = 2.5\ 10^5$) on resuspending fine sediments. No effect of the Reynolds number could be distingushed between experiments run at a depth of 11 cm depth ($4\ 10^4 < Re < 8\ 10^4$) and 40 cm ($1\ 10^5 < Re < 2.5\ 10^5$). The sediment moved as bedload, and the bed developed ripple-like bedforms, which grew in amplitude and wavelength as time progressed. When a bedform Reynolds number (Hu^*/ν, H = bedform amplitude) reach a value between 7 and 10, the sediment transport rate was observed to increase.

7.3.2 Cohesive Results

A reduction in the sediment transport rate was observed for clean glass beads that corresponded to increasing electrolyte composition. These experiments used deionized

water in the flume, with electrolyte concentrations of NaCl and $CaCl_2$ up to 10^{-2} M. All particle sizes showed reduced transport rates for increasing salt concentrations, except for the 69 μm diameter glass beads, which showed no reduction in transport for 10^{-2} M NaCl compared to 10^{-4}M. For each particle size, the decrease in sediment transport rate corresponded with 10^{-3} M NaCl ~< 3.3 10^{-4} M $CaCl_2$ < 10^{-2} M NaCl < 3.3 10^{-3} M $CaCl_2$. At similar ionic strengths, calcium was more effective at reducing the sediment transport rate than sodium.

Experiments with all four sediment sizes were conducted in a 10^{-2}M NaCl solution. Smaller particle sizes had a greater reduction in the dimensionless transport rates from the non-cohesive results. This trend was captured by the model, which predicts that the dimensionless transport rate (q_s*) should decrease as d^{-2} for constant (cohesive) chemical conditions.

Modeling of the interparticle forces with DLVO theory, accounting for electrostatic and van der Waals forces, did not predict the significant cohesive forces observed in this study. The presence of specific covalent or ionic forces between contacting particles could account for the cohesive forces observed.

The aging of the glass beads in deionzied water was shown to reduce the transport rate by more than 50%, compared with freshly prepared particles.

7.4 Application to natural systems

In natural water systems, where low ionic strength waters and perfectly clean particles are unlikely to be found, fine sediments should be expected to exhibit some degree of cohesion. The sediment transport/mobility will no longer be solely dependent on the dimensionless shear stress τ^*. Rather, an understanding of the inter-particle chemical forces, which may change with age, will be essential in obtaining a correct estimation of the sediment's mobility.

7.5 Main Conclusions

1. The dimensionless transport rates for uniform sediments of different mean particle sizes comprise a unique function of the dimensionless shear stress, $q_s^* = \varphi(\tau^*)$ (see Equations (7.1) and (7.2)). The parameter q_s^* corresponds to approximately 0.5 times the fraction of the sediment bed in motion for $Re^* < 1$. Thus, for a constant fraction of the sediment bed in motion, Shields curve becomes independent of Re^* below one. The value of Shields parameter varies with the amount of transport deemed critical.
2. For non-cohesive sediments, the criterion $\tau_c^* = 0.075$ is proposed as an extension to Shields' curve (Figure 6.2) for $Re^* < 1$, based on matching q_s^* with sand-sized results at $Re^* = 1$. This extension is equivalent to $q_s^* \sim 10^{-2}$, or 2% of the sediment bed in motion.
3. The dimensionless shear stress (τ^*) and transport rate (q_s^*) parameters, obtained from dimensional analysis of the problem, reduce the non-cohesive results to a single

dimensionless curve of q_s^* vs. τ^* ($0.05 < \tau^* < 0.3$). The parameters have a simple physical interpretation, and are the appropriate dimensionless variables to explain non-cohesive sediment transport for small bed Reynolds' numbers ($Re^* < 1$).

4. The effect of a fluctuating shear stress and cohesion was incorporated into a stochastic-type transport model. The model incorporates only one layer of moving particles, and thus is limited to small transport rates. The transport model fits the non-cohesive data well for $q_s^* < \sim 0.1$. See Figure 6.4 for the data's agreement to the model curve, and Equation (7.4) for a power-law approximation to the model.
5. Small increases in the electrolyte concentration of the flume water resulted in a substantial decrease (up to one or two orders of magnitude) in the sediment transport rate. Calcium was more effective at reducing the transport rate than sodium for similar ionic strengths. This decrease in the sediment transport rate results in Shields curve to rise sharply for cohesive sediments as Re^* decreases (see Figure 6.7). The transport model shows the same trend, and simulated the trend of reduced sediment transport rates observed in the cohesive experiments with a single parameter representing the net interparticle force. For example, see Figure 6.5 for 26.5 μm sediment. Experimental reproducibility requires meticulous chemical control, of both sediment surface properties and water composition.
6. Sediment transport rates can be calculated as a function of time and longitudinal distance from measurements of the sediment bed's surface elevation with a laser displacement meter. This work demonstrated that the transport rate reached a constant value in time and distance within the length of the 40 cm sediment test bed.

Thus the mobility of silt-sized sediments can be studied in a laboratory flume utilizing only a small sediment test bed.

7. Flume experiments demonstrated that the particles were transported as bedload for the range of flow conditions $0.05 < \tau^* <\sim 0.3$. The sediment bed developed very low ripple-like bedforms that were essentially two-dimensional in nature. The amplitude and wavelength of the bedforms increased as time progressed. Typical bedforms ranged from 0.1 mm to 2 mm in height, and from 15mm to 70 mm in length.
8. The sediment transport rate was observed to increase when the ripple Reynolds number $\frac{Hu^*}{\upsilon}$ reach 8 to 10. However, no evidence of suspension into the mean flow was seen under the conditions studied ($\tau^* < 0.3$).

References

Alfredsson, P.H., Johansson, A.V., Haritonidis, J.H., Eckelmann, H., 1988. The fluctuating wall-shear stress and the velocity field in the viscous sublayer. *Phys. Fluids*, 31(5), 1026-1033.

ASCE - Task Committee on Erosion of Cohesive Materials, 1968. Erosion of cohesive sediments, *J. Hydraul. Div., ASCE*, 94 (HY4): 1017-1049.

Black, C.A. (Ed.), 1965. *Methods of Soil Analysis*, American Society of Agronomy, Madison, WI.

Buffington, J.M., Montgomeryj, D.R., 1997. A systematic analysis of eight decades of incipient motion studies, with special reference to gravel-bedded rivers. *Water Resour. Res.*, 33(8), 1993-2029.

Cleaver, J.W., Yates, B., 1973. Mechanism of Detachment of Colloidal Particles from a Flat Substrate in a Turbulent Flow. *J. Colloid Interface Sci.*, 44(3), 464-474.

Dade, W.B., Nowell, A.R.M., Jumars, P.A., 1992. Predicting Erosion Resistance of Muds. *Marine Geology,* 105, 285-297.

Doremus, R.H., 1994. *Glass Science*, 2nd Ed., John Wiley & Sons, New York, NY.

Elyers, H., 1994. Transport of Adsorbing Metal Ions between Stream Water and Sediment Bed in a Laboratory Flume. PhD Thesis, CIT, Pasadena, CA.

Garcia, M., Nino, Y., Lopez, F., 1996. Laboratory Observations of Particle Entrainment into Suspension by turbulent Bursting. In "Coherent flow structures in open Channels: origins, scales, and interactions with sediment transport," Edts. Best et al., John Wiley & Sons.

Grass, A.J., 1970. Initial Instability of Fine Bed Sand, *J. Hydraul. Div. ASCE*, 96 (HY3): 619-632.

Iler, R.K., 1979. *The Chemistry of Silica.* Wiley-Interscience, New York, NY.

Israelachvili, J.N., 1991. *Intermolecular and Surface Forces*, 2nd Ed. (Academic, New York).

Junda, C., Zhiliang, W., 1989. Condition of incipient motion of cohesive sediment, *Fourth International Symposium on River Sedimentation*, pp. 490-497.

Kennedy, J.F., 1995. The Albert Shields Story. *J. Hydraul. Eng., ASCE.* v121(11). p.766-772.

Kim, H.T., Kline, S.J., Reynolds, W.C., 1971. The production of turbulence near a smooth wall in a turbulent boundary layer, *J. Fluid Mech.*, 50: 133-160.

Kulkarni, R.D., Somasundaran, P., 1977. Effect of Pretreatment on the electrokinetic properties of Quartz, *International Journal of Mineral Processing*, 4: 89-98.

Lavelle, J.W., Mofjeld, J., 1987. Do Critical Stresses for Incipient motion and erosion really exist? *J. Hydraul. Eng.*, 113 (3): 370-393.

Leighton, D., Acrivos, A., 1986. Viscous Resuspension, *Chem Eng. Sci.*, 41 (6), 1377-1384.

Lifshitz, E.M., 1956. The theory of molecular attractive forces between solids, *Soviet Physics JETP*, 2: 73-83.

Ling, C., 1995. Criteria for Incipient Motion of Spherical Sediment Particles. *J. Hydraul. Eng.*, 121 (6), 472-478.

Litton, G.M., Olson, T., 1993. Colloid Deposition Rates on Silica Bed Media and Artifacts Related to Collector Surface Preparation Methods, *Environ. Sci. Technol.*, 27: 185-193.

Lyn, D.A., 1986. Turbulence and Turbulent Transport in Sediment Laden Open-Channel Flows. PhD Thesis, California Institute of Technology, Pasadena, CA.

Lyn, D.A., 1993. Turbulence Measurements in Open-Channel Flows over Artificial Bed Forms *J. Hydraul. Eng.*, 119 (3), 306-326.

Mantz, P.A., 1977. Incipient Transport of Fine Grains and Flakes by Fluids - Extended Shields Diagram, *J. Hydraul. Div., ASCE*, 103 (HY6): 601-615.

Mehta, A.J., Lee, S., 1994. Problems in Linking the Threshold Condition for the Transport of Cohesionless and Cohesive Sediment Grains, *J. Coastal Res.*, 10 (1): 170-177.

Miller, R.L., Bryne, R.J., 1966. The angle of repose for a single grain on a fixed rough bed, *Sedimentology*, 6: 303-314.

O'Neill, M.E., 1968. A sphere in contact with a plane wall in a slow linear shear flow, *Chem. Eng. Sci.*, 23: 1293-1298.

Onoda, G.Y., DeBruyn, P.L., 1966. Proton Adsorption at the Ferric Oxide/Aqueous Solution Interface, *Surface Sci.*, 4: 48.

Otsubo, K., Muraoka, K., 1986. Resuspension of Cohesive Sediments by Currents, *Third International Symposium on River Sedimentation*, pp. 1680-1689.

Packman, A.I., 1997. Exchange of colloidal Kaolinite between stream and sand bed in a laboratory flume. PhD Thesis, CIT, Pasadena, CA.

Partheniades, E., 1993. Erosion and Deposition of Cohesive Soils, *J. Hyd. Div. ASCE*, 91 (HY1): 105-139.

Price, T.C., 1985. Slow linear shear flow past a hemispherical bump in a plane wall, *Quarterly Journal of Mechanics and Applied Mathematics*, 38: 93-104.

Raudkivi, A.J., 1990. *Loose Boundary Hydraulics*, 3rd Ed., Permgamon Press, New York.

Rea, R.L, Parks, G.A., 1990. Numerical Simulation of Coadsorption of Ionic Surfactants with Inorganic Ions on Quartz. In "Chemical Modeling of Aqueous Systems II," Edts. Melchior, D.C., Bassett, R.L., American Chemical Society.

Rees, A.I., 1966. Some flume experiments with a fine silt, *Sedimentology*, 6: 209-240.

Rouse, H. (Ed.), 1950. *Engineering Hydraulics*, John Wiley & Sons, New York, NY.

Russel, W.B., Saville, D.A., Schowalter, W.R., 1989. *Colloidal Dispersions*, Cambridge University Press, Cambridge.

Shields, A., 1936. Anwendung der Aehnlichkeitsmechanik und der Turbulenzforschung auf die Geschiebebewegung, *Mitteilungen der Preussischen Versuchsanstalt fur Wasserbau und Schiffbau*, 26. (English translation by P. Ott & J.C. Uchelon, CIT.)

Stumm, W., Morgan, J.J., 1981. *Aquatic Chemistry*, 2nd Ed., John Wiley & Sons, New York.

Stumm, W., Morgan, J.J., 1996. *Aquatic Chemistry*, 3rd Ed., John Wiley & Sons, New York.

Unsold, G., 1984. Der Transportbeginn feinstkornigen rolligen Sohlmaterials in gleichformigen turbulenten Stromungen: Eine experimentelle Uberprufung und Erweiterung der Shields-Funktion, *Reports Sonderforschungsbereich 95*, Universitat Kiel 70.

Vanoni, V.A., 1964. Measurements of critical shear stress for entraining fine sediments in a boundary layer, *W.M. Keck Lab Report KH-R-7*.

Vanoni, V.A., 1975. Sediment Transportation Mechanics: Initiation of Motion, *Sedimentation Engineering*, V.A. Vanoni, Ed., ASCE, New York, NY.

Vigil, G., Xu, Z., Steinberg, S., Israelachvili, J., 1994. Interactions of Silica Surfaces. J. *Colloid Interface Sci.*, 165, 367-385.

Vorshneya, A.K., 1994. Fundamentals of Inorganic Glasses, Academic Press, New York, NY.

White, C.M., 1940 The equilibrium of grains on the bed of a stream. *Proc. Roy. Soc. Lond. A.*, 174, 322-338.

White, F.M., 1986. Fluid Mechanics, 2nd Ed. McGraw-Hill, New York, NY.

White, S.J., 1970. Plane Bed Thresholds of Fine Grained Sediments, *Nature*, 228: 152-153.

Wiberg, P.L., Smith, J., 1987. Calculations of the Critical Shear stress for Motion of Uniform and Heterogeneous Sediments, *Water Resour. Res.*, 23 (8): 1471-1480.

Willmarth, W.W., 1975. Pressure Fluctuations beneath Turbulent Boundary Layers. *Annual Review of Fluid Mech.*, 7, 13-38.

Yalin, M.S., Karahan, J., 1979. Inception of Sediment Transport, *J. Hydraul. Div. ASCE*, 105 (HY11): 1433-1443.

Appendix A - Chemical Modeling

The chemical conditions within the 12-meter flume were set by addition of specific amounts of electrolyte to deionized water, and allowed to equilibrate with the atmosphere. The ability to control the water chemistry was limited by practical considerations: the size (600L) and the galvanized steel construction of the flume. Experimentally, the transport rate of the glass beads was sensitive to the chemical composition of the flume water, as well as to the cleaning procedure of the glass beads. The influence and importance of possible chemical interactions were investigated by modeling the equilibrium chemistry of the system, and estimating the inter-particle forces from DLVO theory.

It is assumed that a decrease in sediment transport rate under otherwise identical flow conditions, corresponded to an increase in cohesion. For freshly prepared glass beads, the cohesion increased as 10^{-4} M $NaHCO_3$ < 10^{-3}M NaCl < 3.3 10^{-4} M $CaCl_2$ < 10^{-2} M NaCl < 3.3 10^{-3} M $CaCl_2$. The sediment transport rate, with the same electrolyte solution, decreased with decreasing particle size. Glass beads that had aged in deionized water for more than one to two months displayed increased cohesion relative to their freshly prepared state. All material required an initial cleaning before non-cohesive behaviour was observed.

DLVO Modeling

The colloidal interactions of silica particles are generally considered in terms of the attractive van der Waals and repulsive electrostatic force (the DLVO theory). This theory was applied to the silt-sized glass beads used in this work to understand the nature of the chemical interactions. For the interaction between two spheres, the attractive force is:

$$F_a(h) = \frac{Aa}{6h^2} \qquad \text{(A.1)}$$

where A is the Hamaker constant, a the particle radius, and h the separation between spheres. The repulsive force

$$F_r = -\frac{64\pi\, 10^3 \mathrm{I}}{\kappa} RTa\gamma^2 e^{-\kappa \mathrm{h}} \quad \gamma = \tanh\left(\frac{ze\psi_d}{4kT}\right) \qquad \text{(A.2)}$$

where I is the ionic strength, $\frac{1}{2}\sum c_i z_i^2$, κ is the debye length, $\frac{2.8\cdot 10^{-10}}{\sqrt{\mathrm{I}}}\,\mathrm{m}$, R the gas constant, k the Boltzman constant, T temperature, z the ionic charge, e the charge of an electron, and Ψ_d the diffuse potential. DLVO theory assumes the net force between particles is the arithmetic sum of these two forces. This theory is complicated by the fact that value of the Hamaker constant decreases with distance, and additional short range repulsive forces have been observed at short (< 4 nm) distances. At larger separations, experimental measurements have produced excellent agreement with this theory (Vigil).

The unretarded Hamaker constant between amorphous silica surfaces in water is about $8\cdot 10^{-21}$J (Russel, et al., 1989, pg 148). The retarded Hamaker constant, $A_{eff}(h)$, is obtained from the definition:

$$\Phi_{fp}(h) = - 12\pi h^2 A_{eff}(h) \qquad (A.3)$$

where h is the particle-particle separation distance, and $\Phi_{fp}(h)$ is the interaction energy of two flat plates that can be found from the theory of Lifshitz (1956) (see Russel, Saville, Schowalter, 1989). For sphere-sphere geometry and h/a << 1, the attractive force is

$$F_a(h) = \frac{A_{eff}(h)a}{6h^2} \qquad (A.4)$$

Thus the net force is proportional to the particle diameter, and the maximum force corresponding with the secondary potential minimum occurs at a separation (h) given by:

$$\frac{A_{eff}(h)}{384\pi\, 10^3 I\, RT\gamma^2} - h^3 e^{-\kappa h} = 0 \qquad (A.5)$$

Assuming $|\psi_d|$ > 50 mV, then $\gamma \cong 1$, and for a medium with an ionic strength of 0.01 M, the location of the maximum force in the secondary minima, F_{max}, occurs at a separation of ~30 nm. Under these conditions, $A_{eff}(30nm) = 2.0\times10^{-21}$ J for a silica-water-silica system, which is about 25% of its non-retarded value. Substituting these values into equation (A.3) results in a force that is only a few percent of the weight of a 15 μm particle.

The predicted force vs. distance curves between two spherical particles normalized by the particle radius is shown in Figure A.1. It was assumed that the particle's self-weight was the only force acting to push the surfaces together. The range of particle weights, corresponding to 15 μm and 70 μm particles are also shown in Figure A.1.

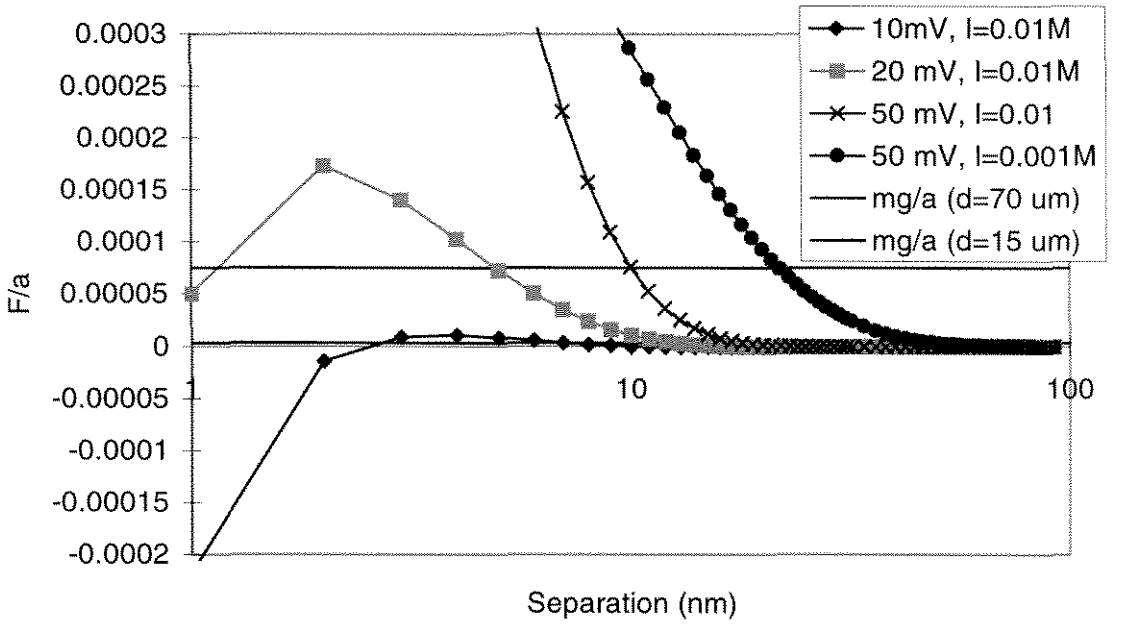

Figure A.1: Predicted forces between two particles from DLVO theory. Forces are normalized by the particle radius.

On this linear scale, the attractive force due to the secondary minimum is almost indiscernible, but occurs around 30 nm at I=10^{-2}M and at 90 nm at an ionic strength of 10^{-3}M. The electrostatic repulsion is many times larger than the particle self weight, suggesting that the particles should not be able to overcome the repulsive energy barrier to reach the primary minimum.

The above DLVO theory assumes that the particles are molecularly smooth, and spherical. As shown in Figures 4.6 to 4.8, the majority of the glass beads are spherical. Atomic force microscopy (AFM, Digital instruments) was used to measure the surface profile of several particles from the 41 μm material. Some particles were smooth to within a few nanometers. The majority of particles showed some 'blob' like surface features, usually 10 to 50 nm in height and 0.5 to 2 μm in diameter. The presence of these surface roughness elements suggest that their radius of curvature should be used

instead of the particle radius to calculate the interaction energy and forces. A typical radius of curvature of such a bump is about 10 μm. Thus, a bump would decrease the interaction force by about a factor of two. From Figure A.1, this decreased repulsive force would still be sufficient to prevent the particles from coming into contact.

The diffuse potential used in the DLVO calculation was taken as the electrophoritic (zeta) potential of the particles (see Section 4.2.2). At the pH of the flume experiments (pH ~7), the measured zeta potentials (Figure 4.10) were -45 mV at $I = 10^{-2}$M, and -85 mV at $I = 10^{-4}$M. Chemical surface models were used to determine if this value might be reduced by the specific adsorption of metal ions from the flume.

Surface Chemical Modeling

The rusting of the flume sidewalls and return piping introduced abundant amounts of iron oxides, which is known to strongly adsorb to silica surfaces (Stumm and Morgan, 1996). However, iron is also relatively insoluble in water in the Fe(III) state at neutral pHs. The soluble concentration was determined by assuming equilibrium with solid $Fe(OH)_3$. The chemical reactions considered were:

$$\text{(am) } Fe(OH)_3(s) = Fe^{3+} + 3OH^- \qquad \log K = -39$$

the majority of the dissolved iron is present as the iron-hydroxide species:

$$Fe^{3+} + H_2O = FeOH^{2+} + H^+ \qquad \log K_1 = -2.19$$

$$Fe^{3+} + 2H_2O = Fe(OH)^{2+} + 2H^+ \qquad \log \beta_2 = -5.67$$

Schindler et al, (1976) measured Fe^{3+} adsorption on silica surfaces in 3.0 M $NaClO_4$, and reported:

$$>SiOH + Fe^{3+} = >SiO\text{-}Fe^{2+} + H^+ \qquad \log {}^*K_{1s} = -1.77$$

$$2 >SiOH + Fe^{3+} = (>SiO)_2\text{-}Fe^{+} + 2H^{+} \qquad \log {}^{*}\beta_2 = -4.22$$

They found that a simplified model with $\Psi = 0$ fit their data, which for a pH of 7.5, gives:

$$[Fe^{3+}] = 10^{-18}M$$

$$\frac{\{>SiO \cdot Fe^{2+}\}}{\{>SiOH\}} = 10^{-12.3}$$

$$\frac{\{(>SiO)_2 \cdot Fe^{+}\}}{\{>SiOH\}^2} = 10^{-7.22}$$

Thus it was concluded that the amount of dissolved iron in the flume was too low to affect the surface potential of the glass beads.

Both sodium and calcium are reported to adsorb weakly to silica surfaces, although Rae and Parks (1990) have suggested that calcium bonds strongly. To investigate this, the triple layer model that Rae and Parks used was adopted to ensure model consistency. The triple layer model is a type of surface chemical model, which attempts to describe adsorption phenomena using an equilibrium approach. The triple layer model assumes only the proton (H^+) and hydroxyl ion (OH^-) are adsorbed directly onto the surface, with a potential Ψ_o. All other ions are adsorbed at a secondary plane of potential Ψ_1, as outer-sphere complexes. Non adsorbed ions form a diffuse layer extending outwards from the third layer, where the potential is Ψ_d. Each of these three layers has an associated charge density σ and are related by two capacitances, C_1 and C_2. To implement this model, the SURFEQL (Faughnan, 1981) computer program was used. The model parameters that were assumed were: $C_1 = 1.25$ F/m, $C_2 = 0.20$ F/m.

A bulk volume of about 100 mL of glass beads was needed to fill the test tray, resulting in a solid concentration of 0.25 g/L in the 600L flume. The surface area was taken as 0.08 m^2/g, corresponding to 30 μm particles.

The protonation constants of the silica surface were taken as $pK_{a1} = -3.2$, $pK_{a2} = 7.2$, giving a pH_{pzc} of 2.0, in agreement with the zeta potentials measured (Section 4.2.2). For the effect of a sodium chloride electrolyte, the equilibrium constants and reactions considered are summarized in Tables A.1.

Reaction	Equilibrium Constant
$>SiOH_2^+ = >SiOH + H^+$	$\log K_{a1,int} = -3.2$
$>SiOH = >SiO^- + H^+$	$\log K_{a2,int} = -7.2$
$>SiOH + Na^+ = >SiO\text{-}Na + H^+$	$\log {}^*K_{Na+,int} = -6.7$

Table A.1: Reactions and intrinsic equilibrium constants for surface ionization and sodium adsorption.

For the calcium chloride electrolyte,

Reaction	Equilibrium Constant
A $>SiOH + Ca^{2+} = >SiO\text{-}Ca^+ + H^+$	$\log {}^*K_{Ca2+} = -3.8$
B $>SiOH + Ca^{2+} = >SiO\text{-}CaOH + 2H^+$	$\log {}^*K_{CaOH+} = -13.5$
C $>SiOH + Ca^{2+} = >SiO\text{-}Ca^+ + H^+$	$\log {}^*K_{Ca2+} = -6.8$

Table A.2: Reactions and intrinsic equilibrium constants for calcium adsorption.

Rae and Parks (1990) suggest adsorption of calcium follows of reactions A and B in Table A.2. These suggested equilibrium constants produce enough specific adsorption of calcium that the surface potential reverses sign at the higher concentration of $CaCl_2$ used. This is thought to be unrealistic, so the $\log {}^*K_{ca2+} = -6.8$ (Reaction C, Table A.2)

value was added. This is the adsorption value Eylers (1994) found for zinc adsorption on quartz. He also reported that calcium sorbed less than zinc, but no value was given. Thus this must be take as an upper limit, but predicts much less adsorption that the values of Rae and Parks.

The resulting diffuse layer potentials are tabulated below:

Water composition	Equilibrium Constants	Calculated Diffuse Layer Potential (mV)
		pH = 6.9
10^{-4}M NaCl		-77.7 mV
10^{-3}M NaCl		-69 mV
10^{-2}M NaCl		-38.6
3.3 10^{-4}M $CaCl_2$	log $*K_{ca2+}$ = -6.8	-54.2
3.3 10^{-3}M $CaCl_2$	log $*K_{ca2+}$ = -6.8	-24.3
3.3 10^{-4}M $CaCl_2$	log $*K_{ca2+}$ = -3.8	-1.7mV
3.3 10^{-3}M $CaCl_2$	log $*K_{Ca2+}$ = -3.8	12.3 mV

Table A.3: Calculated diffuse layer potentials.

Otherwise, the silica surface remains negatively charged, with a diffuse potential of at least 25 – 35 mV. According to the DLVO theory, this would be sufficient to prevent the sediment particles from agglomerating under their own self weight. Thus metal ion adsorption to the sediment surfaces is not believe to be the cause of the cohesion.

Portions of the flume's side wall and return pipe was observed to be actively rusting, and colloidal iron accumulated on the poly air filter at the upstream entrance to the flume channel (see Section 4.1). As discussed in Chapter 5, during experiments with the 26.5 μm particles it was found that after about one week in the flume, the particles contained significant amounts of iron. Amounts of 100-140 μM Fe were measured in the 1.0N HCl used to wash the particles. The corresponding particle surface area was about 90 m^2/L. As this amount of iron is in excess of what is expected to be present from dissolved iron species, it was assumed that the sediment bed was accumulating colloidal iron particles.

Colloidal iron could increase cohesion in two ways, (a) it could form as a bridge between particles, and (b) it would adhere onto the silica surfaces, reducing the effective surface potential. The greatest effect of the colloidal iron was likely to stabilize the surfaces of experiment with very low transport rates ($q_s^* < 10^{-3}$). The long duration (8-24 hours) of these low transport experiments allowed colloidal iron to attach to the surface particles and increase their stability. However, it is not thought that colloidal iron is the primary cause of the cohesion observed, since the reduction in transport rate was observed to vary systematically with the electrolyte concentrations. Additionally, this reduction in transport occurred after the flume had been rinsed and refilled with water, when a low concentration of colloidal particles would be expected.

In their review of the Interactions of Silica Surfaces, Vigil et al. (1994) note that when silica groups are exposed to water for an extended period of time, the conversion of Si-O-Si groups into silanol Si-OH groups can continue and form polymeric chains. The

chains are of the form $-Si(OH)_2-O-Si(OH)_2-OH$, which are able to link up in many different ways and create a three-dimensional network or silica gel.

It appears that these polymeric chains contribute to the increased cohesion observed with the glass beads upon aging. Environmental SEM pictures of freshly cleaned glass beads (about 2 weeks old) and aged particles (about 9 months old) are shown in Figures A.2 and A.3. In this SEM the particles are placed into the instrument wet, and the residual surface water is used to adsorp the electrons. Note that a lower pressure (absolute) was obtainable with the 'old' particles, indicating that the surface was hydrated to a greater extend. Small 'bumps' could also be distinguished on the old particles to a much greater extent than the 'new' (freshly prepared) particles.

Vigil et al also report that these protruding silanol groups react with similar groups on an opposite surface (sinter). Iler (1979, pg 540, 545-546) also reported that silica particles are known to sinter to each other, a process that is apparently catalysed by the presence of water.

As a result, the following explanation is suggested to describe the cohesive nature of the experimental results. For freshly cleaned particles, in which the extent of the silica 'hairs' are small, low ionic strength water affords the particles a high diffuse potential and a correspondingly large inter-particle separation distance. As the ionic strength is increased, the particle separation distances decrease and the importance of specific interactions of the silica surface increase. The fact that glass beads were used likely contributed to the increased importance of these effects, as amorphous silica is known to be less stable than the crystalline (quartz) form. Additionally, the glass matrix is permeable to hydronium ions, and it is well known that sodium ions will diffuse out of

the glass into solution, and be replaced with H_3O^+, which may have accelerated the rate of hydrolysis of the surface layer.

The increased cohesive effect of calcium chloride electrolyte compared with the equivalent ionic strength of sodium chloride was apparently due to a specific adsorption of calcium to the surface. Reported values of the equilibrium constant vary too much to make a good estimation of this effect.

The presence of colloidal iron likely sorbed to the silica surfaces, and may have formed bridge points between particles, and/or reduced the surface potential. This may have increased the stabilization of experiments with very low sediment transport rates ($q_s^* < 10^{-3}$).

References

Elyers, H., 1994. Transport of Adsorbing Metal Ions between Stream Water and Sediment Bed in a Laboratory Flume. PhD Thesis, CIT, Pasadena, CA.

Faughnan, J., 1981. The SURFEQL/MINEQL Manual.

Schindler P.W., Furst, B., Dick, R., Wolf, P.U., 1976. Ligand Properties of Surface Silanol Groups. J Colloid Interface Sci. 55, 469-475.

Iler, R.K., 1979. *The Chemistry of Silica.* Wiley-Interscience, New York, NY.

Rea, R.L, Parks, G.A., 1990. Numerical Simulation of Coadsorption of Ionic Surfactants with Inorganic Ions on Quartz. In "Chemical Modeling of Aqueous Systems II," Edts. Melchior, D.C., Bassett, R.L., American Chemical Society.

Russel, W.B., Saville, D.A., Schowalter, W.R., 1989. *Colloidal Dispersions*, Cambridge University Press, Cambridge.

Vigil, G., Xu, Z., Steinberg, S., Israelachvili, J., 1994. Interactions of Silica Surfaces. J. *Colloid Interface Sci.*, 165, 367-385.

Figure A.2: Environmental SEM photomicrograph of "new" 41 μm glass beads.

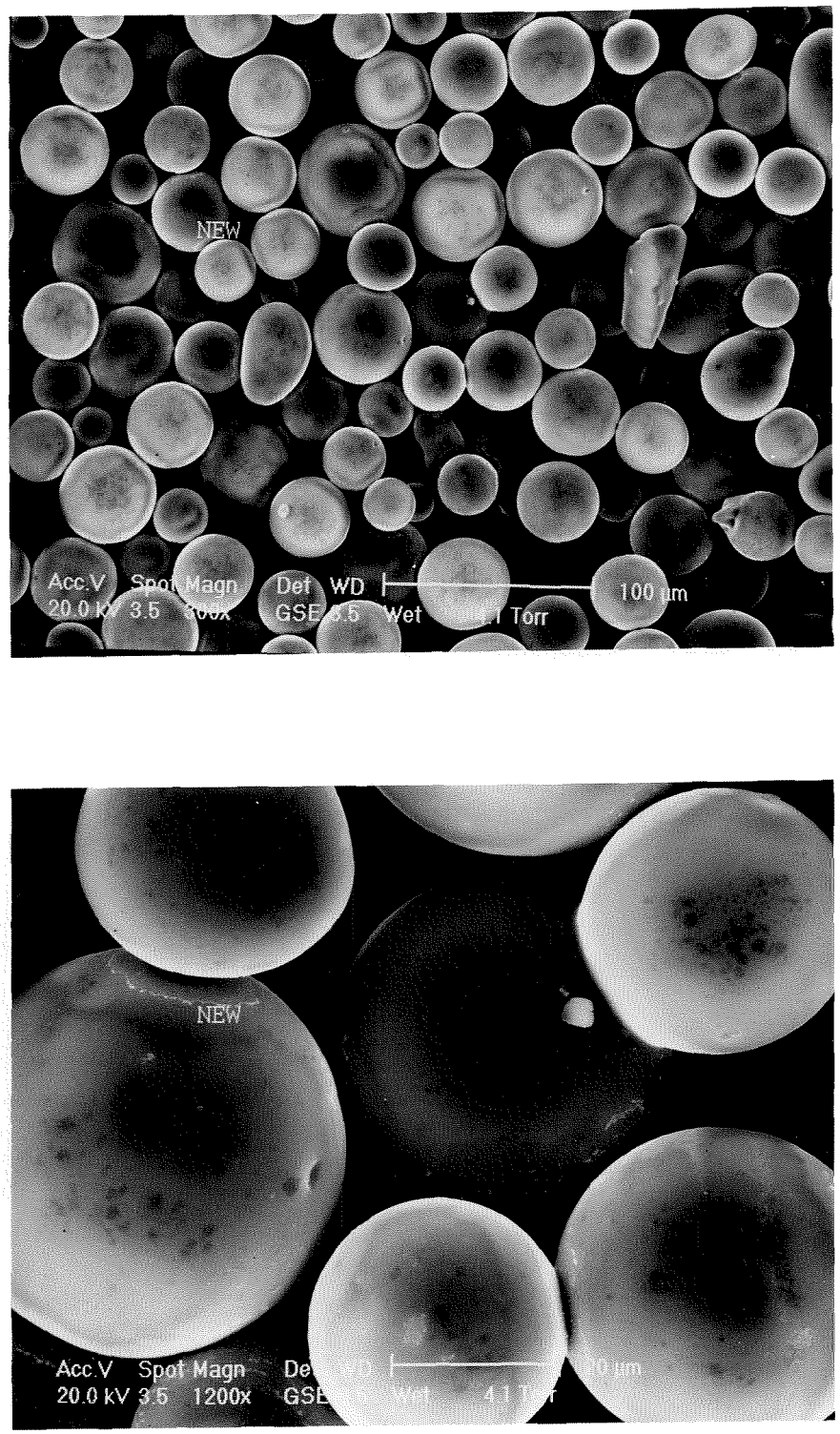

Figure A.3: Environmental SEM Photomicrograph of "old" 41 μm glass beads.